UNIVERSITÀ
DEGLI STUDI
FIRENZE

INTERNATIONAL DOCTORATE IN
Atomic and Molecular Photonics

CICLO XXVIII

COORDINATORE Prof. Righini Roberto

OPTICAL SET-UP DEVELOPMENT AND SOFTWARE INTERFACE OF 2D-VISIBLE COHERENT SPECTROSCOPY EXPERIMENT TO INVESTIGATE DYNAMICS OF MULTI-CHROMOPHORIC MOLECULAR COMPLEXES

Settore Scientifico Disciplinare CHIM/02

Dottorando
Dott. Azzaroli Nicolò

_____

Tutore
Prof. Righini Roberto

_____

Coordinatore
Prof. Righini Roberto

_____

Anni 2012/2015

Contents

Introduction

Ultrafast optical spectroscopy can elucidate sub-picosecond molecular dynamics, pinpointing information about the vibrational and electronic structures and inter- and intra-molecular interactions in the infrared and visible regions of the spectrum[1–6]. Many methods have been developed to explore and study the dynamics due to the interaction of multiple chromophores. In particular, multidimensional femtosecond spectroscopies are suitable tools to investigate electronic and vibrational couplings.

Multidimensional Fourier transform Spectroscopy[7, 8] has revolutionized the magnetic resonance world and originated a significant impact on the study of the structures of large biomolecules in solution and magnetic resonance imaging. In the past, femtosecond lasers source became a reality widely employed in spectroscopy laboratories and have been used to develop two-dimensional Fourier transform (2D FT) non linear spectroscopies[9, 10], in the electronic[11, 12] and vibrational[13–15] regions. These techniques are the optical analogs of two-dimensional Fourier transform nuclear magnetic resonance spectroscopies like NMR Correlation Spectroscopy (COSY) and NMR Nuclear Overhauser Effect Spectroscopy (NOESY). The combination of the femtosecond laser sources with 2D FT methods opened new interesting possibilities: 2D vibrational spectroscopy is employed to obtain structural information on sub-picosecond time scale, by using vibrational coupling and vibrational relaxation as molecular scale rulers; 2D electronic spectroscopy reveals dynamics in the same way the 2D NMR follows spins.

The theoretical formulation can be found in the works of Mukamel et al[5, 16, 17] and Cho[18, 19]. Pioneering experiments were performed in the groups of Hochstrasser[13, 20, 21] and Tokmakoff[14, 15] for vibrational transitions, and in the groups of Jonas[11, 12, 22–24] and Scholes[25] for

electronic transitions. In these experiments, phase-matched four-wave mixing signals are analyzed by heterodyne detection in order to obtain information about both amplitude and phase of the non linear third-order signal emitted by the sample.

In the past, 2D electronic spectroscopy has been originally limited to the wavelength range provided by the very stable output of Ti:sapphire oscillators[26]. Extending the method to a larger range of electronic transitions in the visible spectrum required the use of broadly tunable short light sources such as optical parametric amplifier (OPA). Due to different group velocities of idler and signal, the collinear generation, commonly adopted in standard OPAs, is not capable of providing the ultra.broad band pulses required in 2D electronic Spectroscopy. The development of Non-collinear Optical Parametric Amplification (NOPA) overcomes this deficiency, making ultra-broad band pulses experimentally available[27, 28].

As the 2D time resolved spectroscopy in the visible range, one has to notice that the high pulse stability and position accuracy of interferometric grade, required for this kind of experiments, is definitely more difficult to achieve in comparison tp what is needed in the infrared spectral region. The proper stabilization can be achieved passively by using diffractive optics (DO)[29–33]. Fleming and coworkers first reported the result of heterodyne detected photon echo by spectral interferometry, in short 2D Fourier spectrometry for the visible range[34, 35]. Active control of the phase stability, employing pulse shaping techniques, gives more advantages and several groups introduced this kind of devices in their experimental set-ups[36–38]. The very accurate pulse timing required in interferometric experiments is assumed by movable glass wedges[39]. They act as motion scaler, making possible to introduce very short and accurate time delays, in spite of the limitation of a mechanical translation stage.

Recently, Engel and Co improved the technique, by introducing the GRadient Assisted Photon Echo (GRAPE) spectroscopy: using conventional beam splitters, all the problems about the phase stabilization of the various pulses employed in the experiment are avoided, without the need of pulse shaping or DO, and the coherence time is scanned taking advantages of the pulse tilting front. With this approach it is possible to record a single

2D map with a single laser-shot making the experiment extremely faster and with a very high signal-to-noise ratio[40–42].

The purpose of this Ph.D. has been that of designing, realizing, testing and utilizing a set-up based on diffractive optics to be imployed in four wave mixing experiments. In particular, the interest has been focused on two-dimensional photon echo (2D PE) spectroscopy. The project included the realization of the ultra-broad band NOPA light source, yielding the ultra-short pulses ($\sim$ 20 fs) needed for the experiments. This thesis is organized as follows. In the first chapter an extended theoretical description of the four wave mixing phenomena is given. In the second chapter I describe the experimental set-up. After presenting the master laser source in the laboratory, I describe the Non-collinear Optical Parametric Amplifier (NOPA) set-up. In the third section I give a detailed description of the 2D photon echo set-up, focusing on the sub-femtosecon coherence time scan. Then the home-made NMOS based linear array detector and the acquisition program are presented. In the third chapter the codes necessary to extract the four wave mixing spectra from the row data are presented and discussed. In the fourth chapter the phase characterization of the NOPA pulses, the compression method and its efficiency are described and discussed. In the fifth and sixth chapters I report the very first 2D PE measurements performed with our set-up. The apparatus was first used to reproduce experiments already present in literature in order to verify the reliability and stability of the set-up and the efficiency of the codes for the data treatment. In the seventh chapter novel measurements on a BODIPY based bi-chromophore are reported and in the last chapter some conclusions are given and further steps are suggested.

Chapter 1

Theoretical Background

1.1 Schröedinger and Heisenberg pictures

In quantum mechanics a physical observable is associated to an operator A and the state of the system is represented by a wave function $|\psi(t)\rangle$. The expectation value of the A operator in the generic $|\psi(t)\rangle$ state is given by:

$$\langle\psi(t)|A|\psi(t)\rangle \;=\; \langle A(t)\rangle \tag{1.1}$$

In the Schröedinger picture the time evolution of the system is described by the time dependent wave function and requires solving the time dependent Schröedinger equation:

$$H|\psi(t)\rangle \;=\; i\hbar\frac{\partial}{\partial t}|\psi(t)\rangle \tag{1.2}$$

where H is the hamiltonian of the system. The solution of 1.2 is obtained introducing a set of eigenvectors $|\varphi_n\rangle$ of H with eigenvalues E_n:

$$H|\varphi_n\rangle \;=\; E_n|\varphi_n\rangle \tag{1.3}$$

The wave function is expressed as a linear combination of the eigenvectors of the $|\varphi_n\rangle$ basis set:

$$|\psi(t)\rangle \;=\; \sum_n |\varphi_n\rangle\langle\varphi_n|\psi(t)\rangle \tag{1.4}$$

Substituting 1.4 in the 1.2 we obtain the general:

$$\langle\varphi_n|\psi(t)\rangle \;=\; exp\Big(-\frac{i}{\hbar}E_n(t-t_0)\Big)\langle\varphi_n|\psi(t_0)\rangle \tag{1.5}$$

where $\langle\varphi_n|\psi(t_0)\rangle$ represent the *n-th* coefficient at time t_0. The left side of this equation suggests that the solution $|\psi(t)\rangle$ can be considered as the superposition of many terms with different phase factors:

$$|\psi(t)\rangle \;=\; \sum_n exp\Big(-\frac{i}{\hbar}E_n(t-t_0)\Big)|\varphi_n\rangle\langle\varphi_n|\psi(t_0)\rangle \tag{1.6}$$

Equation 1.6 describes the time evolution of the wave function in the time interval $[t_0, t]$. So, defining the time evolution operator:

$$U(t,t_0) = \sum_n exp\Big(-\frac{i}{\hbar}E_n(t-t_0)\Big)|\varphi_n\rangle\langle\varphi_n| \tag{1.7}$$

eq. 1.6 can be written:

$$|\psi(t)\rangle \;\equiv\; U(t,t_0)|\psi(t_0)\rangle \tag{1.8}$$

In time resolved spectroscopy, generally one deals with time-dependent hamiltonian 1.2. The time dependence of the wave function $\psi(t)$, obtained by solving the eq. 1.2, is expressed by eq. 1.8. The form of the propagator $U(t,t_0)$ is obtained from the equation of motion:

$$i\hbar\frac{\partial}{\partial t}U(t,t_0) = H(t)U(t,t_0) \tag{1.9}$$

If the Hamiltonian does not depend on time, the solution of eq. 1.9 is simply:

$$U(t,t_0) = exp\Big(-\frac{i}{\hbar}H(t,t_0)\Big) \tag{1.10}$$

In case of time-dependent Hamiltonian, the solution of eq. 1.9 is obtained iteratively. Breaking the integration path in infinitesimal intervals, the time ordering of these intervals ($\tau_{n-1} < \tau_n$) holds:

$$\begin{aligned} U(t,t_0) =& 1 + \sum_{n=1}^{\infty}\Big(-\frac{i}{\hbar}\Big)^n \int_{t_0}^{t} d\tau_n \int_{t_0}^{\tau_n} d\tau_{n-1}\ldots \\ & \int_{t_0}^{t_2} d\tau_1 H(\tau_n)H(\tau_{n-1})\ldots H(\tau_1) \end{aligned} \tag{1.11}$$

It's possible to contract this formula using the *positive time ordered exponential*:

$$U(t,t_0) = exp_+\Big[-\frac{i}{\hbar}\int_{t_0}^{t} d\tau H(\tau)\Big] \tag{1.12}$$

The expectation value of a physical observable described by the operator A is defined as

$$\langle A(t)\rangle = \langle\psi(t)|A|\psi(t)\rangle \tag{1.13}$$

substituting 1.8 in 1.13 leads to

$$\langle A(t)\rangle = \langle\psi(t_0)|U^\dagger(t,t_0)AU(t,t_0)|\psi(t_0)\rangle \tag{1.14}$$

The time dependence of the expectation value can be seen under two points of view:

- $\Big\{\langle\psi(t)\Big\}A\Big\{\psi(t)\rangle\Big\}$: The wave functions transform with $U(t,t_0)|\psi(t_0)\rangle$ and the operator is a constant;
- $\langle\psi(t_0)\Big\{U^\dagger(t,t_0)AU(t,t_0)\Big\}\psi(t_0)\rangle$: The operator varies in time according to $A(t) = U^\dagger(t,t_0)AU(t,t_0)$, and the wave function is taken at time t_0.

Schröedinger picture: In the Schröedinger picture the wave function are time dependent, their evolution is described by the Schröedinger equation. while the operators are time independent. The expectation value of an operator A is given by:

$$\langle A(t)\rangle = \langle\psi_S(t)|A_S|\psi_S(t)\rangle \tag{1.15}$$

Heisenberg picture: In the Heisenberg picture the operators are time dependent while the wave functions are time independent. With this approach the expectation value of an operator A is given by:

$$\langle A(t)\rangle = \langle\psi_H|A_H(t)|\psi_H\rangle \tag{1.16}$$

1.2 Interaction picture

This picture stays in between the Schröedinger and the Heisenberg ones; it's very useful when the time dependence of the Hamiltonian can be expressed as:

$$H(t) = H_0 + H'(t) \tag{1.17}$$

When the $H'(t)$ is small in comparison to H_0,it is possible to use the eigenstates of H_0 to describe the dynamics of the system under the action of $H'(t)$. The assumption is that the wave function for the Hamiltonian H_0, which describes the system at equilibrium conditions, is known; we treat perturbatively the time dependant part ($H'(t)$), which represents the interaction of the system with the radiation field. Now, we introduce the time evolution operator with respect to H_0: $U_0(t, t_0)$. It satisfies the equation of motion;

$$i\hbar\frac{\partial}{\partial t}U_0(t, t_0) = H_0U_0(t, t_0) \tag{1.18}$$

As H_0 is time independent, the solution of eq. 1.18 is simply:

$$U_0(t, t_0) = exp\Big[-\frac{i}{\hbar}H_0(t - t_0)\Big] \tag{1.19}$$

The wave functions in the interaction and in the Schröedinger pictures are related by:

$$|\psi_S(t)\rangle \; = \; U_0(t, t_0)|\psi_I(t)\rangle \tag{1.20}$$

where $|\psi_S(t)\rangle$ is the wave function in the Scrödinger picture and $|\psi_I(t)\rangle$ is the wavefuntion in the Interaction one.

To write the temporal evolution in the Interaction picture we need to start from the Scrödinger equation:

$$i\hbar\frac{\partial}{\partial t}|\psi_S\rangle = H(t)|\psi_S\rangle \tag{1.21}$$

using 1.20 we have:

$$i\hbar\frac{\partial}{\partial t}U_0(t, t_0)|\psi_I\rangle = H(t)U_0(t, t_0)|\psi_I\rangle \tag{1.22}$$

Substituting 1.17, we obtain:

$$i\hbar U_0\frac{\partial}{\partial t}|\psi_I(t)\rangle = H'U_0|\psi_I\rangle \tag{1.23}$$

Now multiplying by $U_0^\dagger$:

$$i\hbar U_0^\dagger U_0 \frac{\partial}{\partial t}|\psi_I(t)\rangle = U_0^\dagger H' U_0 |\psi_I\rangle \tag{1.24}$$

and defining the hamiltonian in the Interaction picture as:

$$H'_I(t) \equiv U_0^\dagger(t,t_0) H'(t) U(t,t_0) \tag{1.25}$$

the Scrödinger equation in the Interaction picture becomes:

$$i\hbar \frac{\partial}{\partial t}|\psi_I(t)\rangle = H'_I|\psi_I(t)\rangle \tag{1.26}$$

Equation 1.26 means that the time dependence of the wave function in the Interaction picture is obtained by solving the equation of motion under the effect of a reduced Hamiltonian containing only the time dependent part, expressed in the Interaction picture.

In eq 1.20 we defined the time evolution operator in the basis of H_0; in the same way we can define the time evolution operator in the Interaction picture:

$$|\psi_I(t)\rangle = U_I(t,t_0)|\psi_I(t_0)\rangle \tag{1.27}$$

Substituting in 1.26 we have:

$$i\hbar \frac{\partial}{\partial t} U_I(t,t_0) = H'_I U_I(t,t_0) \tag{1.28}$$

The solution is the same as before:

$$U_I(t,t_0) = exp_+\Big[-\frac{i}{\hbar}\int_{t_0}^{t} d\tau H'_I(\tau)\Big] \tag{1.29}$$

Substituting this latter in 1.20 we obtain:

$$\begin{aligned} |\psi_S(t)\rangle &= U_0(t,t_0)|\psi_I(t)\rangle \\ &= U_0(t,t_0)U_I(t,t_0)|\psi_I(t_0)\rangle \end{aligned} \tag{1.30}$$

Now, considering that $U_0(t_0,t_0) = \mathbf{I}$ (identity), we obtain: $|\psi_I(t_0)\rangle = |\psi_S(t_0)\rangle$, so that:

$$|\psi_S(t)\rangle = U_0(t,t_0)U_I(t,t_0)|\psi_S(t_0)\rangle \tag{1.31}$$

Expression 1.31 means that the total time evolution operator $U(t, t_0)$ can be considered as the product of two operators, one referred to H_0 and the other to $H'(t)$:

$$U(t, t_0) = U_0(t, t_0)U_I(t, t_0) \tag{1.32}$$

Using the formula derived in 1.11 we can write the complete expression for the time evolution operator in the Interaction picture:

$$\begin{aligned} U(t, t_0) &= U_0(t, t_0)U_I(t, t_0) \\ &= U_0(t, t_0) + \sum_{n=1}^{\infty} \Big(-\frac{i}{\hbar} \Big)^n \int_{t_0}^{t} d\tau_n \int_{t_0}^{\tau_n} d\tau_{n-1} \dots \\ &\int_{t_0}^{\tau_2} d\tau_1 U_0(t, \tau_n)H(\tau_n)U_0(\tau_n, \tau_{n-1})H'(\tau_{n-1}) \dots U_0(\tau_2, \tau_1)H'(\tau_1)U_0(\tau_1, t_0) \end{aligned} \tag{1.33}$$

The comparison of equations 1.11 and 1.33 makes clear the consequence of assuming the form 1.17 for the Hamiltonian and of adopting the interaction picture. In spectroscopy, the perturbation represents the interaction of the system with the radiation field that occurs at different times $(\tau_1, \tau_2, \dots, \tau_{n-1}, \tau_n)$. Before the first interaction, the system evolves freely in the interval (t_0, τ_1) according to the propagator $U_0(\tau_1, t_0)$. At the time τ_1 the first interaction occurs, described by $H'(\tau_1)$; than we have a second free evolution expressed by $U_0(\tau_2, \tau_1)$, followed by another interaction at τ_2 with the term $H'(\tau_2)$, and so on until the last interaction $H'(\tau_n)$. The last free evolution $U_0(t, \tau_n)$ ends at the time t, when the measurements is performed.

In the Interaction picture the expectation value of an operator A is given by:

$$\langle A(t) \rangle = \langle \psi_I(t)|A|\psi_I(t) \rangle \tag{1.34}$$

The evolution of the wavefuntion is described by the Schrödinger equation; using the hamiltonian in the Interaction picture we have:

$$-i\hbar \frac{\partial}{\partial t} |\psi_I(t)\rangle = H'_I(t)|\psi_I(t)\rangle \tag{1.35}$$

where $H'_I(t) = U_0^{\dagger}(t, t_0)H'(t)U_0(t, t_0)$. So the time evolution of the operator A in the Interaction picture is expressed by:

$$-i\hbar \frac{\partial}{\partial t} A_I = [H_0, A_I] \tag{1.36}$$

This picture offers a new approach to describe the evolution of the system: a part of the evolution is included in the wave function and a part in the operators. The Schrödinger and Heisenberg pictures can be derived as the Interaction picture's limiting cases: if we set $H_0 = 0$ we have $H' = H$: we recover to the Schrödinger picture, where the time evolution is included in the wave function and the operators are time independent:

$$i\hbar\frac{\partial}{\partial t}|\psi_S\rangle = H'_S|\psi_S\rangle \qquad \frac{\partial}{\partial t}A_j = 0 \tag{1.37}$$

On the other side, we obtain the Heisenberg picture if we set $H_0 = H$ and $H' = 0$:

$$\frac{\partial}{\partial t}|\psi_H\rangle = 0 \qquad \frac{\partial}{\partial t}A_H = \frac{i}{\hbar}[H_0, A_H] \tag{1.38}$$

1.3 Density operator

In quantum mechanics, the density operator ρ is the equivalent of the classical density in the phase space. It can be generalized in the form of a statistical operator, useful when the system cannot be described by a single wave function. To introduce it, we start from the expectation value of an operator A in a quantum system described by the wave function $|\psi(t)\rangle$ given in 1.13. We express the wave function as the linear combination of the vectors of an arbitrary basis set:

$$|\psi(t)\rangle = \sum_n c_n(t)|n\rangle \tag{1.39}$$

Substituting this in the 1.13 we obtain:

$$\langle A(t)\rangle = \sum_{m,n} c_m(t)c_n^\star(t)A_{mn} \tag{1.40}$$

where $A_{mn} = |m\rangle\langle n|$. Now we define the *density operator* as:

$$\rho = |\psi(t)\rangle\langle\psi(t)| \tag{1.41}$$

Using eq. 1.39, the definition 1.41 becomes:

$$\rho = \sum_{m,n} \rho_{mn}(t)|m\rangle\langle n| \tag{1.42}$$

where $\rho_{mn}(t) = c_m(t)c_n^\star(t)$ are the elements of the density operator matrix. From 1.41 it follows that $\rho(t)$ is hermitian ($\rho^\dagger = \rho$). Its is trace:

$$\begin{aligned} Tr\{\rho\} &= \sum_n \langle n|\rho|n\rangle = \sum_n \langle n|\psi\rangle\langle\psi|n\rangle \\ &= \sum_n \langle\psi|n\rangle\langle n|\psi\rangle = \langle\psi|\psi\rangle = 1 \end{aligned} \tag{1.43}$$

The expectation value of the operator A can be rewritten using the density operator formalism:

$$\begin{aligned} \langle A(t)\rangle &= \sum_n \langle\psi|n\rangle\langle n|A|\psi\rangle \\ &= \sum_n \langle n|A|\psi\rangle\langle\psi|n\rangle = \sum_n \langle n|A\rho|n\rangle = Tr\{A\rho\} \end{aligned} \tag{1.44}$$

In quantum mechanics, the state of a system is expressed by a vector while the operators by matrices. With the introduction of the *density operator*, also the state of the system is represented by a matrix. If the state of the system is described by a single wave function the system is in a *pure state* and is completely defined. In most cases this is not true, and we have to treat our system as a statistical distribution of states, each one characterized by a certain probability. If P_n is the probability for the system to be in the the $|\psi_n\rangle$ state, the density operator is defined as

$$\rho(t) = \sum_n P_n|\psi_n(t)\rangle\langle\psi_n(t)| \tag{1.45}$$

Obviously, $\sum_n P_n = 1$ and

$$1 \geq P_n \geq 0 \tag{1.46}$$

There is a difference in the traceof the density matrix of pure and mixed states. For pure states, ρ is *idempotent*, i.e. $\rho^2 \equiv \rho$. This means that:

$$Tr\{\rho^2\} = 1 \tag{1.47}$$

In mixed states we have:

$$\begin{aligned} \rho^2 &= \sum_{m,n} P_m P_n|\psi_m\rangle\langle\psi_m|\psi_n\rangle\langle\psi_n| \\ &= \sum_{m,n} \delta_{m,n} P_m P_n|\psi_m\rangle\langle\psi_n| = \sum_n P_n^2|\psi_n\rangle\langle\psi_n| \end{aligned} \tag{1.48}$$

So the trace of ρ^2 becomes:

$$\begin{aligned} Tr\{\rho^2\} &= \sum_x \sum_n P_n^2 \langle x|\psi_n\rangle\langle\psi_n|x\rangle \\ &= \sum_n P_n^2 \sum_x \langle\psi_n|x\rangle\langle x|\psi_n\rangle = \sum_n P_n^2 \langle\psi_n|\psi_n\rangle = \sum_n P_n^2 \end{aligned} \tag{1.49}$$

According to 1.46, $P_n^2 \leq P_n$ so that

$$Tr\{\rho^2\} \leq 1 \tag{1.50}$$

1.4 Time evolution of the density operator

Keeping in mind the time dependant Schrödinger equation:

$$\frac{\partial}{\partial t}|\psi(t)\rangle = -\frac{i}{\hbar}H|\psi(t)\rangle \qquad \frac{\partial}{\partial t}\langle\psi(t)| = \frac{i}{\hbar}H\langle\psi(t)| \tag{1.51}$$

The equation of motion of the density matrix yields

$$\begin{aligned} \frac{\partial}{\partial t}\rho(t) &= \frac{\partial}{\partial t}\Big(|\psi\rangle\langle\psi|\Big) \\ &= \Big(\frac{\partial}{\partial t}|\psi\rangle\Big)\langle\psi| + |\psi\rangle\frac{\partial}{\partial t}\langle\psi| \\ &= -\frac{i}{\hbar}H|\psi\rangle\langle\psi| + \frac{i}{\hbar}|\psi\rangle\langle\psi|H \end{aligned} \tag{1.52}$$

That can be written in the form of the quantum *Liouville* equation:

$$\frac{\partial}{\partial t}\rho(t) = -\frac{i}{\hbar}[H,\rho] \tag{1.53}$$

In eq. 1.53 ρ is expressed in the Schrödinger picture, and the value of the density operator at a certain time t is given by:

$$\begin{aligned} \rho(t) &= \sum_n P_n U(t)|\psi\rangle\langle\psi|U^\dagger(t) \\ &= U(t)\rho(0)U^\dagger(t) \end{aligned} \tag{1.54}$$

Using the relation between Heisenberg and Schrödinger representations of an operator A: $A_H(t) = U^\dagger(t)A_S U(t)$ and using equation 1.44, the expectation value of an operator A at the time t is:

$$\langle A(t)\rangle = Tr\{A\rho(t)\} = Tr\{AU(t)\rho(0)U^\dagger(t)\} \tag{1.55}$$

Making use of the invariance of the trace under cyclic permutation of the factors

$$\langle A(t)\rangle = Tr\{U^{\dagger}(t)AU(t)\rho(0)\} = Tr\{A(t)\rho(0)\} \tag{1.56}$$

According to the last two expressions, the expectation value of an operator A at time t can be obtained in two different ways. In 1.55 the operator is constant and he density matrix evolves in time (Schrödinger picture); in 1.56 the density operator is constant and the A operator evolves (Heisenberg picture).

In case of time independent hamiltonian H, the Schrödinger equation reduces to the eigenvalue problem $H|n\rangle = E|n\rangle$ and the time evolution operator is $U(t) = exp\Big(-\frac{i}{\hbar}Ht\Big)$. The representation of the density operator in the basis $|n\rangle$ of the eigenvectors of the time independent Hamiltonian H is

$$\langle n|\rho(t)|m\rangle = \langle n|\psi(t)\rangle\langle\psi(t)|m\rangle \tag{1.57}$$

and the wave function at time t is

$$|\psi(t)\rangle = U(t)|\psi(t_0)\rangle = \sum_l |l\rangle exp\Big(-i\frac{E_l}{\hbar}t\Big) \tag{1.58}$$

Substituting in eq. 1.57 we have

$$\begin{aligned}\langle n|\rho(t)|m\rangle &= \langle n|\rho(t_0)|m\rangle e^{-i\frac{E_m - E_n}{\hbar}t} \\ &= \langle n|\rho(t_0)|m\rangle e^{-i\omega_{mn}t}\end{aligned} \tag{1.59}$$

Equation 1.59 tells us that the diagonal elements of the density matrix are constant while the off-diagonal ones oscillates at the frequency ω_{mn}.

Considering the generic element of the density matrix, we can write:

$$\langle n|\rho|m\rangle = \langle n|\psi\rangle\langle\psi|m\rangle \tag{1.60}$$

The integral $\langle n|\psi\rangle$ is the projection of the vector $|\psi\rangle$ on the base vector $|n\rangle$ which corresponds to the value of the coefficient c_n in the expansion of $|\psi\rangle$ in that basis set: $|\psi\rangle = \sum_n c_n\varphi_n$. So the generic element $\langle n|\rho|m\rangle$ of the density matrix corresponds to the product of the coefficients of the expansion of $|\psi\rangle$ on the basis $|n\rangle$.

$$\rho_{nm} = \langle n|\rho|m\rangle = c_n c_m^{\star} \tag{1.61}$$

If $|\psi\rangle$ varies in time the coefficients are time dependent.

$$\begin{aligned}\rho(t) = |\psi(t)\rangle\langle\psi(t)| &= \sum_{n,m} c_n(t)c_m^\star(t)|n\rangle\langle m| \\ &= \sum_{n,m} \rho_{nm}(t)|n\rangle\langle m|\end{aligned} \tag{1.62}$$

From 1.61 it is clear that the diagonal elements of the density matrix ρ_{nn} represent the probability to find the system in the $|n\rangle$ state; these elements are called *population*. The off-diagonal element ρ_{nm} represent the coherent superposition of the two states $|n\rangle$ and $|m\rangle$; these terms are called *coherences*.

As expressed in the 1.59, in a time independent Hamiltonian the coherence oscillates with a frequency given by the energy difference between the two states involved.

Density operator in the Interaction picture

The density operator can be defined starting from the definition 1.20 that leads to $|\psi_I\rangle \equiv U_0^\dagger|\psi_S\rangle$. Thus we obtain:

$$\rho_I = U_0\rho_S U_o^\dagger \tag{1.63}$$

From equation 1.53 we get

$$\frac{\partial}{\partial t}\rho_I(t) = -\frac{i}{\hbar}[H_I'(t)\rho_I(t)] \tag{1.64}$$

where

$$H_I'(t) = U_0^\dagger(t,t_0)H'(t)U_0(t,t_0) \tag{1.65}$$

By integrating eq. 1.64 we find:

$$\rho_I(t) = \rho(t_0) - \frac{i}{\hbar}\int_{t_0}^{t} d\tau[H_I'(\tau),\rho_I(\tau)] \tag{1.66}$$

whose solution is obtained iteratively:

$$\begin{aligned}\rho_I(t) = \rho(t_0) &- \frac{i}{\hbar}\int_{t_0}^{t} d\tau_1[H_I'(\tau_1),\rho_I(t_0)] \\ &+ \Big(-\frac{i}{\hbar}\Big)^2\int_{t_0}^{t} d\tau_2\int_{t_0}^{\tau_2} d\tau_1\Big[H_I(\tau_2)[H_I(\tau_1,\rho(t_0))]\Big] + \dots \\ &+ \Big(-\frac{i}{\hbar}\Big)^n\int_{t_0}^{t} d\tau_n\dots\int_{t_0}^{\tau_2} d\tau_1\Big[H_I'(\tau_n),\Big[\dots[H_I'(\tau_1),\rho(t_0)]\dots\Big]\Big]\end{aligned} \tag{1.67}$$

Equation 1.67 represents the perturbative expansion of the density matrix and can be written as:

$$\rho_I(t) = \rho^{(0)} + \rho^{(1)} + \rho^{(2)} + \cdots + \rho^{(n)} \tag{1.68}$$

where $\rho^{(0)} = \rho(t_0)$.

1.5 The response function

The coherent non linear spectroscopy techniques are based on the *optical polarization* $\mathbf{P}$ which represent the expectation value of the dipole moment. This polarization is related to the electric field through the *susceptivity*:

$$\mathbf{P}(\omega) = \chi \mathbf{E}(\omega) \tag{1.69}$$

the oscillating polarization generates an oscillating electromagnetic field: the *signal*. From the quanto mechanic point of view we have:

$$\mathbf{P}(t) = \langle \boldsymbol{\mu}(t) \rangle \tag{1.70}$$

It's useful to describe the radiation-matter interaction in the perturbation limit $H = H_0 + H'(t)$. In the semi-classical approach the perturbation is

$$H'(t) = -\boldsymbol{\mu} \cdot \mathbf{E} \tag{1.71}$$

Linear absorption spectroscopy

The simplest example of coherent spectroscopy is the absorption measurement. The polarization measures the response of the sample to the incoming field and can be mathematically written as

$$\mathbf{P}(t) = \int_{t_0}^{t} d\tau R(t) \mathbf{E}(t - \tau) \tag{1.72}$$

Where $R(t)$ is the response function. From the 1.70, making use of equation 1.56 we have

$$\mathbf{P}(t) = Tr\Big\{ \boldsymbol{\mu}(t) \rho_I^{(1)}(t) \Big\} \tag{1.73}$$

Now, keeping in mind that $\rho_I^{(1)}(t) = -\frac{i}{\hbar}\int_{t_0}^{t} d\tau[H_I'(\tau), \rho_{eq}]$, from 1.71 and 1.73 we obtain:

$$\mathbf{P}(t) = Tr\Big\{\boldsymbol{\mu}_I(t)\frac{i}{\hbar}\int_{-\infty}^{t} dt'\Big[-\boldsymbol{\mu}_I(t')\cdot\mathbf{E}(t'), \rho_{eq}\Big]\Big\} \tag{1.74}$$

With the change of variable $\tau = t - t'$ and using the properties of commutators, we find:

$$\mathbf{P}(t) = \frac{i}{\hbar}\int_{0}^{\infty} d\tau \mathbf{E}(t-\tau) Tr\Big\{\Big[\boldsymbol{\mu}_I(\tau), \boldsymbol{\mu}_I(0)\Big]\rho_{eq}\Big\} \tag{1.75}$$

The comparison of 1.72 and 1.75 shows that the response function is the expectation value of the dipole moment commutator at different times:

$$R(\tau) = \frac{i}{\hbar}\Theta(\tau) Tr\Big\{\Big[\boldsymbol{\mu}_I(\tau), \boldsymbol{\mu}_I(0)\Big]\rho_{eq}\Big\} \tag{1.76}$$

$\Theta(\tau)$ enforces the causality principle, i.e. it requires that $\tau > 0$.

Non linear polarization

Equation 1.69 can be generalized by expressing the Polarization in terms of rising powers of the electric field:

$$|\mathbf{P}_i| = \chi_{ij}|\mathbf{E}_j| + \chi^{(2)}_{ijk}|\mathbf{E}_j||\mathbf{E}_k| + \chi^{(3)}_{ijkl}|\mathbf{E}_j||\mathbf{E}_k||\mathbf{E}_l| + \ldots \tag{1.77}$$

The corresponding expansion in the time domain is

$$\mathbf{P}(t) = \mathbf{P}^{(1)} + \mathbf{P}^{(2)} + \mathbf{P}^{(3)} + \ldots \tag{1.78}$$

where each term is written a form similar to 1.73:

$$\mathbf{P}(t) = Tr\Big\{\boldsymbol{\mu}_I\rho_I^{(1)}(t)\Big\} + Tr\Big\{\boldsymbol{\mu}_I\rho_I^{(2)}(t)\Big\} + Tr\Big\{\boldsymbol{\mu}_I\rho_I^{(3)}(t)\Big\} + \ldots \tag{1.79}$$

The first term $\mathbf{P}^{(1)}$ (linear polarization) describes the linear optics and the second term represents the second-order non linear processes such as sum frequency generation. The third order polarization enters in a variety of different non linear effects known as four wave mixing. Making use of the

equations previously described, the expression for the n-th order polarization is:

$$P^{(n)}(t) = \int_0^\infty d\tau_n \int_0^\infty d\tau_{n-1} \dots \int_0^\infty d\tau_1 R^{(n)}(\tau_1, \tau_2 \dots \tau_n) \\ \mathbf{E}(t-\tau_n) \cdot \mathbf{E}(t-\tau_n-\tau_{n-1}) \cdot \dots \mathbf{E}(t-\tau_n-\tau_{n-1} \cdots -\tau_1) \tag{1.80}$$

where $R^{(n)}$ is the n-th order non linear response function that carries the complete microscopic information necessary for expressing the polarization at the n-th order:

$$R^{(n)}(\tau_1, \tau_2 \dots \tau_n) = \left(\frac{i}{\hbar}\right)^n \Theta(\tau_1)\Theta(\tau_2)\dots\Theta(\tau_n) \\ Tr\left\{ \Big[\Big[\dots \big[\boldsymbol{\mu}_I(\tau_n + \tau_{n-1} + \dots + \tau_1) \boldsymbol{\mu}_I(\tau_{n-1} + \tau_{n-2} + \dots + \tau_1) \big] \cdots \Big], \boldsymbol{\mu}_I(t_0) \Big] \rho_{eq} \right\} \tag{1.81}$$

For a better comprehension of the real meaning of 1.81, we consider the response function at the second order, focusing on the commutator's part of the equation:

$$Tr\left\{ \Big[\big[\boldsymbol{\mu}_I(\tau_1+\tau_2), \boldsymbol{\mu}_I(\tau_1) \big], \boldsymbol{\mu_I}(t_0) \Big] \rho_{eq} \right\} \tag{1.82}$$

From the first commutator we get:

$$Tr\left\{ \Big[\big[\boldsymbol{\mu}_I(\tau_1+\tau_2)\boldsymbol{\mu}_I(\tau_1) - \boldsymbol{\mu}_I(\tau_1)\boldsymbol{\mu}_I(\tau_1+\tau_2) \big], \boldsymbol{\mu}_I(t_0) \Big] \rho_{eq} \right\} \tag{1.83}$$

while developing the second commutator we obtain four terms:

$$\begin{aligned} Q_1 \quad & + \boldsymbol{\mu}_I(\tau_1+\tau_2)\boldsymbol{\mu}_I(\tau_1)\boldsymbol{\mu}_I(t_0)\rho_{eq} \\ Q_2 \quad & - \boldsymbol{\mu}_I(\tau_1)\boldsymbol{\mu}_I(\tau_1+\tau_2)\boldsymbol{\mu}_I(t_0)\rho_{eq} \\ Q_3 \quad & - \boldsymbol{\mu}_I(t_0)\boldsymbol{\mu}_I(\tau_1+\tau_2)\boldsymbol{\mu}_I(\tau_1)\rho_{eq} \\ Q_4 \quad & + \boldsymbol{\mu}_I(t_0)\boldsymbol{\mu}_I(\tau_1)\boldsymbol{\mu}_I(\tau_1+\tau_2)\rho_{eq} \end{aligned} \tag{1.84}$$

Going back to the Schrödinger representation, i.e. replacing $\boldsymbol{\mu}_I(t_0) = \boldsymbol{\mu}$ and $\boldsymbol{\mu}_I(\tau) = U_0^\dagger(\tau)\boldsymbol{\mu}U_0(\tau)$, we rewrite the four terms in 1.84. For example from Q_3 we obtain:

$$-\boldsymbol{\mu}U_0^\dagger(\tau_1+\tau_2)\boldsymbol{\mu}U_0(\tau_1+\tau_2)U_0^\dagger(\tau_1)\boldsymbol{\mu}U_0(\tau_1)\rho_{eq} \tag{1.85}$$

Using the properties of the operator U ($U(t_1 + t_2) \equiv U(t_1)U(t_2)$) and the cyclic permutation, we can write:

$$-\boldsymbol{\mu}U_0(\tau_2)\boldsymbol{\mu}U_0(\tau_1)\rho_{eq}\boldsymbol{\mu}U_0^\dagger(\tau_1)U_0^\dagger(\tau_2) \tag{1.86}$$

To comprehend exactly the meaning of eq. 1.86 we have to *read* it starting from the action of the perturbation operator μ on the density matrix. We can summarize this equation as follow:

- Starting from the system at equilibrium (ρ_{eq}), the first dipole moment (to the right of ρ) acts on the bra of the density matrix;
- Going to the outside of the equation, the two time evolution operator $U_0(\tau_1)$ and $U_0^\dagger(\tau_1)$ act simultaneously on the bra and ket terms of ρ, which is not anymore in its equilibrium form. In this second step, the system evolves freely, under the unperturbed hamiltonian H_0 during the time interval τ_1.
- At the next step, the second interaction acts, via the dipole moment, on the ket of the density matrix.
- Then the modified ρ evolves freely again under H_0 for the time interval τ_2.
- Finally, the last dipole moment on the extreme left of the equation gives rise to the field emitted by the system at the time t.

The sequence of interaction described above indicates that the Q_3 is a **bra**/**ket** term.
With the same approach we can lead out the development of the other three terms which are:

- Q_1 is a **ket**/**ket** term
- Q_2 is a **ket**/**bra** term
- Q_4 is a **bra**/**bra** term

The comparison of the expressions for the Q_i terms above, shows that $Q_4 = Q_1^\star$ and $Q_3 = Q_2^\star$. This means that four terms describe just two different processes. Conventionally, only the terms in which the last interaction (the signal) acts on the ket are explicitly written. In general we can say that the n-th order response function is obtained as the sum of 2^{n-1} independent processes.

Now we can compact these equations introducing the time propagation super-operator:

$$G(t)A = U_0 A U_0^\dagger \tag{1.87}$$

Thus the Q_1 term becomes:

$$\boldsymbol{\mu} G(\tau_2)\boldsymbol{\mu} G(\tau_1)\boldsymbol{\mu}\rho_{eq} \tag{1.88}$$

Equation 1.88 shows that the $G(t)$ operator describes the free evolution of the system between two perturbation.

1.6 Feynman diagrams

An useful pictorial representation of the response function is provided by the *Feynaman diagrams*. They consist of two vertical lines representing the time evolution of ket and bra of the density matrix, the positive time direction being from bottom to top. At each interaction of the field an arrow is drown on the left if it acts on the ket or on the right if it acts on the bra. Each diagram represents one of the terms (i.e. one process) that contribute to the n-th order interaction. The rules for drawing the Feynman diagrams are:

- The density operator is represented by two vertical line, the one on the left corresponds to the time evolution of ket and the other of the bra.
- Each interaction with the field is represented by an arrow, incoming arrows represent absorptions while outgoing ones represent emissions.
- Each diagram brings a sign depending on the number n of interactions on the bra: the sign is given by $(-1)^n$.
- Between two interaction the system evolves freely under time independent hamiltonian.

- The frequency of the signal of the n-th order term is the sum of the n frequencies taken with their sign: $\omega_s = \pm\omega_1 \pm \omega_2 \pm \cdots \pm \omega_n$; the wave vector of the signal is the vector sum $\vec{k_s} = \pm\vec{k_1} \pm \vec{k_2} \pm \cdots \pm \vec{k_n}$.

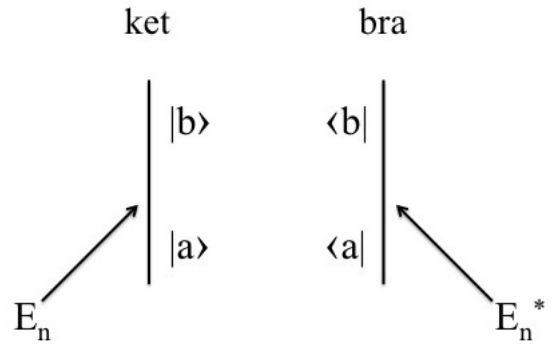

(a) Absorption

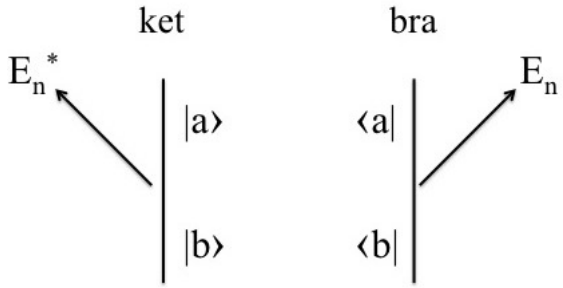

(b) Emission

Figure 1.1: Feynman diagrams representation for absorption (a) and emission(b) both from bra and ket side of density matrix

The different possible resonant interactions and their effect on the density matrix are shown in FIgure 1.1. For the ket side the incoming field gives rise to an interaction described by $(\boldsymbol{\mu}_{ab} \cdot \mathbf{E}_n) exp[i\mathbf{k}_n \cdot \mathbf{r} - i\omega_n t]$, while the emission corresponds to the complex conjugate $(\boldsymbol{\mu}_{ba} \cdot \mathbf{E}_n^{\star}) exp[-i\mathbf{k}_n \cdot \mathbf{r} + i\omega_n t]$. The opposite holds for the bra side. Figure 1.2 represent the generic Feynman diagram where the system in the population state $|a\rangle\langle a|$ interacts with the first field E_1 yielding the coherence $|b\rangle\langle a|$; then the system evolves freely for the time interval τ_1. The second field E_2 follows acting on the bra; it leads

to a different coherence state $|b\rangle\langle c|$, which evolves freely for the time interval τ_2 and so on. Finally the signal field is emitted (interaction on the ket side).

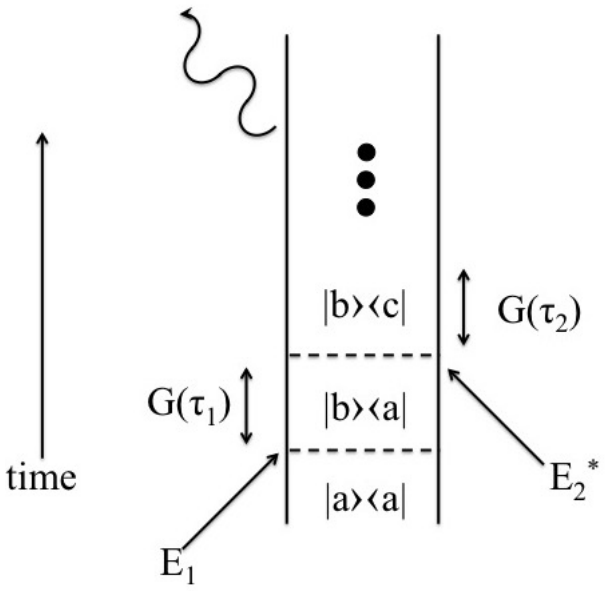

Figure 1.2

1.7 Third order non linear spectroscopy

At the third order of the polarization expansion, for a two level system in resonance with the radiation we can write eight diagrams, half of which are the complex conjugates of the others. So we have to consider four diagrams, as shown in figure 1.3. Analyzing these contributions we observe that:

- R_1 is a **ket**/**ket**/**ket** term with $\omega_s = \omega_1 - \omega_2 + \omega_3$ and $\mathbf{k}_s = \mathbf{k}_1 - \mathbf{k}_2 + \mathbf{k}_3$.
- R_2 is a **bra**/**ket**/**bra** term with $\omega_s = -\omega_1 + \omega_2 + \omega_3$ and $\mathbf{k}_s = -\mathbf{k}_1 + \mathbf{k}_2 + \mathbf{k}_3$.
- R_3 is a **bra**/**bra**/**ket** term with $\omega_s = -\omega_1 + \omega_2 + \omega_3$ and $\mathbf{k}_s = -\mathbf{k}_1 + \mathbf{k}_2 + \mathbf{k}_3$.

- R_4 is a **ket/bra/bra** term with $\omega_s = \omega_1 - \omega_2 + \omega_3$ and $\mathbf{k}_s = \mathbf{k}_1 - \mathbf{k}_2 + \mathbf{k}_3$.

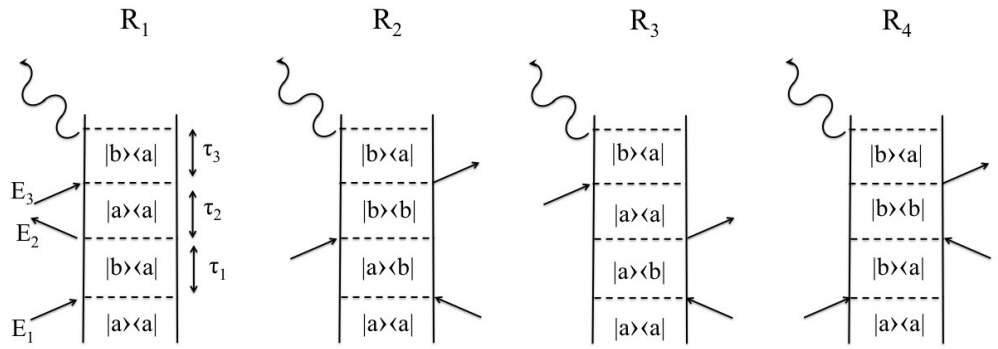

Figure 1.3: Feynman diagrams describing third order polarization for a two level system in resonance.

Using the notation given in eq. 1.88, the expression for R_2 is

$$R_2 = (-1)^2 p_a(\mu_{ba}^{\star})(e^{-i\omega_{ab}\tau_1})(\mu_{ba})(e^{-i\omega_{bb}\tau_2})(\mu_{ab}^{\star})(e^{-i\omega_{ba}\tau_3})(\mu_{ab}) \tag{1.89}$$

where p_a is the probability of finding the system in the population state $|a\rangle\langle a|$. The dipole moments represent the interaction of the system with the electric field at different times t_1, t_2 and t_3, while the phase factors represent the phase acquired by the system during the free evolution intervals τ_1, τ_2 and τ_3. Considering that $\omega_{bb} = 0$, we have:

$$R_2 = p_a|\mu_{ab}|^4 exp\Big[- i\omega_{ba}(\tau_3 - \tau_1)\Big] \tag{1.90}$$

Multipling eq. 1.90 by the fields, we obtain the third order polarization. For diagram R_2 the product of the three fields is:

$$\mathbf{E}_1\mathbf{E}_2\mathbf{E}_3 = E_1^{\star}(e^{i\omega_1 t - i\mathbf{k}_1\cdot\mathbf{r}})E_2(e^{-i\omega_2 t + i\mathbf{k}_2\cdot\mathbf{r}})E_3(e^{-i\omega_3 t + i\mathbf{k}_3\cdot\mathbf{r}}) \tag{1.91}$$

Using the relations $\omega_s = -\omega_1 + \omega_2 + \omega_3$ and $\mathbf{k}_s = -\mathbf{k}_1 + \mathbf{k}_2 + \mathbf{k}_3$ we have:

$$\mathbf{E}_1^{\star}\mathbf{E}_2\mathbf{E}_3 = E_1^{\star}E_2E_3e^{-i\omega_s t + i\mathbf{k}_s\cdot\mathbf{r}} \tag{1.92}$$

Similarly, we have for R_4:

$$R_4 = p_a|\mu_{ab}|^4 exp\Big[- i\omega_{ba}(\tau_3 + \tau_1)\Big] \tag{1.93}$$

The comparison of equations 1.90 and 1.93 shows that in the time interval τ_1 the density matrix oscillates differently: in 1.90, (R_2 diagram) we have $G(\tau_1) = exp(i\omega_{ba}\tau_1)$ while for R_4 $G(\tau_1) = exp(-i\omega_{ba}\tau_1)$. These operators add phase to the density matrix; being the signs in the two exponent opposite, the total phase acquired goes to zero when $\tau_3 = \tau_1$. For the diagram R_4 the phase factor acts with the same sign in the both intervals, so there is no cancellation. Note that during τ_2 the frequency ω_{bb} is zero, so no phase is acquired in that interval. We can graphically summarize the phase behaviour as in Figure 1.4.

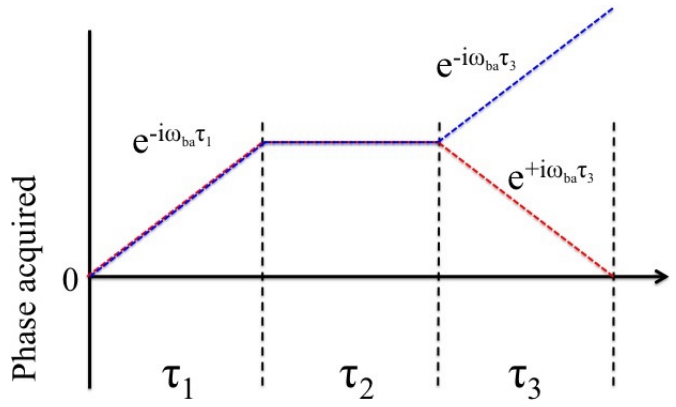

Figure 1.4: History of phase acquired from the density matrix in the R_2 (red) and R_4 (blue) diagrams.

This figure pinpoints the different nature of the two diagrams. The total phase in R_2 goes back to zero at $\tau_3 = \tau_1$; this term is called *rephasing*. In contrast, in R_4 diagram the phase continues to grow: this term is called *non-rephasing*. Using the same approach for the other two diagrams we find that R_1 and R_4 are both *non-rephasing* while R_2 and R_3 are both *rephasing* terms.

1.8 Wave vectors to select Feynman diagrams

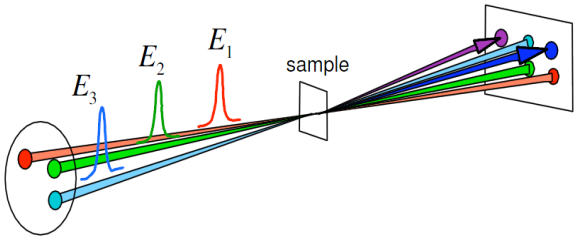

Figure 1.5: Box car geometry.

It's easy to realize that, in case of box car geometry(Figure 1.5) of the fields, the Rephasing and Non-rephasing signals are emitted in different directions. We already noticed that in the rephasing diagrams the signal is emitted in the direction $\mathbf{k}_{sig} = -\mathbf{k}_1 + \mathbf{k}_2 + \mathbf{k}_3$, while in the non-rephasing diagrams the signal propagates with $\mathbf{k}_{sig} = \mathbf{k}_1 - \mathbf{k}_2 + \mathbf{k}_3$. Assuming that $\omega_1 = \omega_2 = \omega_3 = \omega_{sig}$, so that the modulus of the wave vectors of all the beams is the same $|\mathbf{k}| = \frac{2\pi}{\lambda} n$. Figure 1.6 (c) reports the corresponding front view of the Rephasing (R) and Non-rephasing (NR) signals. In this case the Non-rephasing signal is emitted

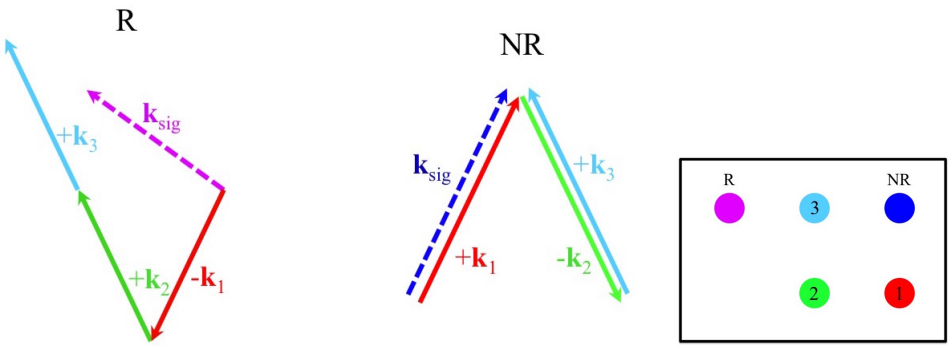

(a) (b) (c)

Figure 1.6

in the fourth vertex of the square while the rephasing one is emitted on the left of the square. From Figure 1.6 (a) it is clear that in this case the phase

matching condition is not satisfied: this means that the rephasing signal is vanishingly weak.

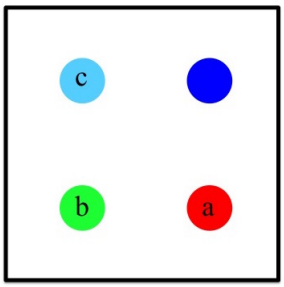

Figure 1.7

However, is possible to observe at the phase matching position both rephasing and non rephasing signals just varying the time ordering of the incoming fields. The 1,2 and 3 indexes in the Figure 1.6 (c) represent the time ordering. If we label with the indexes a, b and c the three applied fields, Figure 1.7 shows the location of the three fields and of the signal on the target.

It is easy to realize that the signal at the position $\mathbf{k}_{sig} = \mathbf{k}_a - \mathbf{k}_b + \mathbf{k}_c$ corresponds to:

- chosen timing a=1, b=2 and c=3: Non-rephasing signal (diagrams R_1 and R_4)
- chosen timing a=2, b=1 and c=3: rephasing signal (diagrams R_2 and R_3)

1.9 Three Pulse Photon Echo

Three pulse photon echo is a particular example of four wave mixing technique in which three pulses interact with the sample and produce a signal in a particular phase-matched geometry. In the presence of inhomogeneus broadening the photon echo spectroscopy gives access to the natural linewidth of the optical transitions. When this experiment is performed with ultra short pulses, whose spectrum is broad enough to cover a significant part of the absorption/emission spectrum of the sample, the three pulse photon echo effect

can be used to generate a two-dimensional frequnecy-frequency map: this experiment is known as Two-Dimensional Photon Echo (2D PE) spectroscopy. In the 2D map one recognize diagonal peaks, corresponding to the main spectral features of the linear spectrum, and off-diagonal peaks due to inter-state coupling. In the presence of inhomogeneity of the system, these features are not detectable in linear spectra while are well visible in 2D PES with high time and frequency resolution. By measuring the 2D PES as a function of the delay time between the first two pulses and the third pulse (the *probe*) we can resolve the dynamics of various inter- and intra-molecular processes. For example, energy transfer manifests itself as growth of off-diagonal peaks in the 2D spectrum. The bath fluctuations modulate the site energies and the coupling strength of and between chromophores in the system, what has a marked effect on the lines shapes of diagonal and off-diagonal peaks.

The Pulse sequence in a 2D PES experiment (see Fig. 1.8) consists of three

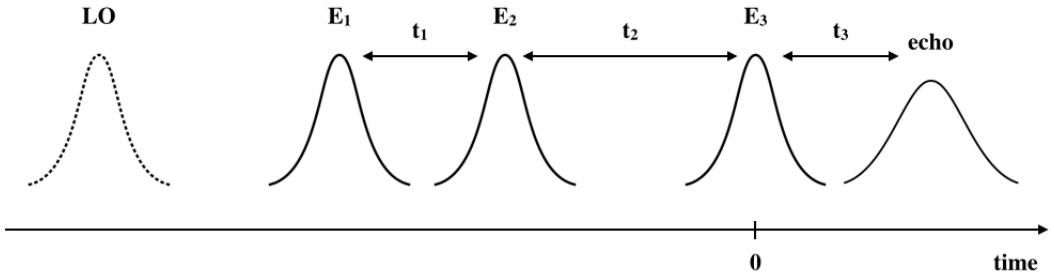

Figure 1.8: Three pulse photon echo sequence. The time zero is set when the probe field (E_3) hits the sample.

pulses and of an additional pulse (the local oscillator). All pulses have the same central frequency, resonant with the energy separation of two stationary levels of the sample. The first pulse creates a single-quantum coherence, which evolves for the coherence time t_1. The second pulse gives rise to a population state; after it, the system evolves freely, undergoing relaxation during the population time t_2. The third pulse generates a second coherence that evolves during t_3, and finally the signal is emitted. The local oscillator is spatially superimposed to the signal, so that the detector, consisting of a monochromator and of an array sensor, measures the interference spectrum

of the two, thus realizing a heterodyne detection of the signal.

Note that the relevant time for measuring the dynamics of the sample is the population time t_2, which corresponds in Figure 1.8 to the time separation between E_2 and E_3. The univocal definition of its value requires that the scanning of t_1 is done as two independent scans. Of course, the condition $t_1 = 0$ corresponds to the perfect overlap in time of E_1 and E_2. Starting from $t_1 = 0$, E_1 is scanned to negative times; then is brought back to zero delay and E_2 is moved to negative times. With this procedure the time position of the pulse that comes later among E_1 and E_2 is kept fixed, so that the value of t_2 is unambiguous.

Chapter 2

Experimental Set-Up

2.1 Introduction

Spectroscopy is the study of the light-matter interaction. The choice of one particular light source rather than others depends on which kind of phenomena we wish to investigate. In ultrafast spectroscopies light pulses as short as few femtoseconds (10^{-15} s) are used. This extremely short duration corresponds to very high peak powers and power densities, and gives the possibility of accessing very fast chemical processes and with extremely high time-resolution of monitoring ultrafast dynamics. One of the most commonly used techniques to measure ultrafast dynamics is *pump-probe*. The first pulse, the pump, excites the sample and the second one, the probe, measures changes in the absorption spectrum induced by the pump pulse at different delay times. In our case we need a system that produces ultra-broad tunable laser pulses in order to cover all the visible range with an extremely high temporal resolution ($\sim$ 15fs).
Nowadays, ultrafast light sources are commercially available and widely employed. Ti:Sapphire lasers generate pulses with time duration less than 20 fs with an output band centered approximately at 800 nm with a bandwidth $>$50 nm. It is possible to achieve 100 nm bandwidth pulses with tuneable central wavelength in the visible range using parametric generation in a *non-collinear optical parametric amplifier* (NOPA), equipped with a compression stage in order to compensate for the frequency dispersion introduced in the

amplification stage.

This chapter describes the light sources and the experimental setup used to perform 2D Photon Echo measurements. In the first section the laser system is briefly presented. In the second one I describe the principle of the Optical Parametric Amplification (OPA), focusing on the Non-Collinear case, which we used to generate ultra-broadband visible laser pulses. Finally, the 2D Photon Echo setup is presented and described. Special attention is devoted to the method used to scan the coherence time. In fact, recording the echo signal requires particularly precise and accurate scanning of the time t_1 with sub-femtosecond step. Such a short step is very hard to achieve with traditional methods and it is practically impossible to guarantee the precision and accuracy needed. In the last section I describe the home made array detector and the software used for data recording and treatment.

2.2 Light Sources

2.2.1 Ti:sapphire oscillator and amplifier

The laser system used in the ultrafast laboratory at *LENS* is the commercial Coherent® Micra amplified by the Coherent® Legend Elite regenerative cavity.

Main Oscillator

In our system the ultrashort pulses are generated by the self-mode locking Ti:Sapphire Micra laser. Laser output occurs in a broad range of wavelengths corresponding to different resonant frequencies (modes) of the cavity. If no phase-relation between these modes is established, the various frequencies interfere with each other and the output fluctuates in time. Mode-locking fixes the relative phases of the modes and forces the laser to emits a train of temporally narrow light pulses. The larger the range of frequencies at which the laser oscillates, the shorter the time duration of the mode-locked pulse obtained. The Micra produces pulses centered at 810 nm with 85 nm bandwidth and power of 400 mW at 89 MHz repetition rate. The pulses can be compressed to a duration $<$20 fs.

Stretcher, amplifier and compressor

The output of the Micra has to be amplified in order to achieve the desired pulse energy. This step is done by using the pulses from the oscillator as seed for the regenerative amplifier. The Legend Elite regenerative amplifier employs three stages: the stretching, the amplification and the compressor. This procedure is called *chirped pulse amplification*. To reduce the peak power in the amplifier, the pulse is stretched by a factor 1000-5000, so that it can be amplified safely; it is then compressed back to a duration as close as possible to its initial value. After compression we obtain a total energy per pulse >3 mJ with a pulse duration of 35 fs at 1KHz repetition rate.

2.3 Ultra-broadband visible pulse generation: non-collinear optical parametric amplifier

When intense laser light interacts with non-linear materials, non linear optical phenomena appear. Some of these effects have great practical importance, allowing the generation of new frequencies, thus extending the spectral range of the laser in a very broad range, from the Ultraviolet to the Infrared regions. The basic process is a second order non-linear optical process ($\chi^{(2)}$). In practice when two waves at frequencies ω_1 and ω_2 propagate in a non-linear crystal, a third wave at frequency ω_3 is generated by the second order process. This process is called sum frequency generation (SFG) as $\omega_3 = \omega_1 + \omega_2$. If $\omega_1 = \omega_2$ we have the second harmonic generation (SHG). Difference frequencies generation (DFG) takes place when $\omega_3 = \omega_1 - \omega_2$. Another very important non-linear interaction is Optical Parametric Generation (OPG). Here a pump wave at frequency ω_3 generates, in a non linear crystal, two new waves at ω_1 and ω_2 called *idler* and *signal* such that $\omega_1 + \omega_2 = \omega_3$. If a week wave (seed) at frequency ω_1 or ω_2 is present together wit the pump, an amplification of the signal or idler will occur: this process is called Optical Parametric Amplification (OPA). In an OPA device operating in collinear geometry, the propagation direction in the nonlinear crystal is selected to satisfy, for a given signal wavelength, the phase-matching condition $\Delta k = 0$. In this condition the signal and idler group velocities are fixed; equally fixed

is the phase matching bandwidth that can be accepted. An additional degree of freedom can be introduced using a non-collinear geometry: pump and signal wave vectors form an angle α (independent of signal wavelength) and the idler is emitted at an angle Ω with respect to the signal (Figure 2.1). In this

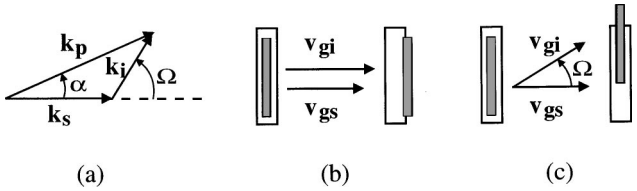

Figure 2.1: (a) Non-collinear interaction geometry schema. (b) Representation of signal and idler pulse in collinear condition. (c) The same of (b) in non-collinear interaction[28].

case the phase matching condition involves vectors which, projected onto the directions parallel and perpendicular to the signal wave vector become:

$$\Delta k_{par} = k_p cos(\alpha) - k_s - k_i cos(\Omega) = 0 \tag{2.1}$$

$$\Delta k_{perp} = k_p sin(\alpha) - k_i sin(\Omega) = 0 \tag{2.2}$$

Note that the angle Ω is not fixed, as it depends on the signal wavelength. If the signal frequency increases by $\Delta\omega$, the idler frequency decreases by $\Delta\omega$ and the wave vector mismatches along the two directions can be approximated as:

$$\Delta k_{par} \simeq -\frac{\partial k_s}{\partial \omega_s}\Delta\omega + \frac{\partial k_i}{\partial \omega_i} cos(\Omega)\Delta\omega - k_i sin(\Omega)\frac{\partial \Omega}{\partial \omega_i}\Delta\omega \tag{2.3}$$

$$\Delta k_{perp} \simeq \frac{\partial k_i}{\partial \omega_i} sin(\Omega)\Delta\omega + k_i cos(\Omega)\frac{\partial \Omega}{\partial \omega_i}\Delta\omega \tag{2.4}$$

To achieve broadband phase matching, both Δk_{par} and Δk_{perp} must vanish. Multiplying equation 2.1 by $cos(\Omega)$ and equation 2.2 by $sin(\Omega)$, adding the results and setting equal to zero, we get:

$$\frac{\partial k_i}{\partial \omega_i} - cos(\Omega)\frac{\partial k_s}{\partial \omega_s} = 0 \tag{2.5}$$

which is equivalent to:

$$\nu_{gs} = \nu_{gi} cos(\Omega) \tag{2.6}$$

Equation 2.6 shows that broadband phase matching can be obtained for an angle Ω (signal-idler angle) such that the signal group velocity equals the idler group velocity projected along the signal direction. In the collinear case (Fig 2.1(b)), signal and idler travel with different group velocities and get quickly separated, causing pulse lengthening and bandwidth reduction. On the contrary, with collinear geometry (Fig. 2.1(c)) the two pulses manage to stay effectively overlapped. In our case, we pump the non linear crystal (a type I β-BariumBorate BBO) with $\lambda_p = 400$ nm for a signal wavelength $\lambda_s = 600$ nm. Broadband phase matching is achieved for $\alpha = 3.7°$ inside the crystal which allows us to obtain an emission band extending from 500 to 750 nm[28].

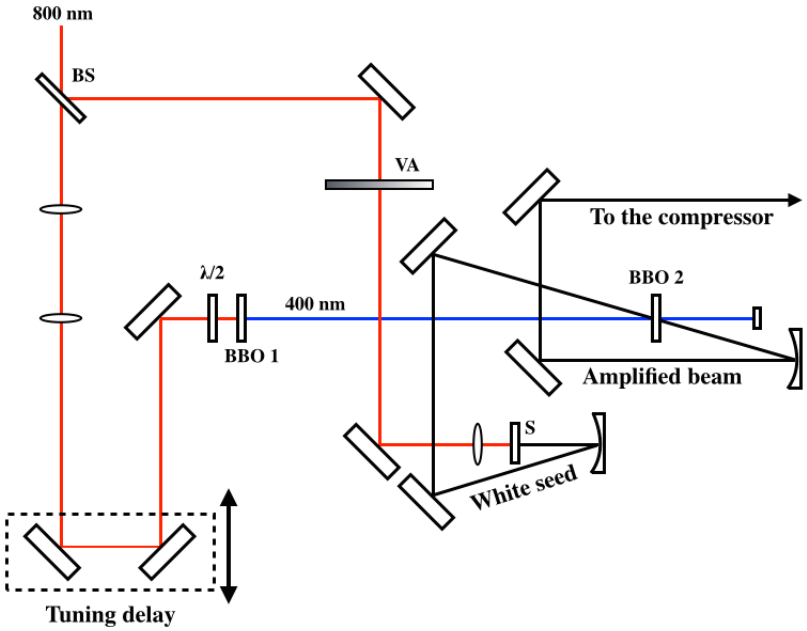

Figure 2.2: NOPA schema; BS = beam splitter, BBO 1 = 2mm Type I BBO $\theta = 29°$ for 400 nm pump pulses generation, VA = variable attenuator, S = 2mm sapphire plate for white light generation, BBO 2 = 1mm Type I BBO $\theta = 32°$.

A fraction of approximately 400 μJ per pulse is splitted off the Ti:Sapphire regenerative amplifier output and are employed to pump the BBO crystal of

our Non-collinear Optical Parametric Amplifier (NOPA). The pump pulses (400 nm wavelength) are obtained by frequency doubling of the fundamental through a 2mm type I BBO $\theta = 29°$ crystal; the power of the incoming 800m beam is variable via $\lambda/2$. The seed pulses are generated focusing another small fraction of the input light into a 2 mm thick sapphire plate. Carefully controlling the energy incident of the plate with a variable optical-density attenuator and the position of the plate close to the focus, a highly stable white-light continuum is generated. To avoid the introduction of additional chirp, only reflective optics are employed to guide the white light to the amplification stage. Parametric gain is obtained using a 1 mm thick BBO crystal cut at $\theta = 32°$, using a single pass configuration to increase the gain bandwidth. The chosen crystal length is close to the pulse-splitting length for signal and pump at the wavelength of interest. The white light seed is driven on the amplification crystal with a spherical mirror, with a spot size nearly matching the one of the collimated pump beam. The amplified pulses have an energy of approximately $2\mu J$, after the amplification the pulses are collimated by a spherical mirror and sent to the compressor stage (Fig. 2.2).

2.4 2D Photon Echo Setup

After the ultra-broadband generation, the amplified pulses are sent to the compression stage in order to compensate for the optical dispersion acquired during the amplification process. This step is performed by a couple of Dispersion Compensating Mirrors (DCMs): with nine bounces per mirror we obtain pulses compressed enough for our purpose. More details about this step are given further on.

The setup for the experiment is a conventional four wave mixing scheme in the box car geometry. The compressed pulses are split in two arms by a 50:50 beam splitter (BS). The reflected part generates the two pump beams and is sent two a motorized stages for population time scan (t_2) (DL). The transmitted part produces the probe beam that stimulate the emission of the echo signal, and the local oscillator (LO) used for heterodyne detection. The two arms are placed on the same vertical plane but at different height and focused by a spherical mirror (SM1) onto a phase mask (PM) where they

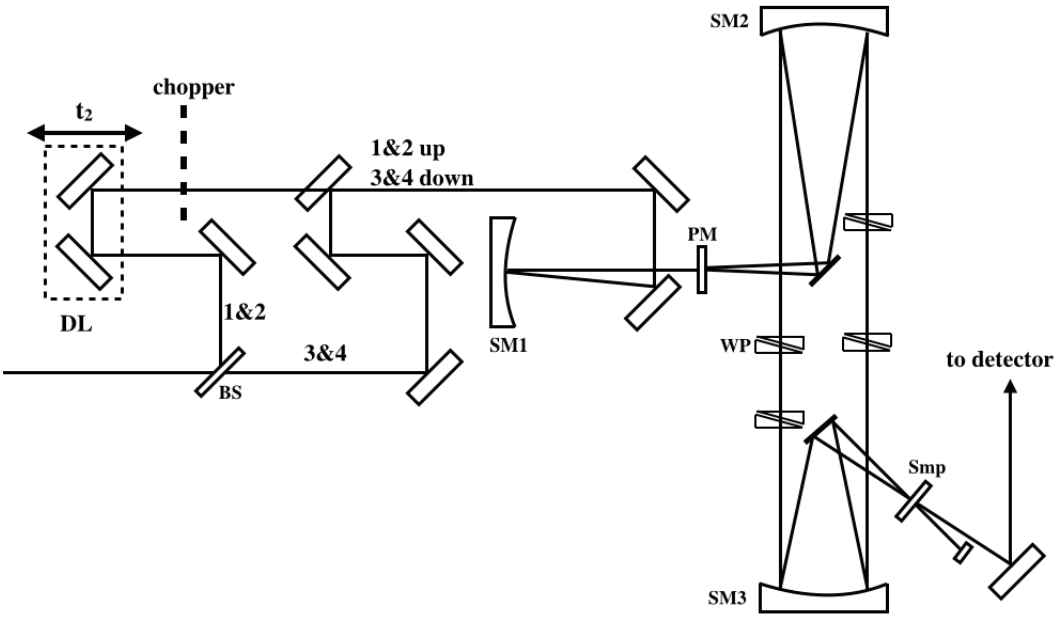

Figure 2.3: 2D Photon Echo setup.

generate the four replicas needed for the experiment in box car geometry. In this schema, the echo field is emitted towards the fourth vertex of the square as shown in Figure 1.7, and the local oscillator is naturally overlapped on it. All the beams are collimated by the same spherical mirror (SM2) and focused on the sample (Smp) by a second mirror (SM3). Along the collimated path between SM2 and SM3 finely tunable delay is added on each beam. In particular, for the two pump replicas two pairs of wedges (WP) in antiparallel configuration (Fig. 2.4) mounted on motorized stages are employed, one for each arm. This allows us to perform coherence time (t_1) scan independently for the rephasing and non-rephasing diagrams with sub-femtosecond steps. More details about how they work are given later on. Other two couples of wedge mounted in antiparallel configuration on non-movable mounts are employed to separate in time the probe beam and the local oscillator. The delay between them has to be constant and well known during the data acquisition and is crucial for the phase reconstruction of the echo signal. This point will be treated in a next section. An additional beam, which follows an independent path, is splitted off to generate the reference beam

which is sent to the detection system in order to minimize the noise on the spectrum due to laser fluctuations. Finally, a chopper is placed on the pump beam, so that the transient absorption signal ΔA is measured as:

$$\Delta A = log\left(\frac{I^{on}_{probe}}{I^{on}_{ref}}\frac{I^{off}_{ref}}{I^{off}_{probe}}\right) \cdot 1000 \tag{2.7}$$

where I^{on}_{probe}, I^{on}_{ref}, I^{off}_{probe} and I^{off}_{ref} are, respectively, the probe and reference signal's intensities with and without the pump pulse.

2.4.1 Sub-femtosecond Time Scan

One of the major difficulties from the experimental point of view in recording 2D spectra is that the coherence time needs to be varied with very high accuracy to avoid possible artifacts in the Fourier transform of the time domain data from which the 2D spectrum is obtained. This step is crucial for visible spectra (much less in the infrared region), because at those wavelengths accidental variation of the path length can easily lead to large phase error. Clearly, the required accuracy is increasingly difficult to achieve at shorter wavelengths. Here we use the approach adopted by Brixner and Co[43].

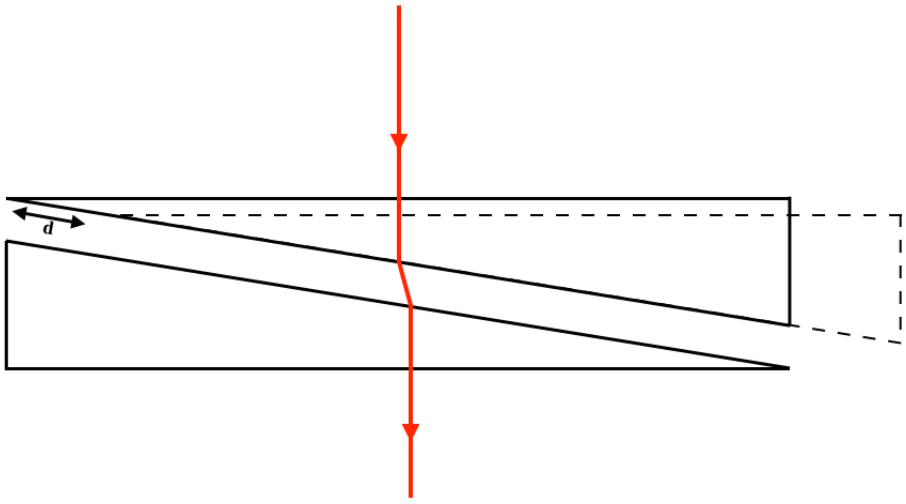

Figure 2.4: Wedge configuration for sub-femtosecond time step scan, d is the moving wedge's travel direction.

The fine control of the time delay between pulses 1 and 2 cannot be achieved easily using conventional delay stages because of two reasons. First, is not so trivial to place them in a box car geometry setup; second, and most relevant, it would be very hard to obtain the required delay precision with this method. To record 2D echo measurements we need to perform t_1 delay time step of the order of ~ 100 as. With a conventional delay stages this corresponds to 0.015 μm spatial motion of the motorized stage. The motorized stages we adopt are the M 112.1DG from PI® which guarantees a minimal incremental resolution of 0.1 μm definitely higher than the step we need, so a different approach is required. The adopted method consists in realizing this delay with interferometric precision using fused silica movable glass wedges with thickness from 2mm to 1.4mm and angle 1°, placed on the computer-controlled motorized stages described above. Each wedge is closely paired with another identical one mounted in antiparallel orientation (Fig. 2.4) on a fixed support. Lateral translation occurs along the inner surfaces, keeping the outer ones perpendicular to the laser beams. In this way the beams have a very small lateral displacement that, considering the collimated geometry in which this wedges act (Fig. 2.3), do not alter the geometry of the experiment. Figure 2.4 provides a sketch of the way the wedges work. Each pair of wedges acts on the beam as one glass plate of varying thickness, adding delay on that particular beam. The glass wedges act as a *motion scaler*, so that moderately precise mechanical movements are transferred into very high precise time delays. In particular a movement of 0.1 μm of the stages corresponds to a delay time of approximately 4 as at 600 nm. The dispersion introduced by the wedges is negligible but, if needed, can be compensated *a posteriori* in the data treatment procedure as will be shown later.

In the calibration procedure the sample is replaced by a pinhole. This leads to diffraction of beams 1 and 2, when they are crossed in the pinhole. There the two beams interfere: the light scattering from the pinhole edges drives a fraction of the interference pattern to the detector, where it is measured as a function of the time delay between the two pulses, expressed in spatial position (mm) of the motorized stages.

A pulse centered at 600 nm has a period of 10.5 fs. In order to take 5

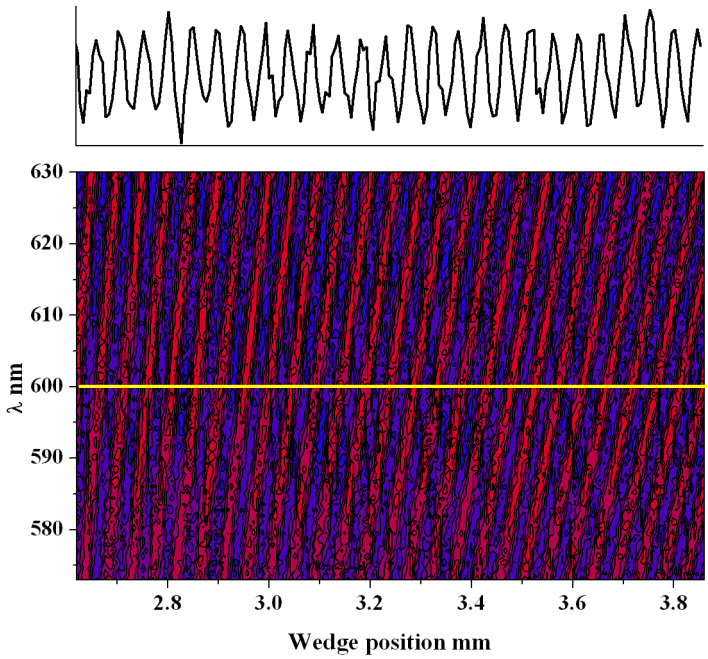

Figure 2.5: Spectral interference patterns between pulses 1 and 2 recorded with 6 μm steps by moving the glass edge on arm 1. The cross section among the horizontal yellow line delivers the temporal oscillations for that particular wavelength shown on top.

points per period we need 200 as time step which corresponds in 6 μm spatial movement of the motorized stage. The result is shown in Figure 2.5. The temporal separation between adjacent interference maxima (moving along the wedge-position axis) depends on the wavelength (vertical axis). The 2D plot shows the fringe pattern: the tilt of the stripes increases with the time pulses separation. At the precise pulses overlap all the wavelengths have the same phase and the corresponding stripe is exactly vertical. In this way is possible to determine the time-delay zero point with interferometric precision. The slice from Figure 2.5 at one particular wavelength (600 nm, yellow line) gives temporal oscillations which are present within and outside of the pulse temporal overlap. Knowing the wavelength and counting the temporal oscillations, it is easy to convert the wedge displacement into time delay. Although the calibration factor is, in principle, wavelength dependent,

we used the same value for all the spectra. It is worth to notice that, because of small mechanical differences between the moving wedges placed on the two arms, different calibration factors were used for the two arms.

2.4.2 Probe and Local Oscillator Fields

The Probe pulse is the E_3 field in the four wave mixing experiment (Fig. 1.8); it is the one that creates the last coherence, so that after a time $t_3 = t_1$ the echo signal is emitted.

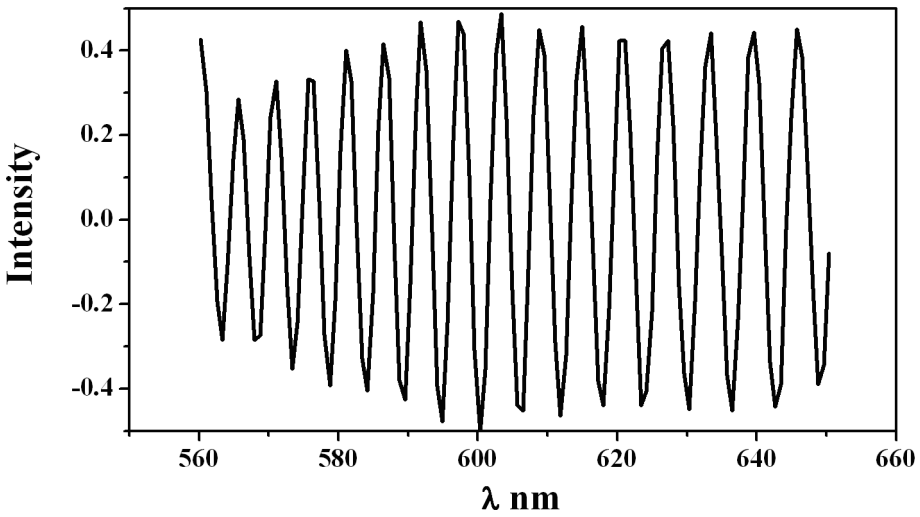

Figure 2.6: Interferogram between the probe and the local oscillator fields.

The local oscillator (LO) is an auxiliary field necessary for the heterodyne detection. An other wedge pair is employed to balance the dispersion of the probe field with respect to beams 1 and 2. A third couple of wedges is placed on the LO beam, to allow manual fine-tuning of the delay time between the probe and the local oscillator. To avoid influencing the response of the system, the pair on the LO beam is slightly tilted, so that the consequent beam displacement moves the local oscillator out of the pulse overlap in the sample cell. It is crucial for the reconstruction of the 2D map of the echo signal to determine the phase difference between E_3 and LO. This was accomplished in a preliminary interferometric measurement, before the echo

data recording. A pinhole is placed in the sample couvette, the E_3 field is chopped and the LO is sent to the detector. An interferogram is recorded (Fig. 2.6) and the phase is reconstructed from a Fourier analysis. In all our experiments the delay of the local field LO with respect to the probe E_3 field was close to 200 fs.

2.5 Echo Signal Detection

The E_1, E_2 and E_3 fields are blocked after the sample, while the LO and the echo signal are focused at the entrance of a Horiba Jobin Yvon® CP 140 1602 monochromator operating in the wavelength range from 285 to 715 nm with 16.8 nm/mm average dispersion. For the acquisition of the spectrum we used a home-made NMOS liner array detector. The detection are performed by two NMOS arrays of 256 pixels, one for the LO+echo and the other for the Reference beam. The combination of monochromator and array gives a spectral resolution of 0.8 mm/pixel. The entire acquisition apparatus is controlled by a Field Programmable Gate Array (FPGA) mounted on a custom printed circuit board designed by the LENS' Electronic Workshop. The FPGA's firmware, written by Prof. Marco Prevedelli in C++ language, set all the electronic timings during all the acquisition process, from the download of the data from the array to their transfer, via USB, to the PC. All these steps are synchronized with the laser trigger.

2.6 Acquisition Program

The acquisition program was developed in LabVIEW® (Laboratory Visual Instrumentation Engineering Workbench) programming language, a platform and development environment for visual programming language from National Instrument Corporation. The programming language used, called *G*, is a data-flow language; the execution is determined by the structure of a graphical block diagram, *LV-source code*, on which the programmer connects different function-nodes by drowing wires. These wires propagate variables and any node can execute as soon as all its input data become available. *G*

is capable of parallel execution, thus multi processing and multi threading hardware is automatically exploited by the built-in schedule. One benefit of LabVIEW is the extensive support for accessing instrumental hardware. All the hardware employed for this setup is controlled by digital codes in LabVIEW. The acquisition program allows the operator to perform different operations needd for the experiments, from the single spectrum acquisition to the complete scan of all the three temporal axes used for the echo experiment. In the following few words are spent to describe all the subroutines implemented in the software.

Stand-by

This is the default mode. At the first run and when a measure is stopped the program automatically goes in this mode. Here is possible to create two different time scan files. The first is dedicated to the t_2 population time scan, the second one to the t_1 coherence time scan. The latter is identical for both E_1 and E_2 time scans. In this mode is also possible to set the home position of the three motorized stages and set different time zero which are different for 1D or 2D experiments. It is also available possible to set the parameters for the calibration of the array detector and save the Probe file. This procedure is performed placing interferential filters on the light beam path, in this way is possible to assign to a particular array's pixel one single wavelength value. Once at least three points are recorded with a linear fitting procedure is possible to retrieve the whole probe's wavelength window.

Background

The first thing to do before starting a measurement is to record the dark background with incident light blocked. In this way the program record two data set (one for each array) which will be subtracted during the data acquisition or during the live-monitoring of the signals to eliminate any offset due to electronic or background noise from the room illumination. This operation is crucial to obtain clean measurements.

Show Spectrum

This is the basic routine, to which other routines dedicated to the data acquisition are strongly inspired. In this mode is possible to live monitor the LO and Reference beams which illuminate the arrays. A switch is implemented to change what is shown in the data graph. When enabled, the subroutine executes the operation described in equation 2.7 and shows the transient differential signal. It is also possible to save a data file with the intensities of LO and Reference beams. This mode allows the operator to move independently all three stages in order to vary both the coherence and the population time delay involved in the echo experiment. This routine is very important for the optimization of the setup alignment and to determine the zero-point position for each motorized stages.

1D Scan

This mode allows to record a set of spectra recorded at different t_2 population delays. This routine is very useful in performing preliminary measurements before the 2D spectrum acquisition. It is possible to measure 1D Transient Absorption Spectrum just blocking the E_3 beam and setting $t_1 = 0$ (E_1 and E_2 are coincident). In this way the LO acts as a probe of the excited sample, and measure a one-dimensional spectrum in function of t_2. This procedure is very useful to monitor the effective compression and dispersion of the pulses. A flat wave-front is crucial for the 2D Photon Echo spectra reconstruction. This is also used to perform Transient Grating (TG) measurements. It is sufficient let all the four beams hit the sample with the t_1 delay set to zero. The TG measurement is obtained by scanning the two coincident pump pulses.

Scan Axis 1

This routine is identical to the 1D Scan one, but for the motorized stages involved. In this mode it is possible to move the wedge pair mounted on the E_1 beam path, allowing the operator to perform a fine scan with a virtual resolution $\sim$ 4 as (attosecond = 10^{-18} s). This routine was employed to estimate the dispersion of the amplified pulses generated from the NOPA

and to characterize the pulse duration after the compression stages. More details are given later.

Scan Axis 1/2

This mode allows the operator to record the data for a two-dimensional spectrum. In particular, it performs two scans: one of the wedge pair mounted on E_1 and another one for that mounted on E_2. Two sets of data are recorded for Non-rephasing and Rephasing diagrams respectively. Both stages use the same *time scan file* described above. Before starting the scans, the t_1 delay is automatically set at zero moving both the stages at their home position. Then the scan of axis 1 starts. The field E_1 is progressively anticipated with respect to the E_2 so that the t_1 delay increases without varying the population time t_2 (see Fig. 1.8). At the end of the scan, the stage return to its home position and the E_2 axis scan starts. The two files are saved with the same file name but the letters *NR* and *R* are added respectively to the Non-rephasing and Rephasing file's names. With this routine is possible to reconstruct a 2D Electronic Spectrum for a given population time. This kind of measurement is useful to make the last check before to start the 2D scan.

2D Scan

This mode is very similar to the previous one; in addition it includes the scan of the population time. In particular, the routine reads the first position value of t_2 written in the scan file and sets the relative motor stages at the proper position. Then a 2D measurement is performed with the same procedure described for the Scan Axis 1/2 routine. The operatin is repeated for the next population time t_2, and so on. This routine allows hands-off measurements, it is very important for this kind of experiments, as a complete measurement can take up to 48 hours. In this way, the operator is free to follow the measurement in remote via FTP or SSH protocol. The data recorded are saved as describe for the previous routine, adding the value of t_2 to the Non-Rephasing and Rephasing file's names.

Chapter 3

Data Treatment

3.1 Introduction

The spectral resolution of our monochromator and the sensitivity of the detector allow us to separate in time the LO and the E_3 fields $\sim$ 200 fs; in literature longer time separation are generally adopted. In those cases the common adopted scheme has the local oscillator (LO) field arriving onto the sample as the first field. Of course the time separation between LO and E_3 sets the upper limit to the t_2 population time that can be achieved; in this case the maximum t_2 is of the order of 1 ps. Figure 3.1 (a) illustrates this pulse sequence for the three pulses photon echo measurement: LO pulse arrives before all the other and the population time scan never create a overlap between LO and pump pulses. If the LO-E_3 time separation is made shorter, say 200 fs, the LO field arrives after E_1 and E_2 (see Figure 3.1 (b)). In this case the LO acts on the sample as the third field. Theoretically, the wave vector selection rule guarantees no contamination in the echo signal's direction, but in this condition the LO, acting as third field, generates another echo signal (at the population time $= t_2 - t_{LO}$) emitted in the E_3's direction. The consequence of it is just a loss o intensity on the echo emitted in the LO's direction (when the signal is detected). When $t_2 \sim t_{LO}$ the LO and the pump fields overlap and unwanted interference effects can be generated that alter the echo signal. For those reasons we decided to adopt the pulse sequence shown in Figure 3.2. In this way we avoid the overlap between

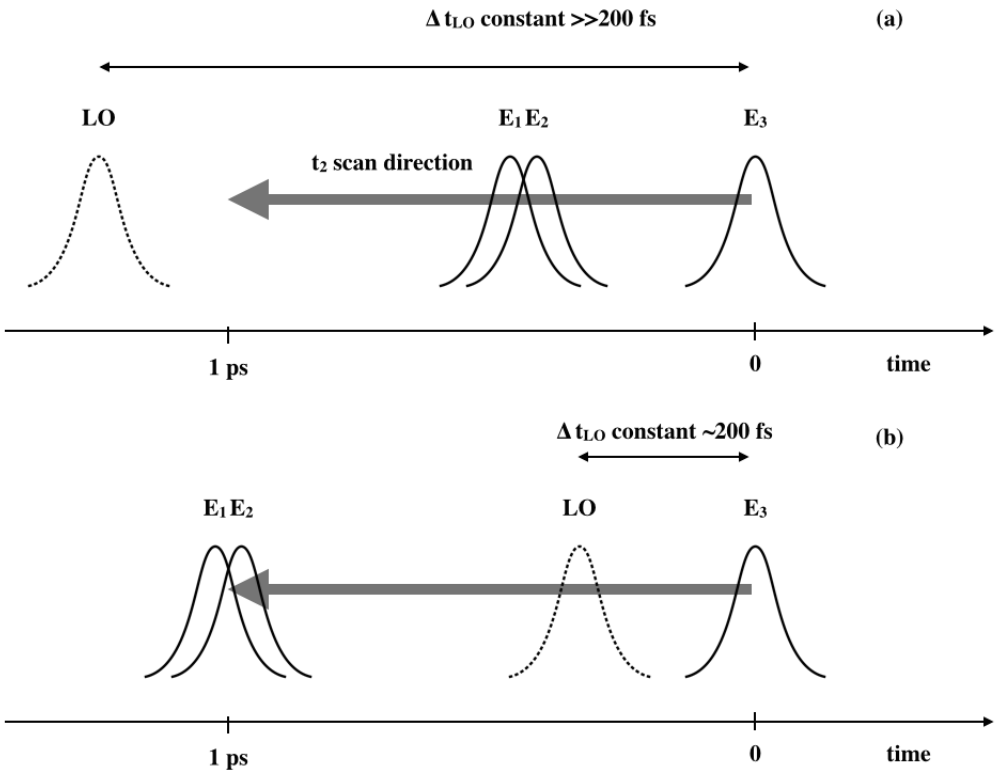

Figure 3.1: Possible tie sequences of the pulses in echo experiments. Absolute time grows from left to right; in btoh cases the local oscillator field (LO) precedes by a constant time Δt_{LO} the probe field E_3. (a) The LO precedes all three pulses E_1, E_2 and E_3. (b) The LO field precedes E_3 by a short lag ($\sim$ 200 fs) so that it is in between E_3 and the two excitation pulses E_1 and E_2.

the LO and the pump fields, and no loss of echo signal's intensity occurs. On the other hand, we have a constant contamination from the pump-probe spectrum. In fact, arriving as last the field, LO basically *probes* the sample excited by the previous chopped pulses, so that the pump-probe signal is always superimposed to the four-wave mixing signal (Transient Grating and 2D Photon Echo). An accurate Fourier filtering procedure to get rid of the pump-probe contribution is needed before the data are treated for the extraction of the spectra.

In the following I describe the procedures and the computer codes used for the four-wave mixing measurements recorded with our setup. The first

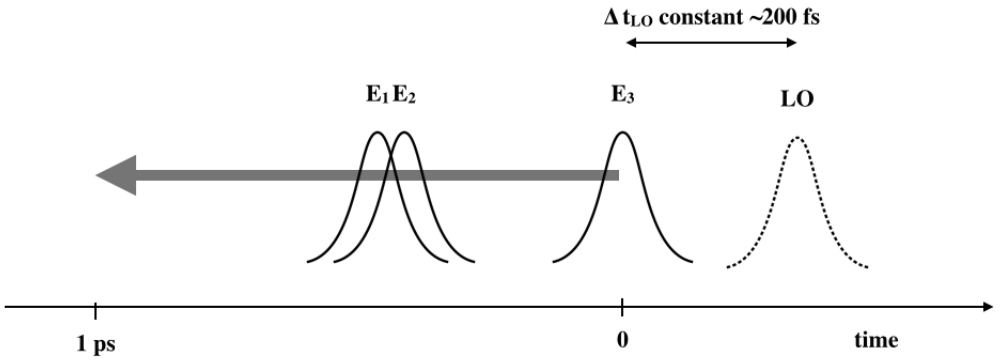

Figure 3.2: Oure choice for the oulse sequence: the local oscillator LO comes after the E_1, E_2 and E_3 pulses. With this sequence the E_1 and E_2 pump pulses never overlap the LO.

section concerns the Transient Grating data analysis. This operation is simpler respect to that for the Photon echo and does not require preliminary measurements. In the second section I explain exhaustively the method for obtaining the 2D Photon Echo map. This procedure requires a very accurate knowledge of the phase difference between the E_3 field an the LO, and an accurate minimization subroutine is crucial for the fine tuning of the phase correction when the Rephasing and Non-rephasing spectra are summed.
The data treatment procedure described in the following sections was translated in a computer code written in Matlab language (from MathWorks® Co). This language is particularly indicated to manipulate this kind of spectroscopic data, thanks to the subroutine functions implemented as data smoothing, direct and inverse fast-fourier transform (fft and ifft) and the minimization routines.

3.2 Transient Grating Spectra

In the transient grating experiment, the fields E_1 and E_2 overlap in the sample at the same time (taken as zero time) and set-up the optical grating; the delayed third field E_3 probes the grating. The heterodyne detection of the diffracted probe beam is made possible by adding a local oscillator (LO),

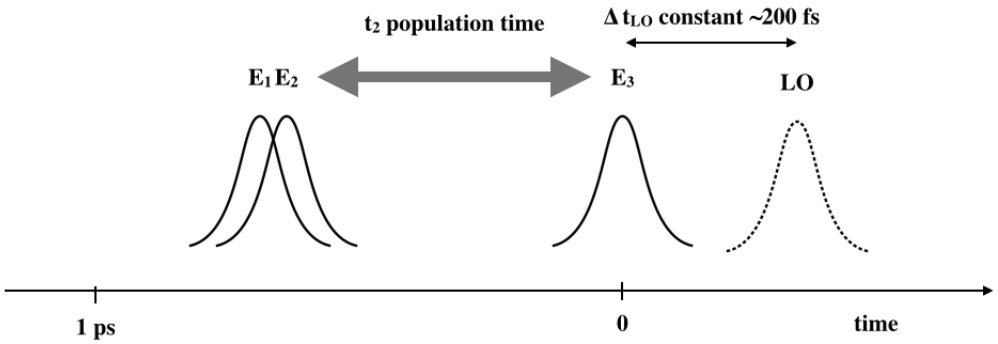

Figure 3.3: Transient Grating experiment pulse sequence.

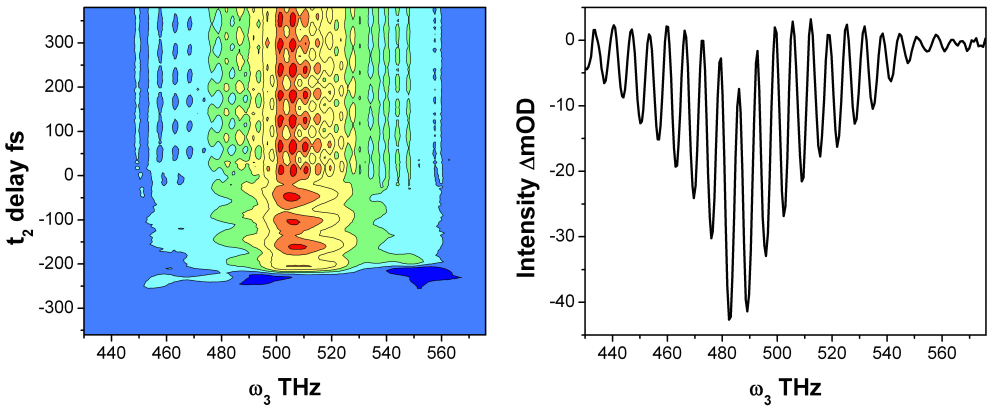

(a) (b)

Figure 3.4: (a) Row data containing both transient grating and pump-probe contributions. In the delay time interval from -200 fs to zero only the pump-probe is present. (b) Horizontal slice taken from Figure 3.4 (a) at $t_2 = 300$ fs, where both TG and pump-probe are present. The oscillations are due to the interference of the TG signal with the local oscillator.

which is made spatially coincident with the diffracted signal. In our case, the LO field reaches the sample 220 fs after the E_3 probe field; the time sequences is sketched in Figures 3.3 with fields E_1 and E_2 coincident in time. It is evident that, when scanning the population time, the pump-probe signal appears at negative delay time $t_2 = -220$ fs. At $t_2 = 0$, when E_1 and E_2 coincide with E_3, the transient grating signal appears, superimposed to

the pump-probe signal. This composite signal persists for the entire range of positive delays considered. This picture is confirmed by the results shown in Figure 3.4 (a), where the TG row data are plotted against the population delay time. Cleaning the row data from the unwanted pump-probe contri-

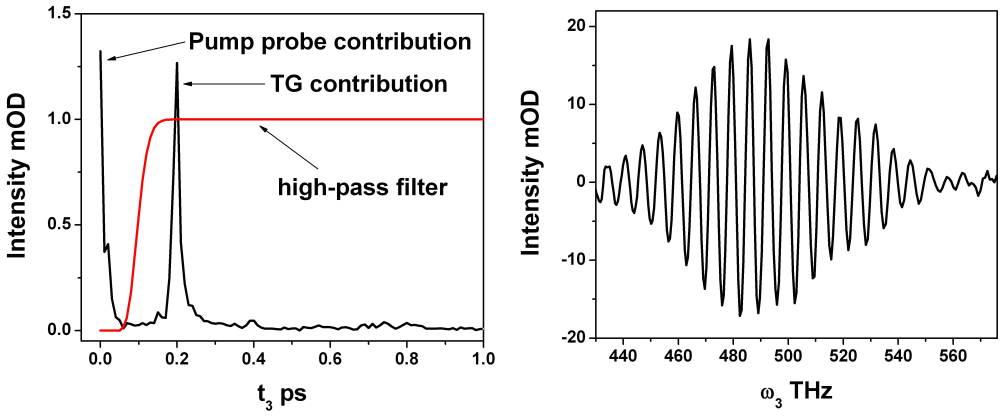

(a) (b)

Figure 3.5: (a) Inverse Fourier transform of the spectra sown in Fig 3.4 (b) (black line). at $t_3 = 0$ the pump-probe contribution shows up. The peak at ~ 200 fs is the transient grating signal. The red line is the band-pass filter with gaussian shape applied to the row data. (b) The oscillating signal is the Fourier transform to the ω_3 space after filtering.

bution requires a Fourier filtering procedure. Consider the Figure 3.4 (b). Performing an Inverse Fourier Transform along the ω_3 axis we obtain the intensity profile (absolute value) plotted vs the conjugated time t_3, shown in Figure 3.5 (a). The non-oscillating part (the pump-probe contribution) appears as a band at $t_3 = 0$, while the oscillating part appears as a band centered at $t_3 \sim 200$ fs. This value represent the period of the oscillations in Figure 3.4 (b), which corresponds to the time separation between the transient grating signal and the local oscillator. By using a high pass filter it is possible to cut off the zero time contribution, so that the Fourier transformation back to the ω_3 domain gives the oscillating signal due to the TG signal free of the pump-probe contribution, as shown in Figure 3.5 (b). At this point we have to remove the oscillation due to the interference between the transient grating signal and the LO field; this is accomplished by multi-

plying the real part of each spectrum by the associated phase factor obtained from the the Fourier transformation previously described. In Figure 3.6 the reconstructed time evolution of the transient grating spectrum for the Cresyl Violet is presented.

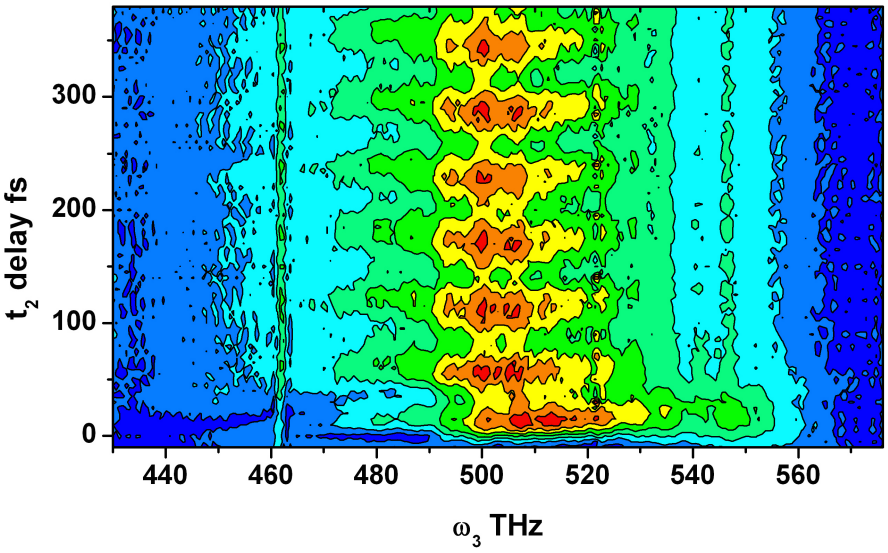

Figure 3.6: Reconstructed time evolution of the Transient Grating spectrum for Cresyl Violet.

3.3 2D Photon Echo

Extracting the photon echo data and reconstructing the 2D spectrum is definitely more complex than obtaining the transient grating signal. In fact, to obtain a complete two dimensional spectrum one has to scan also the time separation t_1 between E_1 and E_2. Actually, since the population time t_2 is defined as the time separation between E_2 and E_3, in order to have an univocally defined value of t_2 we have to perform two independent scans, one for E_1 preceding E_2 and another for the opposite time ordering. The two different conditions correspond to the Non-rephasing and Rephasing contributions, respectively. Also needed is the interferogram between the E_3 and the LO fields, and it has to be recorded separately. In the Rephasing,

Non-rephasing and E_3-E_{LO} interferogram data, the same pump-probe contribution mentioned for the TG experiment is present and has to be filtered out. For what concerns the interferogram between E_3 and E_{LO} the same filtering procedure described above is employed. The procedure used to clean the Rephasing and Non-rephasing data from the pump-probe contribution is somehow more sophisticated; it is described in details in the followiong.

The row data recorded consist of a series of interferograms between the emitted signal E_S and the LO field (E_{LO}) collected at each t_1 step for a fixed t_2 time. The quadratic detector reveals an intensity which depends on the fields E_S and E_{LO}. The expression of the measured intensity is:

$$\begin{aligned} I(\omega_3;t_1,t_2) =& \left|E_{LO}(\omega_3)e^{i\omega_3\Delta t_{LO}} + E_S(\omega_3;t_1,t_2)\right|^2 = \\ & \left|E_{LO}(\omega_3)\right|^2 + \left|E_S(\omega_3;t_1,t_2)\right|^2 + \\ & E_{LO}(\omega_3)e^{i\omega_3\Delta t_{LO}}E_S^\star(\omega_3;t_1,t_2) + E_{LO}^\star(\omega_3)e^{-i\omega_3\Delta t_{LO}}E_S(\omega_3;t_1,t_2) \end{aligned} \tag{3.1}$$

where Δt_{LO} is the time delay between E_3 and LO. Considering that the homo-dyne signal $\left|E_S(\omega_3;t_1,t_2)\right|^2$ is negligibly small since $E_{LO} \gg E_S$ and that $\left|E_{LO}(\omega_3)\right|^2$ is a time-independent constant offset which is chopped off, the remaining term is just the last one relative to the interferogram between the LO and the echo signal. The oscillation of this contribution is due to the time separation between the emitted signal E_S and the LO, however the echo signal is defined considering the time delay between the emitted E_S field and the probe E_3 field. To reconstruct this phase factor is sufficient to subtract the phase difference between the LO and the E_3 fields, recorded with a previous measure. Indicating with $S_S(\omega_3;t_1,t_2)$ the expression for the echo signal, the mathematical operations needed to isolate it from the intensity, recorded by the detector, are given in Equation 3.2:

$$S_S(\omega_3;t_1,t_2) \propto E_{LO}^\star E_S(\omega_3;t_1,t_2) = F\Big[\Theta(t_3)F^{-1}I(\omega_3;t_1,t_2)\Big]e^{i\omega_3\Delta t_{LO}} \tag{3.2}$$

where F and F^{-1} are, respectively, the Fourier and the inverse Fourier transforms (in this case along ω_3 and its conjugate t_3) while $\Theta(t_3)$ is an Heaviside function which equals to zero all contributions for $t_3 < 0$, thus filtering out the pump-probe contribution[44]. Briefly, the inverse Fourier transform projects the $I(\omega_3;t_1,t_2)$ in the t_3 domain where the Heaviside function filters out the

pump probe contribution and guarantees the causality principle, then the direct Fourier transform transforms back the cleaned signal in the ω_3 domain. At this point the phase contribution due to the time separation between E_{LO} and E_3 is removed.

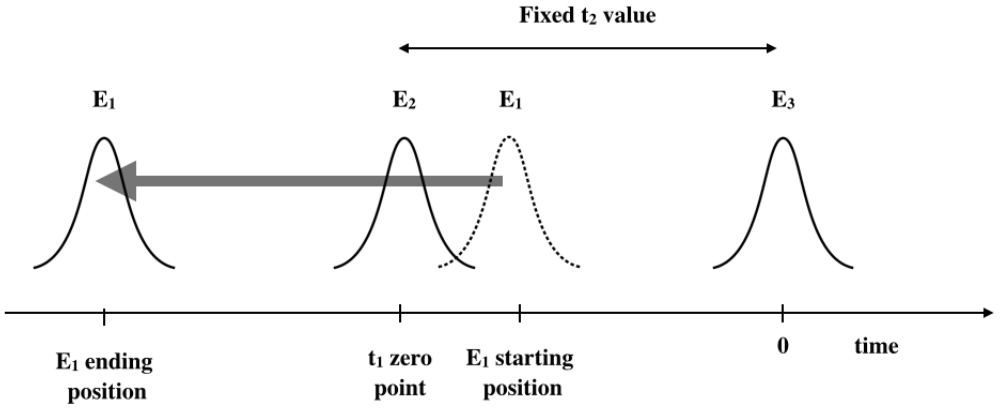

Figure 3.7: Sketch of the scan procedure for the t_1 delay time (separation between E_1 and E_2) for the Non-rephasing contribution. The E_1 starting position (dotted line) is at negative t_1 delay (with respect to E_2), its final position is after E_2. The same procedure is adopted for obtaining the Rephasing contribution, interchanging the role of E_1 and E_2. In this way we are sure that the zero delay time is contained in both interferograms so that it can be easily located.

Once the data are free of the pump-probe contribution and the causality principle is guaranteed by the Heaviside function, we have to reconstruct the full t_1 scan. To be sure of the perfect overlap of the two interferograms at $t_1 = 0$, the t_1 time is scanned from *negative* delays to positive ones with respect to E_2 as shown in Figure 3.7. In this way we are sure to locate the exact zero delay time in both components. At this point is sufficient to cut the two data sets at the proper $t_1 = 0$ and add the two interferograms. The complete interferogram is shown in Figure 3.8. From the pump-probe-free data, the 2D spectrum is obtained as the two-dimensional Fourier transform along t_1 and t_3. In our experimental se-up, the trasnfor along t_3 is performed by the monochromator. The absorptive 2DES spectrum is obtained adding the real parts of the separatelly collected Rephasing and Non-rephasing components

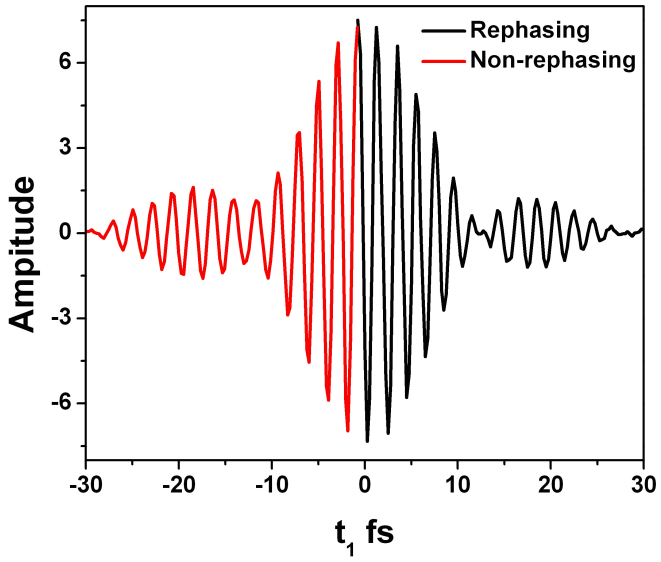

Figure 3.8: Rephasing (black line) and Non-rephasing (red line) interferograms cut at $t_1 = 0$ and plotted vs the global t_1 axis.

(Eq. 3.3).

$$\begin{aligned} &S(\omega_1, t_2, \omega_3) = \\ &Re\Big[\int_0^\infty dt_1 \int_0^\infty dt_3 S_R(t_1, t_2, t_3) e^{-i\omega_1 t_1} e^{i\omega_3 t_3} + \\ &+ \int_0^\infty dt_1 \int_0^\infty dt_3 S_{NR}(t_1, t_2, t_3) e^{i\omega_1 t_1} e^{i\omega_3 t_3}\Big] \end{aligned} \tag{3.3}$$

In priciple, at this point it should be sufficient to operate the Fourier transform along t_1 for both components, take the real part and add them:

$$S(\omega_1, t_2, \omega_3) = Re\Big[S_R(\omega_1, t_2, \omega_3) + S_{NR}(\omega_1, t_2, \omega_3)\Big] \tag{3.4}$$

Actually, other little correction are needed to obtain the exact 2D map. In fact, there may be uncontrollable experimental discrepancies that result in relevant inconsistencies in the final spectra. The number of mathematical operations that have to be done on the row data is quite large: everything has to work at its best in order to have reliable final results. First we have to consider carefully the spectral scans of t_1 leading to the Rephasing and Non-rephasing spectra. The delay is scanned by discrete intervals and is possible that the zero point saved in the memory of the motorized stages doesn't

coincide exactly with the real one. The perfect determination of the t_1 zero point is crucial for a perfect calibration of the two-dimensional spectrum, so a parameter which takes into account this indetermination has to be included in the program code. As already noticed, the Rephasing and Non-rephasing spectra are recorded with different motorized stages; we have the necessity of including two different parameters, one for each interferogram. Another sensible point is the phase difference between E_3 and E_{LO}. There is some indeterminacy on its value, and we need a parameter which accounts for this sense. Another important aspect to be considered is the chirp of the pulses used in the experiment. Its presence affects remarkably the final 2D spectra, so that it has to be made as small as possible. Our compression stage, as will be shown in the next chapter, guarantees a flat wave-front, but an *a posteriori* correction can be helpful, as reported by Park et al[45]. The correction for the chirp can be included in the correction for the phase that we make in the ω_1, ω_3 frequency domain, after the final transform and before the two parts are added:

$$S(\omega_1, t_2, \omega_3) = \\ Re\Big[S_R(\omega_1, t_2, \omega_3) exp\big[i\phi_R(\omega_1, \omega_3)\big] + S_{NR}(\omega_1, t_2, \omega_3) exp\big[i\phi_{NR}(\omega_1, \omega_3)\big]\Big] \tag{3.5}$$

where:

$$\phi_R = \omega_1 \Delta t_{1,2} + \omega_3 \Delta t_{3,LO} + \omega_1\omega_3 Q_1 + \omega_1^2\omega_3^2 Q_2 \tag{3.6}$$

$$\phi_{NR} = -\omega_1 \Delta t_{1,2} + \omega_3 \Delta t_{3,LO} + \omega_1\omega_3 Q_1 + \omega_1^2\omega_3^2 Q_2 \tag{3.7}$$

In details, the term $\Delta t_{1,2}$ is the parameter relative to the uncertainty on the zero time when scanning t_1: it acts on the ω_1 axis; the $\Delta t_{1,2}$parameter has opposite sign in the Rephasing and Non-rephasing terms. As t_1 is varied i two independent scan, corresponding to the Rephasng and Non-rephasing contributions, the value of $\Delta t_{1,2}$ may be different in the two terms.
The $\Delta t_{3,LO}$ parameter takes into account the indetermination of the time separation between E_3 and E_{LO}; it acts on the ω_3 axis and is equal for both contributions. The number of terms needed for the chirp correction depends on the order of the correction to be included, which depends on the

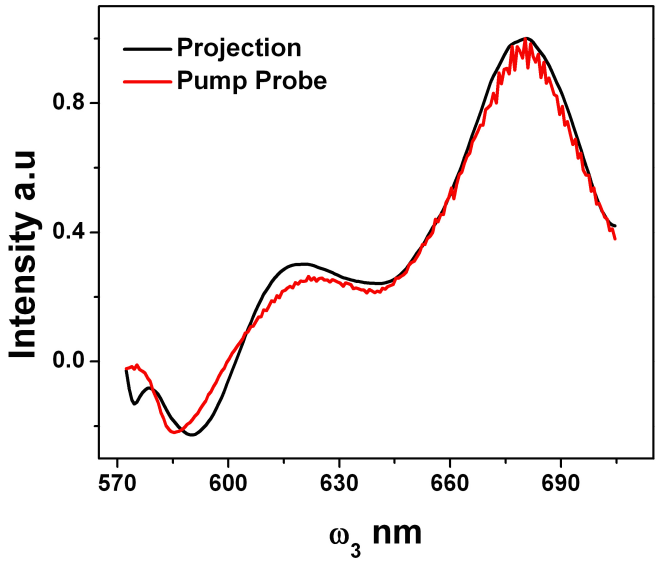

Figure 3.9: Comparison between the pump-probe spectrum (red line) of Rhodamine 800 dissolved in MeOH and the projection of the reconstructed 2D map (black line) of the same sample. The comparison with the data of ref.[46] shows a substantial improvement.

actual dispersion of the optical set-up. In our case we included linear and quadratic corrections. The two corresponding parameters are Q_1 and Q_2 in equations 3.6 and 3.7. The two parameters act on both ω_1 and ω_3 axes, Q_1 linearly and Q_2 quadratically in the frequency values (Eq. 3.5, 3.6, 3.7). The parameters are adjusted until the projection of the 2D spectrum on ω_3 matches the pump-probe spectrum[45]. Figure 3.9 shows the pump-probe spectrum (with opposite sign) of the Rhodamine 800 in methanol and the projection on the probe axis ω_3 of the 2D map of the same sample. The agreement is very satisfactory; if we compare the results of Figure 3.9 to those reported in the literature for the same sample [46], we notice a clear improvement obtained with our minimization procedure. These data will be discussed later.

Chapter 4

Ultra-broadband Pulses Characterization and Compression

4.1 Introduction

The Non-collinear Optical Parametric Amplifier (NOPA) generates pulses with very broad bandwidth, that are potentially extremely short. The transform-limit duration for a laser pulse is the minimum duration compatible with a given bandwidth; in order to get as close as possible to this value, the phase characteristics of the ultra-broadband pulses generated with the NOPA must be accurately controlled. In particular, we determined the frequency dependance of the phase of the NOPA output by means of time resolved Optical Kerr Effect (OKE). In our set-up a vertically polarized NOPA pulse acts as the OKE probe. It reaches the monochromator and the array detector after passing through a crossed polarizer (the *analyzer*) that completely extinguishes its intensity. In the presence of a pump pulse, polarized at 45 degrees from the probe polarization direction and overlapped to the probe inside the Kerr medium (1 mm thick fused silica plate), the induced transient birefringence changes the polarization state of the probe beam. Consequently, a fraction of it is transmitted by the *analyzer*, is dispersed by the monochromator and measured by the array detector. In our first attempt we used

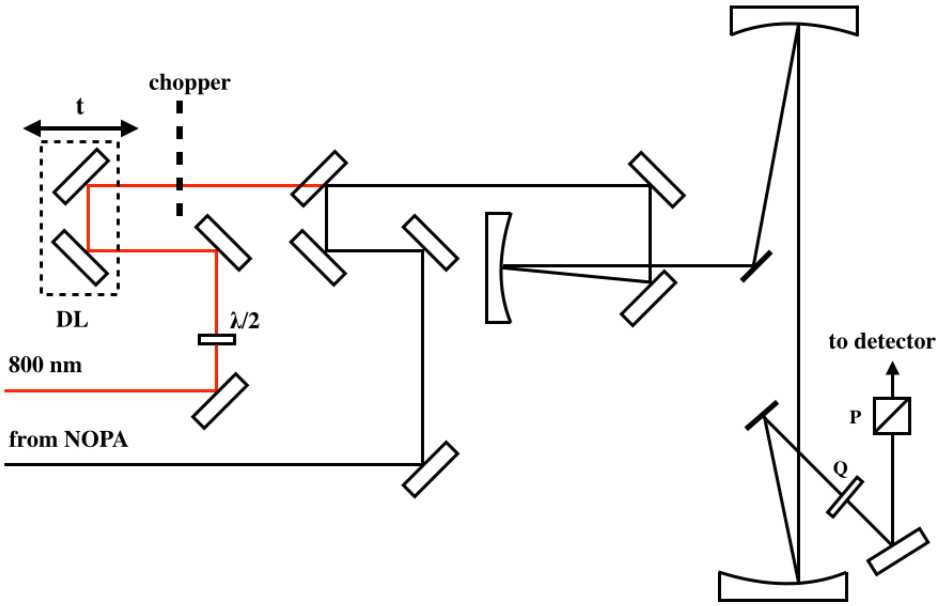

Figure 4.1: Setup modified for kerr measurements. $\lambda/2$ = half-wave plate. Q = 1 mm thick quartz plate. P = polarizer.

part of the photon echo set-up of Figure 2.3; we obtained the pump and the probe beams by splitting in two the NOPA output. Unfortunately, the OKE signal resulted too weak for our detection system. Then We, modified the set-up (see Figure 4.1) by sending in the pump arm of the set-up a fraction ?? of the 800 nm fundamental from the regenerative amplifier. A $\lambda/2$ plate was inserted on its path to rotate the polarization direction to the proper angle. Figure 4.2 shows the frequency resolved OKE signal measured as a function of the pump-probe delay time. The figure demonstrates that the NOPA pulses have a large group delay, of the order of 400 fs in the range of 410-580 THz (520-730 nm).

In the next sections I give a brief outline of the theoretical background about the phase dispersion of ultrashort laser pulses, and describe two different approaches that can be used to compensate for the chirping acquired by the pulse during the amplification stage. The first method makes use of a couple of SF10 dispersion prism. The second one adopts a couple of commercial Dispersion Compensating Mirror (DCM). On the basis of the comparison

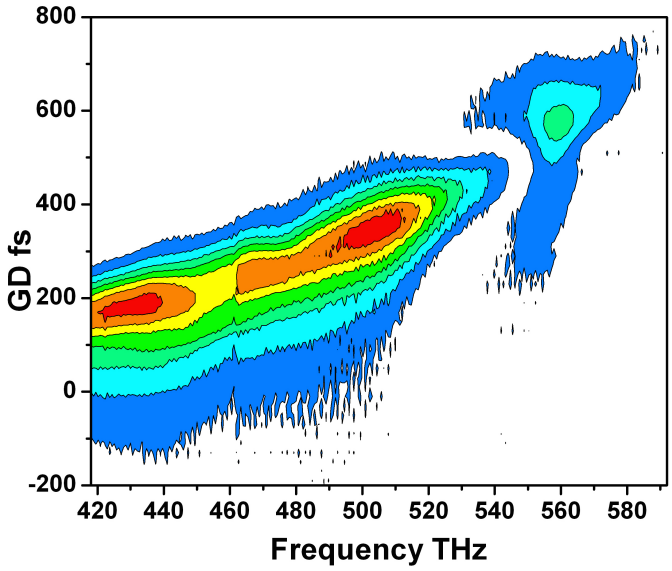

Figure 4.2: Group Delay of the amplified pulses output from the NOPA. This data are recorded with a 800 nm 35 fs gate pulse.

of the methods, I give the justification of the final choice adopted here.

4.2 Theory

The electric field of a light pulse with Gaussian time profile and central frequency ω_0 is written as:

$$E(t) = \sqrt{A_t e^{-ln2(\frac{2t}{\Delta t})^2}} e^{-i(\omega_0 t + \theta(t))} + c.c. \tag{4.1}$$

where A_t is the amplitude of the pulse and $\theta(t)$ is the phase in the time domain. $\theta(t)$plays a crucial role in determining the pulse broadening in dispersive media; it can be thought as adding a complex width to the Gaussian envelope of the pulse.

When dispersion is included in equation 4.1 for a pulse traveling in a dispersive medium, the time domain is no more the most convenient for describing the underlying physics. It is preferable to move to the frequency domain. Taking into account that convolutions become products upon Fourier transformation, the Fourier transform of equation 4.1 yelds[47, 48]:

$$E(\omega) = \sqrt{A_\omega e^{-ln2(\frac{\omega-\omega_0}{\Delta\omega})^2}} e^{-i\varphi(\omega-\omega_0)} \tag{4.2}$$

Equation 4.2, in which negative frequencies are omitted, describes the field of a pulse with central frequency ω_0 and Gaussian spectral profile with width $\Delta\omega$. The frequency domain phase $\varphi(\omega - \omega_0)$ describes the relation between the spectral components of the pulses. When the incoming pulse, $E_{in}(\omega)$, passes through a dispersive medium, the material adds a certain phase to the field. From the mathematical point of view this is expressed as the product of the incoming field and the response of the material $R(\omega)$:

$$E_{out}(\omega) = E_{in}(\omega)R(\omega)e^{-i\varphi_M(\omega-\omega_0)} \tag{4.3}$$

where $\varphi_M(\omega - \omega_0)$ is the spectral phase added by the material, and $R(\omega)$ is an amplitude scaling factor which for transparent media con be well approximated to the unity.

Usually, the spectral phase is expressed as a Taylor expansion around the carrier frequency:

$$\varphi(\omega - \omega_0) = \varphi_0 + \varphi_1 \cdot (\omega - \omega_0) + \varphi_2 \cdot \frac{(\omega - \omega_0)^2}{2} + \varphi_3 \cdot \frac{(\omega - \omega_0)^3}{6} + \dots \tag{4.4}$$

Assuming that the added phase is proportional to the travel length L in the medium: $\varphi(\omega) = k(\omega)L$, and taking in mind that the group velocity is: $v_G = d\omega/dk$, it is easy to see that the first term in equation 4.4 adds a constant phase. The second term is proportional to $1/v_G$ and adds delay to the pulse. No one of these terms affects the shape of the pulse. However, the third one, referred to as the Group Delay Dispersion (GDD), is proportional to $\frac{d}{d\omega}\left(\frac{1}{v_G}\right)$. It introduces a delay which is different for the different spectral components of the pulse. The fourth term, referred to as Third Order Dispersion (TOD), adds a frequency dependant quadratic phase to the pulse.

Figure 4.2 shows that the group delay GD has a non-linear dependance on the frequency. Then we have to consider, at least, both the GDD and TOD terms.

4.3 SF10 Prism Compression

It is easy to see that angular dispersion introduces negative GDD and TOD. This effect can be realized by a sequence of prisms or, for large dispersion,

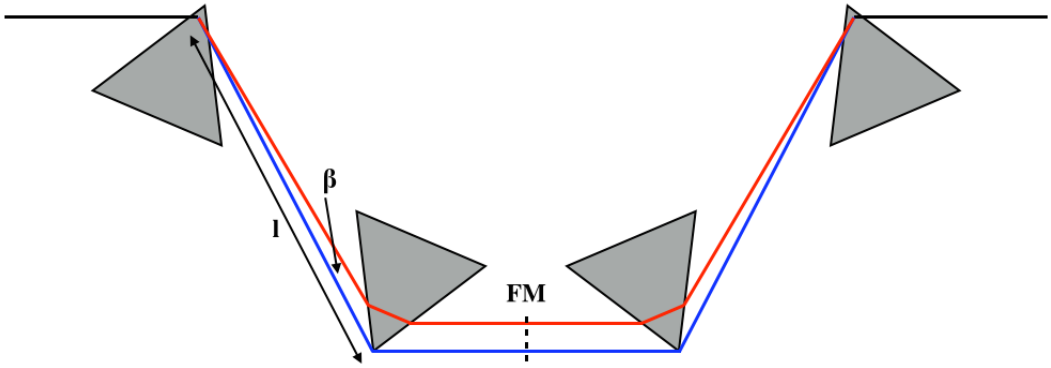

Figure 4.3: Four prisms compressor geometry. FM indicates the position of the folding mirrors in the two prisms-folded variation.

by a sequence of gratings. The unfolded geometry for the prism compressor consists of a four prism sequence shown in Figure 4.3. The apex angle of each prism is equal to the Brewster angle for the central frequency of the light beam and the prisms are arranged in such a way that the beam enters and exits each prism under Brewster angle. The reflection losses in that case are minimized for the P polarization. The first prism disperses the beam and the second one collimates it. The third and fourth prisms compensate for the action of the first two so that the beams entering and exiting the compressor are spatially identical. The last two prism can be removed and

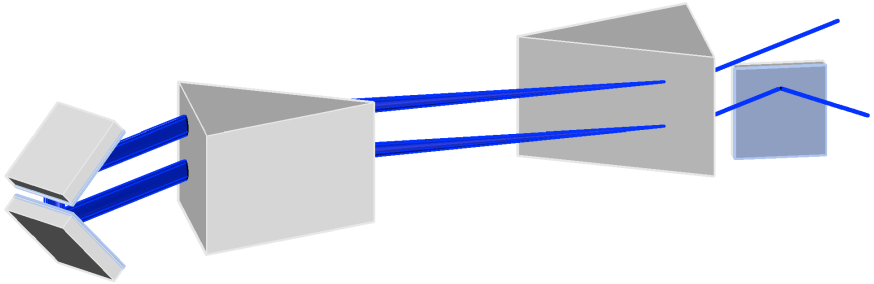

Figure 4.4: Experimental setup of a prism compressor in double pass geometry with folding mirrors.

substituted by folding mirrors to adopt a two prism double pass geometry configuration (Fig 4.4). It is easily shown that the wavelength dependent

path due to dispersion is given by:

$$P = 2lcos(\beta) \tag{4.5}$$

where l is the distance between the apex vertex of the two prisms and β is the wavelength dependent angle of the dispersed beam after the first prism. A detailed theoretical description of the second and third order phase dispersion introduced by a pair of prisms for an ultrashort laser pulse is given by Ramirez-Corral et al[49]. In particular, they give the equations describing the GDD and the TOD terms in the Brewster angle approximation:

$$\begin{aligned} GDD_{prism} =& \frac{L_g}{c}\Big(2\frac{dn}{d\omega}\Big|_{\omega_0} + \omega_0\frac{d^2n}{d\omega^2}\Big|_{\omega_0}\Big) \\ & - \frac{L_g\omega_0}{cn^3}\Big(\frac{dn}{d\omega}\Big|_{\omega_0}\Big)^2 - \frac{4\omega_0 L}{c}\Big(\frac{dn}{d\omega}\Big|_{\omega_0}\Big)^2 \end{aligned} \tag{4.6}$$

$$\begin{aligned} TOD_{prism} =& \frac{1}{c}\frac{dL_g}{d\omega}\Big(2\frac{dn}{d\omega} + \omega_0\frac{d^2n}{d\omega^2}\Big) + \frac{L_g}{c}\Big(3\frac{d^2n}{d\omega^2} + \omega_0\frac{d^3n}{d\omega^3}\Big) \\ & - \frac{L_g}{cn^3}\Big(\frac{dn}{d\omega}\Big)^2 - \frac{\omega_0}{cn^3}\frac{dL_g}{d\omega}\Big(\frac{dn}{d\omega}\Big)^2 + \frac{3L_g\omega_0}{cn^4}\Big(\frac{dn}{d\omega}\Big)^3 \\ & - \frac{2L_g\omega_0}{cn^3}\frac{dn}{d\omega}\frac{d^2n}{d\omega^2} + \frac{sL_g\omega_0}{cn^6}\Big(\frac{dn}{d\omega}\Big)^3 - \frac{4L}{c}\Big(\frac{dn}{d\omega}\Big)^2 \\ & - \frac{4\omega_0}{c}\frac{dL}{d\omega}\Big(\frac{dn}{d\omega}\Big)^2 - \frac{8\omega_0 L}{c}\frac{dn}{d\omega}\frac{d^2n}{d\omega^2} + \frac{8L\omega_0}{cn^3}\Big(\frac{dn}{d\omega}\Big)^3 \\ & - \frac{16L\omega_0 n}{c}\Big(\frac{dn}{d\omega}\Big)^3 \end{aligned} \tag{4.7}$$

Those equations are expressed as function of parameters like distances between the apex vertex (L), quantity of glass crossed by the beam in the first prism (L_g), refractive index of the material (n) and speed of light (c). Using them we wrote a code, in Matlab® language, to simulate the behaviour of the compressor applied to the dispersion of our amplified pulse.

The simulation's results are shown in Figure 4.5. Each panel reports the guess GD of our pulse (black line), the total GD for the SF10 prism compressor taking into account the GDD and TOD factor (green line) and the residual GD after the compression stage (red line). Each simulation is performed at different central wavelength from 580 nm up 680 nm. From the zooms collected in Figure 4.6, we can pinpoint some features of this kind of compressor. First, it is evident that the compressor efficiency is not the

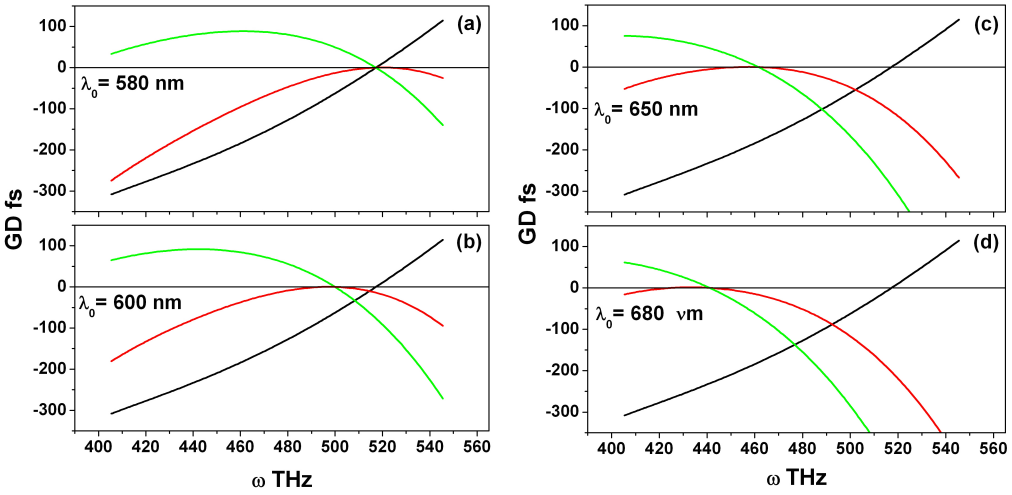

Figure 4.5: Simulation results for the SF10 prism compressor. The black line represent the dispersion of our pulse. The green line is the total dispersion for a couple of SF10 prisms and the red line is group delay residual after the compression. All the simulation are performed at different central wavelength as shown inside the graphics.

same throughout the pulse spectrum: it is higher in the red than in the blue region. In any case, the residual phase is too much for the requirements of our experiments. Some comments are needed. In this simulation I took into account the dispersion of the broadest band I can generate with the NOPA under the best alignment condition. Real experiments do not require such broad band. In all the experiments reported in literature the bandwidth varies approximately from 50 to 120 nm, depending on the region of interest and on the type of compressor used. Consider the panel (c) in Figures 4.5 and 4.6. It is easy to see that for a pulse centered at 650 nm if the band is limited to $\sim$ 80 THz ($\sim$ 100 nm in this region), the residual dispersion is approximately 40-50 fs. With this setup we performed some measurements, that will be presented later, on Rhodamine 800 in methanol, aimed to reproduce the measurement recorded by Scholes and Co[46]. The results were very satisfactory. However when we repeated those measurements on Cresyl Violet, the results were unsatisfactory. In fact, the two samples absorb in different visible regions: Rhodamine absorption is located more in the red region, where our prism-compressor works fine. The Cresyl Violet absorbs

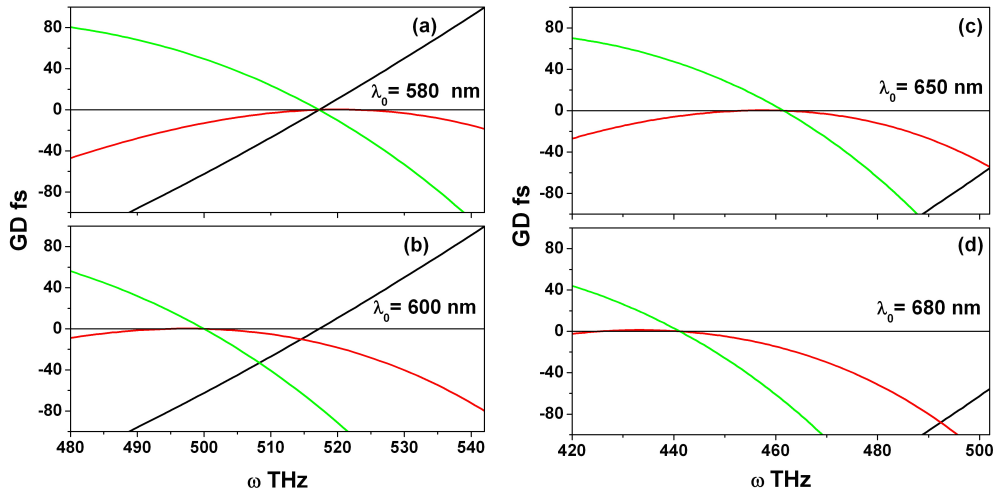

Figure 4.6: Zoom of figure 4.5.

more in the blue range, where this kind of compressor is much less efficient. In order to find the conditions for a satisfactory Group Delay compensation in a broader spectral window, we decided to simulate the behaviour of a compressor based on a couple of commercial Dispersion Compensating Mirror (DCM).

4.4 Dispersion Compensating Mirror Compressor

The dispersion compensating mirrors (DCM), or commonly, *chirped mirror*, are multi-dielectric layered mirrors. A normal dielectric mirror is transparent to light except for the wavelengths in a more or less narrow band around the one it is designed to reflect. Overlapping different dielectric layers at specific depth is possible to create dielectric mirrors for a wide range of wavelengths. As the light reflected from a deeper layer travels a longer path respect to that reflected from on outer one, a phase difference sets up between the two components. Special design of the dielectric layers deposition can realize a mirror able of introducing a negative dispersion; differences in thickness of these layers allow to operate on GDD and TOD at the same time. It is thus possible to recover the positive dispersion acquired by a laser pulse

passing through a medium. The mirror we choose are the DCM10 mirrors from Veneteon®. In the following section I report the simulation done using the mirror parameters given in the website of the company.

4.4.1 Simulation

The specifications given by the company include the graphs of the measured GDD (fs^2) and the reconstructed GD (fs) for the couple. Starting from the GDD data I reconstructed the GD with a numerical integration and I fitted it with a third order polynomial. In the upper panel of Figure 4.7 are shown

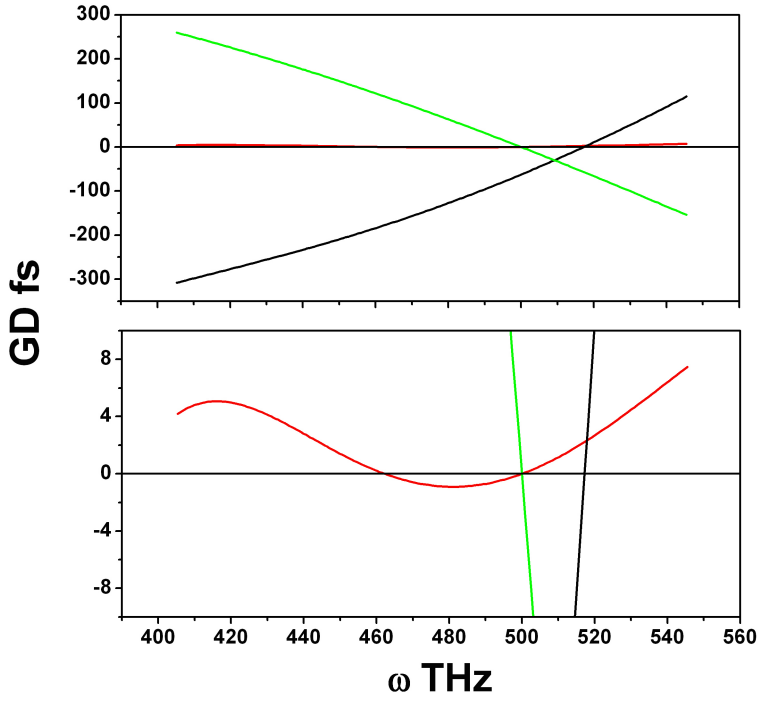

Figure 4.7: On top the result of the simulation with Venteon® DCM10. On the bottom a zoom near the GD values equal to zero. The black line represent the dispersion of our pulse. The green line is the total dispersion for a couple of DCM10 after 9 bounces and the red line is group delay residual after the compression.

the results obtained for a couple of Venteon® DCM10 mirrors. The black line represents the dispersion of the pulses from the NOPA. The green line is the GD of the DCM after 9 bounces and the red line is the residual GD after the DCM compressor. The large improvement with respect to the results

of figure 4.5 is evident. The lower panel shows a zoom of the same graph. This simulation demonstrates the extremely different efficiency of the two compressors. In Figure 4.7 the GD of the compressed pulse for the whole spectrum (from 400 to 550 THz, 550-750 nm) is about 10 fs. The residual GD (red line) is not perfectly flat, but we have to consider that the DCM mirrors are not custom made for the dispersion of our pulses. The residual dispersion predicted by our simulation appears tolerable for the requirement of our experiments.

Figure 4.8 is a pictorial representation of the structure of the compressor adopted for the echo experiments.

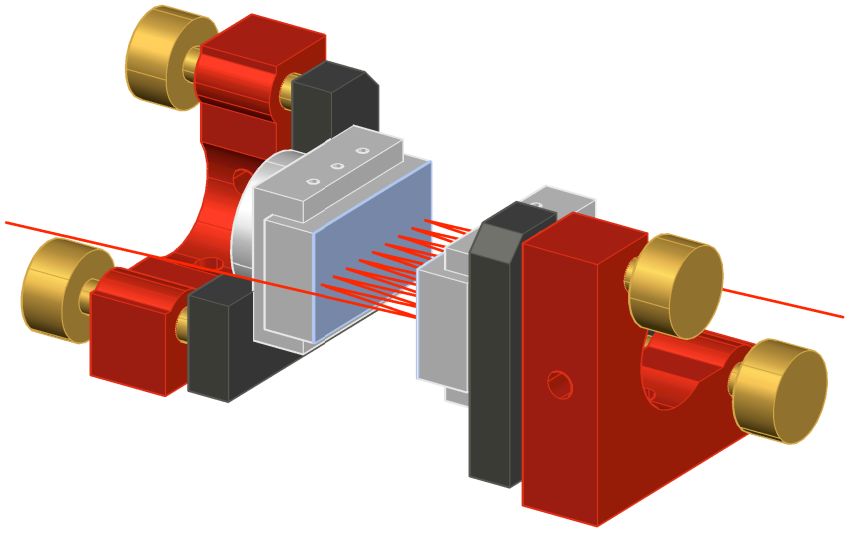

Figure 4.8: Experimental setup for the DCM compressor. Our simulation indicates that nine bounces are needed for optimal compression.

4.4.2 Compressed Pulses' Characterization

After the compression the peak power of our pulses is extremely higher respect to the un-compressed ones. For this reason we modified the OKE set-up using the beam from the compressor both for pump and probe branches as shown in Figure 4.9.

I performed first the characterization of the NOPA pulse with the broadest possible band. This is the most demanding condition, which emphasizes the

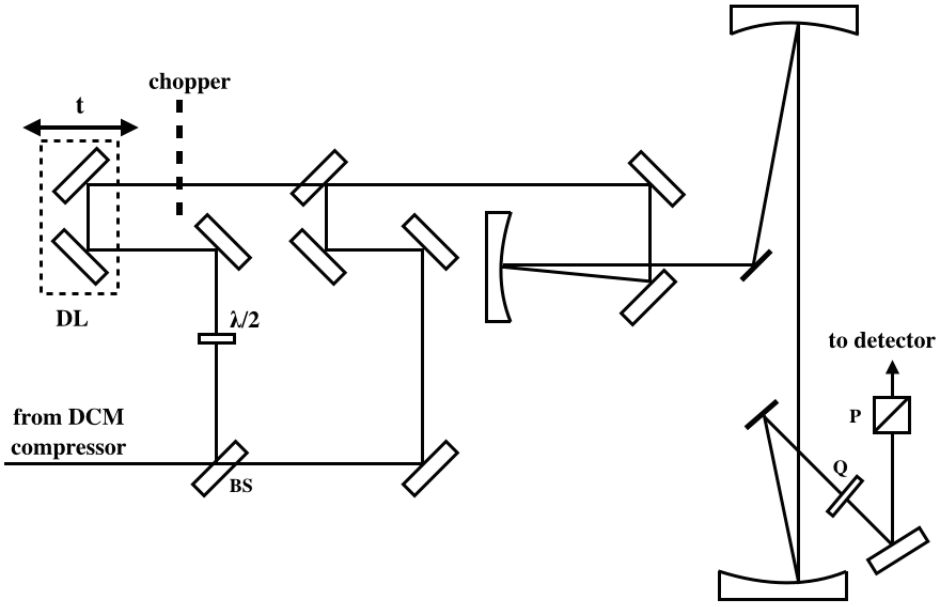

Figure 4.9: Setup modified for kerr measurements upon compressed pulses. BS = beam splitter,$\lambda/2$ = half-wave plate. Q = 1 mm thick quartz plate. P = polarizer.

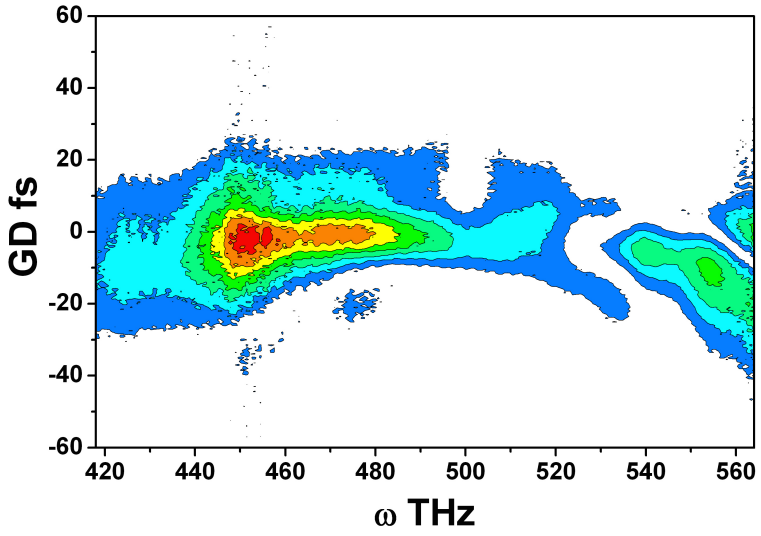

Figure 4.10: GD recovered after 9 bounces on the DCMs for the broadest amplified band generated with the NOPA.

impact of the DCM compressor.The GD measured for the entire band is shown in Figure 4.10. The comparison to Figure 4.2 demonstrates the high

efficiency of the compressor and the excellent phase recovery obtained.

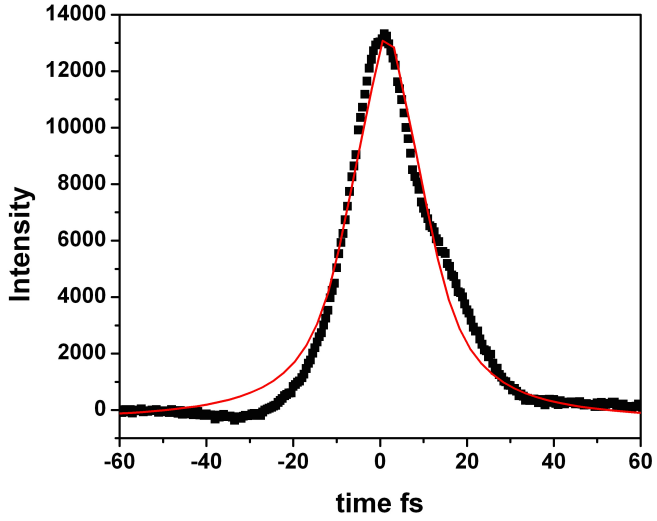

Figure 4.11: Cross correlation experimental data for the broadest band amplified with the NOPA (square dots). In red is superimposed the fit with $sech^2$ profile.

The GD is limited to approximately 20 fs and, considering that we are watching cross correlated data, this value is overstimated. In Figure 4.11 the cross correlation intensity profile, obtained by integrating Figure 4.10 with respect to the frequency, is presented. The filled square symbols are the experimental data, the solid red curve is the reconstructed fit with $sech^2$ profile. The FWHM of the cross correlation is 19 fs, corresponding to a pulse duration of approximately 12 fs. This pulse duration is still longer than the transform limited value for such a broad band. As reported in the literature, this limit can be approached by using active optics (like pulse shaper) or passive optics (i.e. DCMs) specially designed for the actual dispersion of the set-ups. The compression reached in Figure 4.10 is definitely enough for our purpose. Actually, we do not even need the entire band reported in the figure. In the next pages I will present the pulse characterization for narrower bands generated by the NOPA at different central wavelengths for use in 2D visible ultrafast spectroscopy applications.

All the measurements are performed via cross-correlation spectroscopy on a 1 mm-thick quartz plate with a time scan of 500 as. A $sech^2$ profile is used for the fits. The wavelength region covered goes from 520 nm to 780 nm

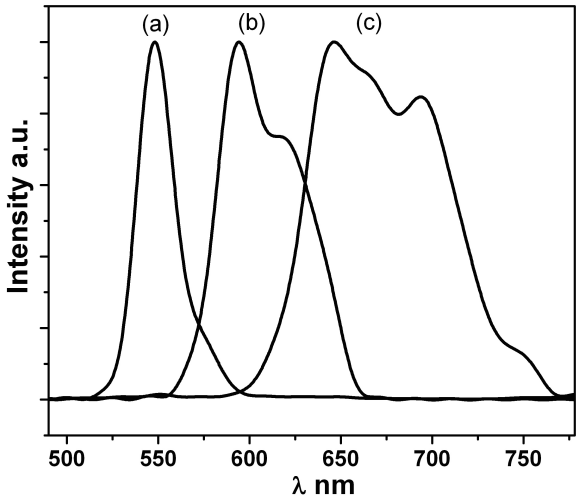

Figure 4.12: Amplified pulse spectra at different wavelengths; tuning of the NOPA is achieved by changing the pump-signal delay. The FWHM for the spectra are 45 nm (curve a), 70 nm (curve b) and 100 nm (curve c).

(Figure 4.12). The cross correlation results are presented in Figure 4.13. The scattered symbols represent the experimental cross correlation intensity, the red line is the data fit. The pulse durations reported in the graphs correspond to the cross correlation FWHM: they have to be scaled by a factor 1.54 (for a $sech^2$ shape) to get the pulse durations: 16 fs for Fig 4.13 (a), 18 fs for Fig 4.13 (b) and 14 fs for Fig 4.13 (c).

4.5 Considerations

We performed accurate simulations to predict the effective group delay compensation adopting two different compressors. The prism based one resulted unable to reach the desired low level of temporal dispersion. In particular, it is evident how the prism are not able to compensate the third order dispersion, especially on the blue side of the spectrum. This would imply a severe limitation in the bandwidth we can use in our experiments. The photon echo experiment is a degenerate four wave mixing, in which all the pulses have the same spectrum. Thus, all the spectral dynamics that can be measured in a 2D experiment is contained in the pulse band width. It is then crucial

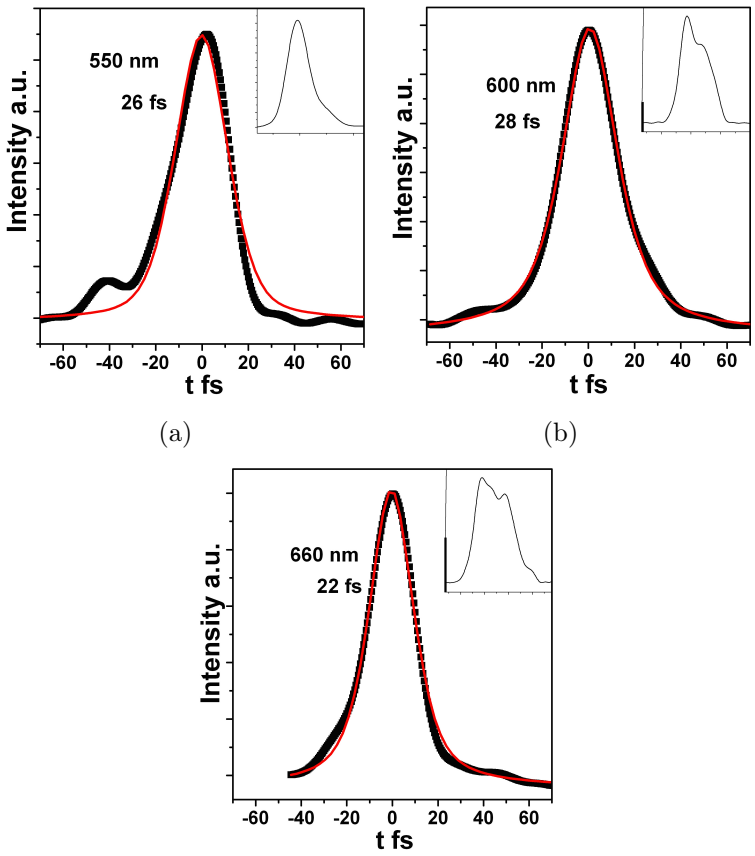

Figure 4.13: Auto correlation traces (scattered symbols), the corresponding spectra are shown as inset. Their best fit is shown as a red line with $sech^2$ shape. The reported time duration correspond to the FWHM of the correlation traces; they have to be scaled by a factor 1.54 to get the actual pulse durations. See text for details.

that pump and probe pulses have a bandwidth of at least 45-50 nm with a flat phase distribution. A compressor based on Dispersion Compensating Mirrors (DCMs) satisfies these requirements. In spite of the restriction due to the fact that its compression efficiency can be adjusted only by discrete steps (correspinding to the number of bounces), it allows us to compensate almost all the second and third order dispersion present after the amplification stage and to obtain a flat wavelength dispersion for bandwidth as broad as 100 nm.

Chapter 5

Rhodamine 800

5.1 Introduction

Once verified the good efficiency of the pulse compression, a field test was required of the Echo set-up. In particular it's mandatory to verify the accuracy and the reliability of the reconstruction of the echo 2D map. To this purpose, a good candidate is a molecule which absorbs in the 500-700 nm spectral range, and has more than one absorption band, in order to verify if the map reconstruction locates the various bands at their exact positions. Last but not the least, we should have reliable literature data to check our results. I decided to repeat the measurement performed by Anna and co [46], who recorded the 2D photon echo spectrum for Rhodamine 800 (Fig. 5.1) in methanol, at the fixed population delay time of 200 fs. The electronic

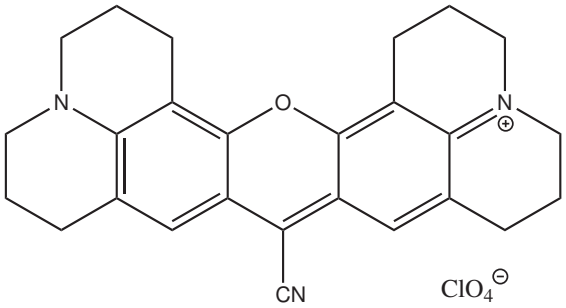

Figure 5.1: The Rhodamine 800

absorption spectrum in the visible range of the Rhodamine 800 is shown in

Figure 5.2. A vibronic progression is clearly visible on the blue side of the main peak; in particular, we consider the two intense bands, centered at 620 and 680 nm respectively, the two electronic components are clearly coupled; this implies the presence of cross peaks in the bi-dimensional map. These

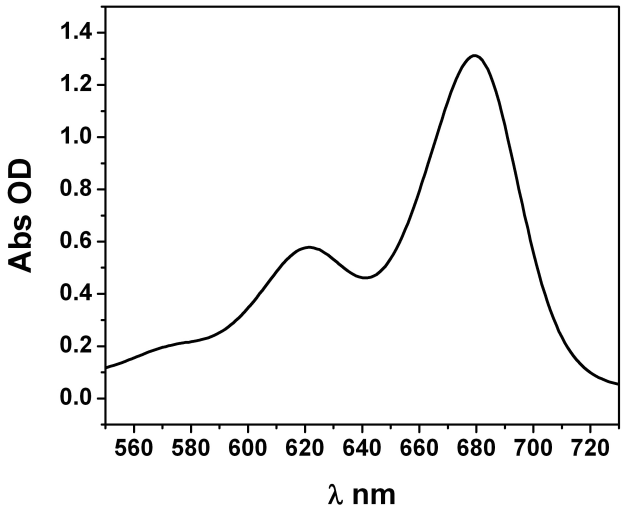

Figure 5.2: Linear absorption spectra of Rhodamine 800 in methanol. The two band we are interested in are centered respectively at 620 and 680 nm.

spectral properties make Rhodamine 800 a good candidate for a measurement which should pinpoint the efficiency of our set-up and of our codes for the data analysis.

5.2 Pump-Probe Spectrum

The broad band pump-probe transient spectrum for the Rhodamine 800 dissolved in methanol at 200 fs delay time is presented in Figure 5.3. The two bleaching bands are well evident, centered respectively at 620 and 680 nm. Furthermore, an excited state absorption (ESA) band is shows up at 585 nm. Our spectrum is absolutely consistent with the one reported in Ref. [46]; it confirms that we are working in the same experimental condition of the authors, so that we can use their echo measurements as a probe of our procedures.

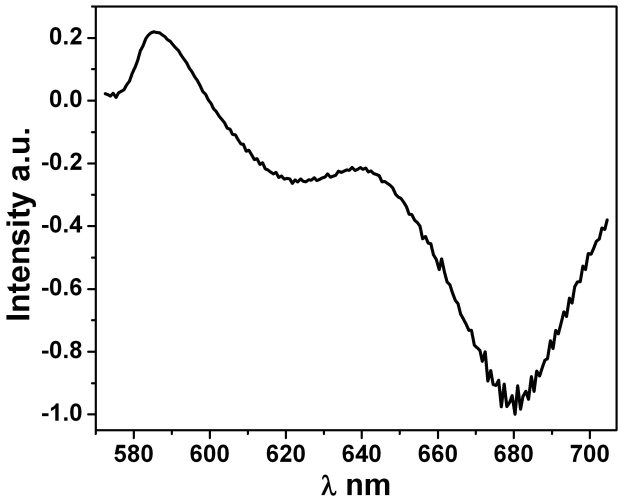

Figure 5.3: Broad band pump-probe transient spectrum for Rhodamine 800 in MeOH at 200 fs delay time.

5.3 2D Photon Echo

We performed all our 2D experiments at a population time of 200 fs, the same delay time adopted by Anna et al.[46].

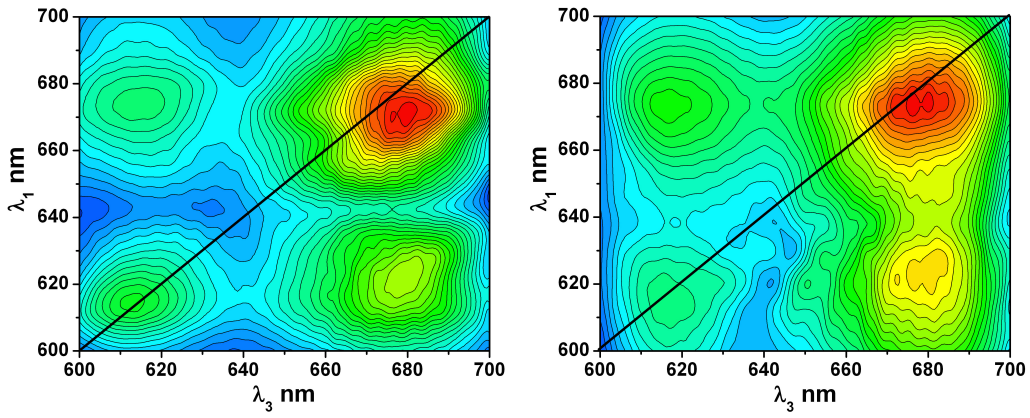

(a) Rephasing (b) Nonrephasing

Figure 5.4: (a) Rephasing and (b) Nonrephasing spectra measured for the Rhodamine 800 in MeOH at $t_2 = 200$ fs.

Before to considering the 2D echo map, it is interesting to have a look to the Rephasing and Non-rephasing contributions respectively. The two

spectra are recorded independently and the data treatment is the same. The absolute value of the two spectra are shown in Figure 5.4. Focusing first on the diagonal peaks, we notice that the band at 680 nm is actually in the expected position for both contributions (Fig. 5.4 a and b). On the other hand, the band that should be at 620 nm is at slightly lower wavelength. This discrepancy is due to the nature of the data plotted. In fact, in Figures 5.4 (a) and (b) I present the absolute values of the spectra; a little blue shift is produced by the nearby excited state absorption (approximately at 585 nm) which, having opposite sign respect to the bleaching (Fig. 5.3), moves the center of the resulting band, in the absolute values spectra, at a value in between the bleaching and the ESA wavelengths. The off diagonal peaks represent the coupling between the two fundamental bands.

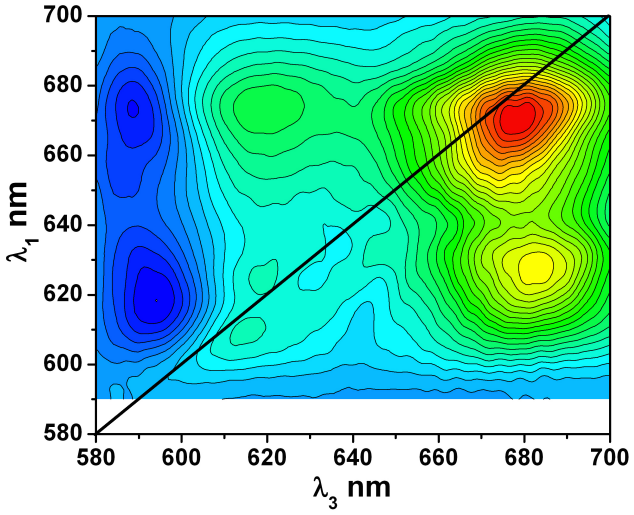

Figure 5.5: Absorptive Echo spectrum obtained from the data in Figure 5.4.

Figure 5.5 shows the absorptive 2D echo spectra for the Rhodamine 800 in MeOH at $t_2 = 200$ fs. In this figure the diagonal peak corresponding to the lower wavelegths bleaching band is in the correct position (620 nm); the ESA contribution shows up at 585 nm as off-diagonal peak. The absorptive spectrum in Figure 5.5 is in very good agreement with the data reported in Ref. [46]. We can conclude that we are able of performing photon echo experiments and of extracting reliable 2D spectra in a spectral window broader than 100 nm. A further test to verify that the treatment we applied to the

row data is correct, consists in applying the projection theorem, i.e. in verifying that the projectionof the 2D spectrum on the probe axis (the λ_3 axis) matches the pump-probe spectrum. I already discussed this check in the code analysis chapter, the comparison is shown in Figure 3.9.

5.4 Conclusion

I measured the photon echo spectrum on Rhodamine 800 in methanol at the population time $T_2 = 200$ fs and compared my results to existing literature data[46]. The purpose of this measurement was of verifying the effective ability of our setup to perform reliable measurements and of checking the correctness and efficiency of our codes for the absorptive spectrum reconstruction. The results are extremely encouraging; in particular I obtained a perfect 2D map of the absorptive spectrum, very close to that reported in the Ref. [46]. Actually, the projection of the 2D spectrum on the probe axis sows that our fit of the pump-probe spectrum is definitely better than that reported by those authors. This means that our code acts on the proper experimental parameters with a correct procedure.

Chapter 6

Cresyl Violet

6.1 Introduction

In the previous chapter we checked the efficiency in reconstructing the 2D map of our codes. An additional point to be verified is the long term stability of the entire set-up. This is a crucial aspect, in view of the long time required (typically more than 12 hours) to complete an experiment where the population time is scanned over several picoseconds.Cresyl Violet (Figure 6.1) is an excellent test molecule to this purpose for several reasons. It

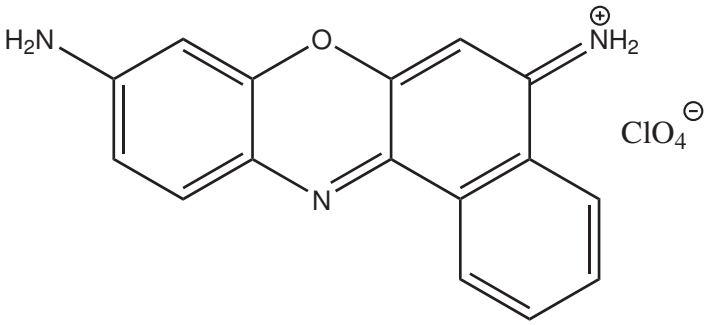

Figure 6.1: The Cresyl Violet.

is an organic compound commonly used in biological and medical fields as histological stain. Other application are in the laser field used as laser dye for pulsed and current wave operation. The Visible spectrum of Cresyl Violet dissolved in methanol is shown in Figure 6.2. It consists of a main absorption

band centered at 600 nm and of a shoulder on the blue side (approximately at 565 nm), generally attributed to a vibronic progression. Our interest on

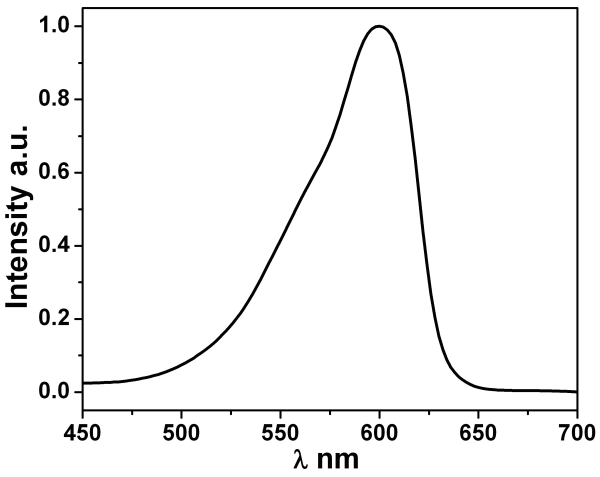

Figure 6.2: The Visible spectra of the Cresyl Violet dissolved in methanol.

this molecule is due to the simple structure of its spectrum in the region accessible to the NOPA emission and due to important physical-chemical properties found in literature. In particular Turner and co. [50] performed 2D visible measurements at different population time for this molecule dissolved in methanol, from their kinetic data are well visible the oscillations due to the vibronic coupling. In this chapter I report on the results of our measurements, made especially to test and verify the long term stability of our set-up. This test is crucial to validate the results obtained when the experiments involve spectral dynamics in the picosecond range.

6.2 Pump-Probe Spectra

Figure 6.3 reports the spectrum of the NOPA emission used for all the measurements: broad band pump-probe, transient grating and 2D echo.

Figure 6.4 (a) shows the map of the broad band pump-probe experiment, reporting the intensity as function of time and wavelengths, while Figure 6.4 (b) reports a slice of the previous map taken at 605 nm. From these figures it is evident that, from the spectroscopic point view, the peculiarity for this molecule resides in the strong vibronic coupling of the two bands shown in

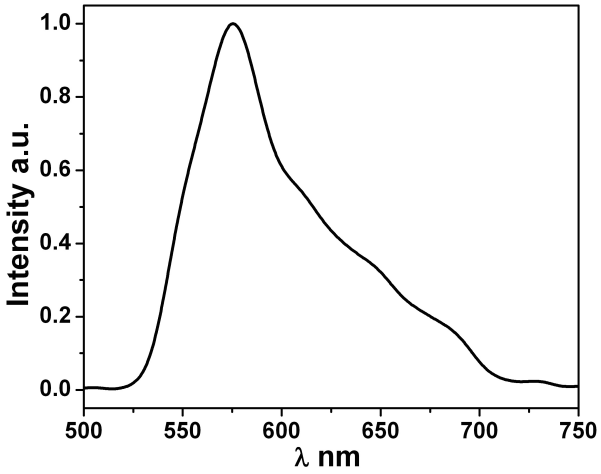

Figure 6.3: Output band from the NOPA.

Figure 6.2 manifested in the time resolved measurements (Fig. 6.4 a and b) as oscillations whose frequency is equal to the energy separation of the two band. The transient absorption spectra of this molecule don't reveal any

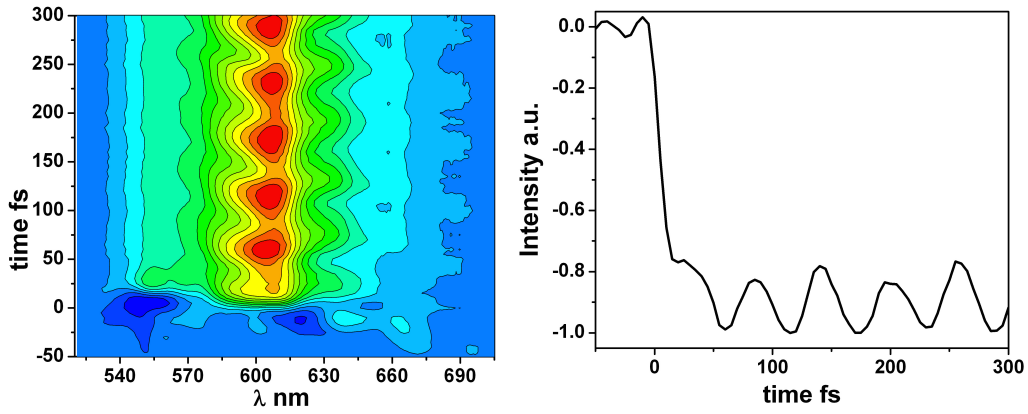

(a) (b)

Figure 6.4: (a) Broad band map for the Cresyl violet in MeOH. The oscillations due to the coupling between the to vibronic band are well evident. (b) Kinetic trace took at 605 nm of (a).

particular dynamics, besides the oscillations behaviour. The same oscillation is expected to be present in the four wave mixing experiments. Considering that the 2D echo measurements require approximately 40 minutes for a single

value of the population time, recording the oscillation over a t_2 time scan of 300 fs, takes about 20 hours. The reproducibility of the oscillations aver such a long time is a good test of the long term stability of our system.

6.3 Transient Grating

The transient grating 2D map was already shown in Figure 3.6. In the first 20 fs a red shift of the main absorption is well evident as reported in Ref. [50]. It is also possible to appreciate the oscillations alredy reported in Figure 6.4 (a). Figure 6.5 compares the kinetics at 605 nm from the transient grating experiment (black line) and from the pump-probe (red line); note that the latter is shown with inverted sign in the intensity axis.

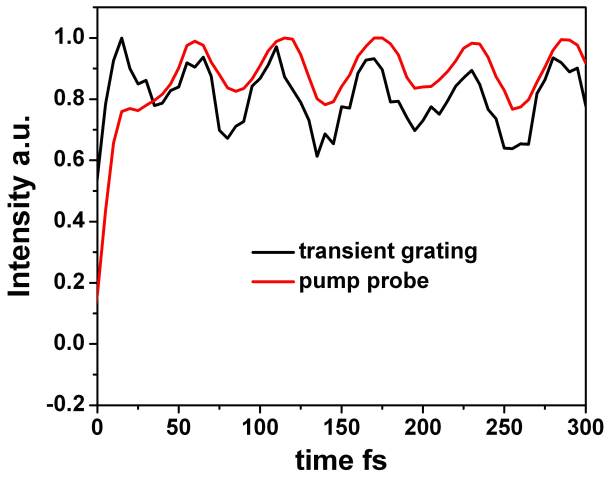

Figure 6.5: Comparison between the kinetic traces at 605 nm from the TG (black) and from the pump-probe(red). the pump-probe kinetic is multiplied by -1 for a better comparison.

6.4 2D Photon Echo

The 2D Photon Echo maps for the Cresyl Violet dissolved in methanol are shown in Figure 6.6 at selected population delay times. The 2D spectrum is dominated by the strong diagonal peak at 600 nm, the shoulder at 565 nm

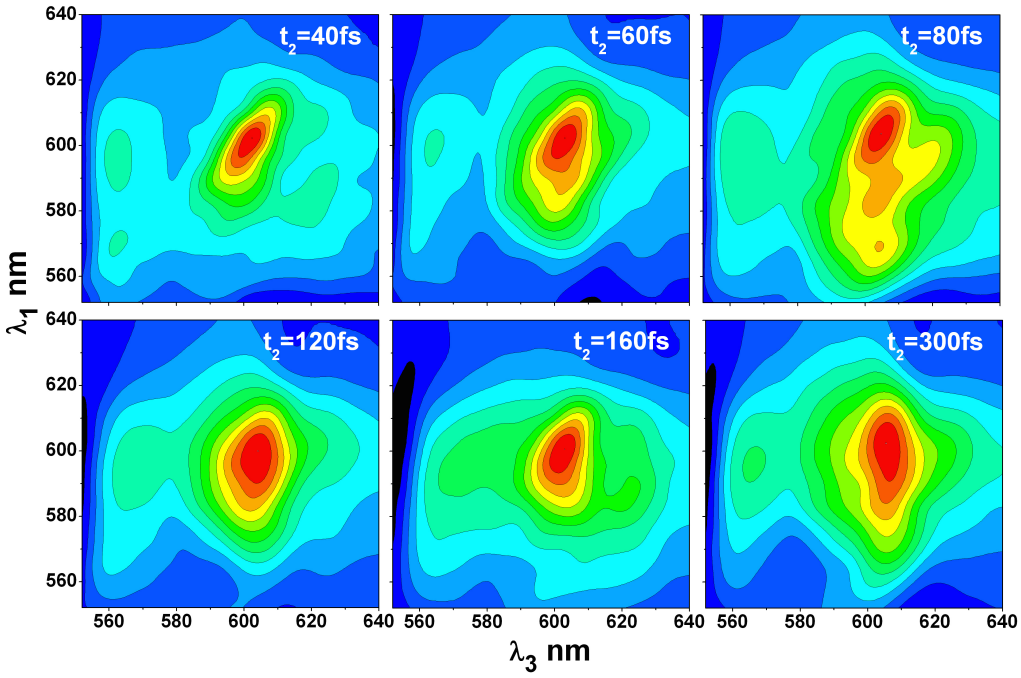

Figure 6.6: The 2D PE maps for the Cresyl Violet dissolved in MeOH at selected t_2 delay times.

is hardly visible. Well visible is the cross peak ($\lambda_1 = 600$, $\lambda_3 = 565$) due to the vibronic coupling of the two diagonal features. Figure 6.7 compares the intensities of the transient grating signal (taken at 600 nm), in black, and of the cross peak of the 2D spectrum, in blue, as a function of the population time t_2. It's well visible that the comparison of the two oscillations have the same period, but different phase which is shifted by π. This kind of inversion, due to the ground state wave packet dynamics [51], is a behaviour well known in literature, observed in 2D experiments [52] and in theoretical simulations [53].

Our measurements confirm the stability of the 2D echo apparatus in long term measurements ($\sim$ 20 hours). We reproduce exactly the oscillating pattern due to the vibronic coupling, by monitoring the intensity of an off diagonal peak, which represents the most sensitive, and often the most difficult to measure, spectral feature in a 2D map.

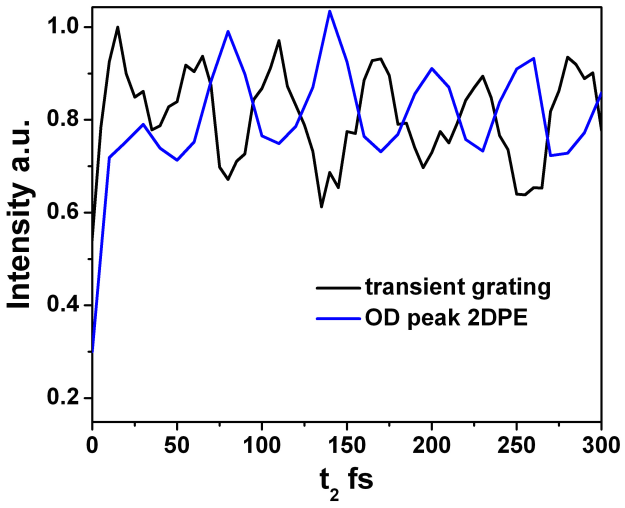

Figure 6.7: Comparison between the TG trace at 600 nm (black line) and the cross peak from 2D echo (blue line) at different t_2.

6.5 Conclusion

I performed steady state UV-Vis spectra in order to individuate the visible region of interest for this molecule. The spectrum (Fig. 6.2) shows a main absorption at 600 nm and a very weak shoulder on the blue side of the main absorption. The pump-probe spectra (Fig. 6.4) demonstrate a strong vibronic coupling, resulting in periodic variation of the intensity. This behaviour is present also in the four wave mixing experiments. The kinetic trace at 600 nm, taken from the Transient Grating experiments,compares well with that from the pump-probe spectrum (Fig. 6.5). The kinetic behaviour is well evident also in this measurement, and the oscillations observed in both cases match properly. Finally, the 2D echo spectra are performed and presented. In the 2D map (Fig. 6.6) the cross peak corresponding to the two main vibronic bands is well resolved. It's dynamics against t_2 is shown in Figure 6.7 together with that obtained from the Transient Grating experiments. The oscillation phase is inverted in the two cases, as observed in previous experiments and simulations[52, 53]; the period of the two oscillations matches each other properly. The observation that the periodicity of the oscillations is preserved in spite of the long ($\sim$ 20 hours) experimental time required to cover the entire t_2 window, confirms the stability of our system and makes

us confident that reliable dynamical data can be extracted from 2D maps.

Chapter 7

BODIPY Bi-Chromophore

7.1 Introduction

In nature the photosynthetic process is based on the solar light harvesting, made possible thanks to particular protein-pigment complexes called antenna complexes, whose excitation energy is finally transferred to the reaction center[54, 55]. Natural systems have an extremely high energy conversion efficiency, and understanding the factors that determine such a high efficiency is crucial for the engineering of new devices able of converting and storing solar energy.

The simplest model system for which energy transfer can be conveniently studied consists of two chromophores: the first absorbs light (the donor) and transfers energy to the second one (the acceptor). In order to make this communication possible, particular attention in the spectroscopic properties of the compounds involved is needed, the fluorescence of the donor must overlap the acceptor absorbtion in order to make the energy transfer possible.

Recently, researchers in the LENS' ultrafast laboratories investigated the ultrafast energy transfer in a bi-chromophoric molecular dye by means of Transient Absorption Spectroscopy (TAS)[56]. The molecule under investigation is composed by a styryl-pyridinium donor and a BF_2-chelated dipyrromthene compound (BODIPY) acceptor. The kinetics of the process, studied with femtosecond TAS in different solvents, revealed that the electronic energy transfer (EET) is quantitative and very fast. Although the

energy transfer process follows a multi-exponential behaviour, attributable to the presence of different geometrical conformers in solution, almost 70% of the overall excitation energy is transferred from the donor to the acceptor in the sub-picosecond time scale. While the ab-initio calculation of the intra-chromophoric energy transfer support the interpretation of the results in terms of a Förster mechanism, the limited time resolution of the used TAS experimental set-up is not able of resolving the dynamics on that fast time scale. 2D maps obtained from photon echo measurements (2D PE) have the advantage of bringing the time resolution to few tens of femtoseconds and, most of all, of giving access to important information, hidden to the TAS experiment, thanks to the expansion of the spectra into the second dimension. In the compound previously investigated, the UV spectrum of the styryl-pyrudinium moiety is characterized by a main broad absorption band centered around 490 nm, with a tail extending to 530 nm. Its fluorescence emission is centered at 640 nm, where the BODYPY acceptor absorbs. For a complete two-dimensional spectrum, coherent light pulses with a broad band, covering at least the 530-620 nm region, are required. Unfortunately, even though the NOPA in our lab is able of generating such pulses, the available compression stage is not efficient under 550 nm, according to the chirped mirrors (DCM) specifications. In addition, in the above mentioned bi-chromophoric molecule the link connecting the two moieties is highly flexible, so that several conformations are present in solution. This introduces a substantial degree of indeterminacy about the actual molecular structure and complicates the comparison of the experimental results with proposed energy transfer models.

For this reason, we decided to investigate a different bi-chromophoric molecule, based on two BODYPY units, which was purposely sensitized by Prof. Stefano Cicchi, from the Organic Chemistry Department of the University of Florence, to perform this kind of measurement.

In recent years the BPDIPY cromophores have attracted broad attention and often have been used as donor and acceptor molecules[57–62]. This success is due to their chemical stability and to their high absorption coefficients and high emission quantum yields. In addition, their spectral properties can be finely tuned acting on the substituents[63]. The molecule under inves-

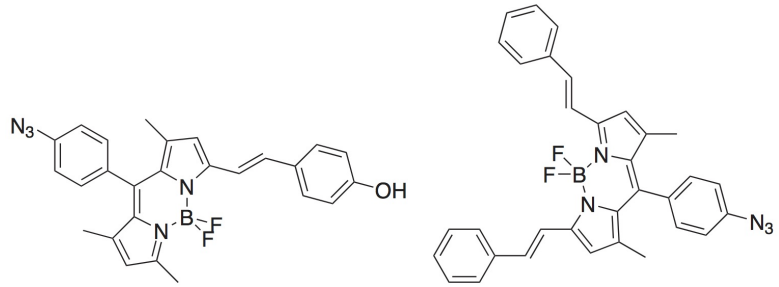

(a) donor

(b) acceptor

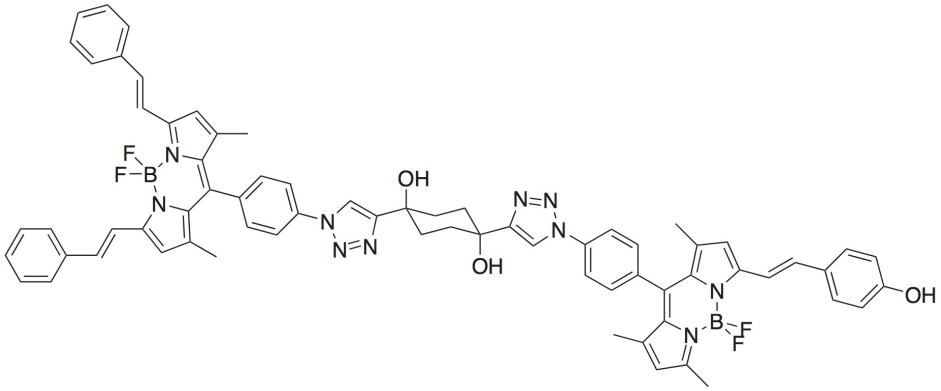

(c) bi-chromophore

Figure 7.1

tigation is composed by two different BODYPY units as shown in Figure 7.1, where (a) is the donor and (b) the acceptor. The BODIPY/BODIPY bi-chromophoric molecule is shown In Figure 7.1 (c). The donor and the acceptor are kept together by a rigid link, a 1,4 hydroxide cycle-hexane. Such a link is structurally rigid, as the two hydroxide groups block the chair conformation of the cycle-hexane and avoid the possibility of an inversion. The relative position of the two chromophores is then essentially fixed, the only degree of freedom being the rotation around the bonds connecting the tri-azo moieties to the cyclohexane.

In the next sections, the steady state measurements on the separate donor and acceptor, and on the bi-chromophore are presented. Then the Preliminary TAS measurements, performed on the bi-chromophore, are reported and discussed; finally, the 2D photon echo spectra are shown and discussed

and some conclusions are given.

7.2 Steady State Measurements

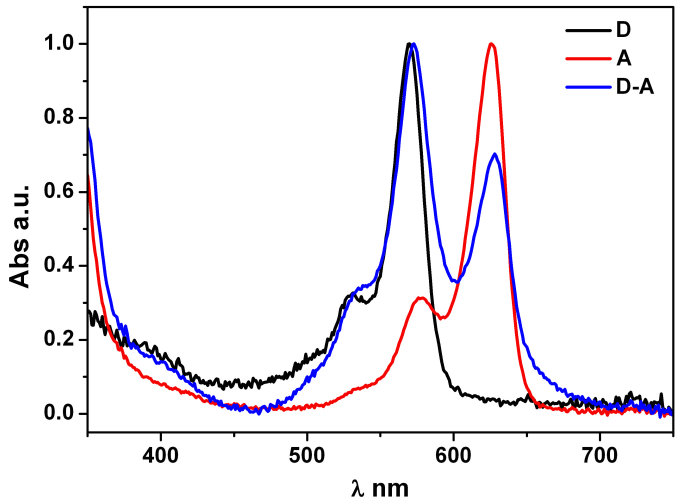

Figure 7.2: Comparison of the Visible spectra of the donor (black line) of the acceptor (red line) and of the bi-chromophore (blue line) dissolved in THF.

Figure 7.2 shows the visible spectra of the donor (black line), of the acceptor (red line) and of the bi-chromophore (blue line) dissolved in Tetrahydrofuran (THF). The donor spectrum is characterized by two narrow absorption bands centered at 530 and 570 nm, respectively. The acceptor shows the same spectral features but shifted by ~ 50 nm to the red: namely, their central wavelengths are at 576 and 625 nm. As expected, the spectrum of the bi-chromophore (blue line) in Figure 7.2 is, from a qualitative point of view, the sum of the spectra of the isolated donor and acceptor. However, one has to consider that the spectra of Figure 7.2 have been separately normalized, so that no direct comparison can be done of the band intensities in the three compounds. Actually, this subject deserves specific consideration and will be treated in the following.

Table 7.1 compares the absorption coefficients values obtained from the donor and the acceptor. Those in the first column are the values for the free chromophores independently dissolved in THF. The reported values

Table 7.1: Comparison of the absorption coefficients values for the donor and acceptor. In the first column are shown the values of the two molecule independently dissolved in THF. The last column reports the same value obtained from the bi-chromophore dissolved in THF.

	free molecule	bi-chromphore
Donor	$1 \cdot 10^4$	$1.5 \cdot 10^4$
Acceptor	$1 \cdot 10^5$	$1 \cdot 10^4$

correspond to the strongest absorption band of the visible spectrum (Fig. 7.2). The second column shows the corresponding values measured in the bi-chromophore complex, taken, respectively, at 570 nm for the donor and at 625 nm for the acceptor. There is a remarkable difference for the absorption coefficients of the free acceptor and for the acceptor when in the bi-chromophoric complex. When the two molecule are unbounded the acceptor's coefficient is one order of magnitude higher than that of the free donor. In the bi-chromophore the situation is inverted: the coefficient of the donor is 1.5 times greater than that of the acceptor. The fact that the absorbance in the region 580-620 nm of the acceptor linked in the bi-chromophoric compound, decreases by an order of magnitude with respect to the free chromophore, suggests that, if we excite the donor around 570 - 580 nm (i.e. on the maximum of its absorption band, see Figure 7.2) the contribution of the acceptor's direct excitation at that wavelength would be small.

This conclusion is supported by comparing the 2D photon echo map shown in Figure 7.3. In panel (a) I report the 2D PE for the acceptor dissolved in THF at a population time of 60 fs. The off-diagonal peak ($\lambda_1 = 570$ and $\lambda_3 = 625$ nm) is due to the coupling of the two vibronic bands of the acceptor (Fig. 7.2 (red line)). The 2D map leads out the extremely high efficient coupling between the two bands making the cross peak as the most intense in the map. Fig. 7.3 (b) presents the same measurement on the bi-chromophore at the same population time. The off diagonal band ($\lambda_1 = 570$ and $\lambda_3 = 625$ nm) is very weak. This is consistent with the data reported in Table 7.1: the absorption at the excitation wavelength $\lambda_1 = 570$ nm is

mostly due to the donor.

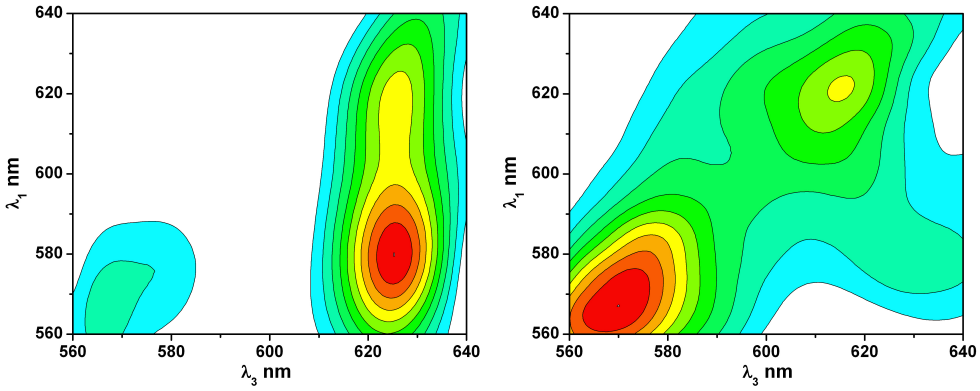

(a) Acceptor (b) Bi-chromphore

Figure 7.3: Comparison of the 2D PE spectra for the acceptor (a) and the bi-chromphore (b) in THF at a population time $t_2 = 60$ fs.

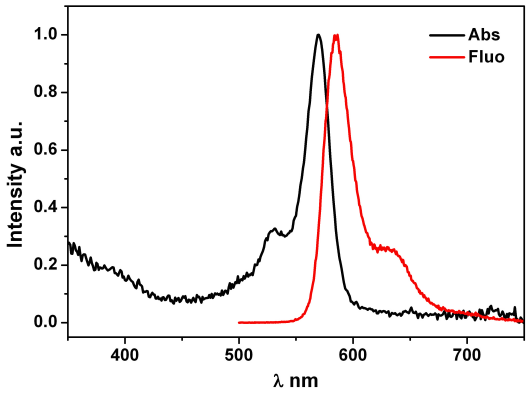

Figure 7.4: Comparison of the normalized visible absorption (black line) and the normalized fluorescence emission intensity (red line) spectra for the donor dissolved in THF.

Figure 7.4 compares the normalized visible absorption (black line) and fluorescence emission intensity (red line) spectra of the donor dissolved in THF. The fluorescence spectrum is characterized by an intense emission centered at 585 and a weaker one at 632 nm. The former is almost in resonance with the acceptor's absorption band centered at 576 nm, thus making the energy transfer between the two chromophores possible with a Förster type mechanism.

7.3 Transient Absorption Spectroscopy

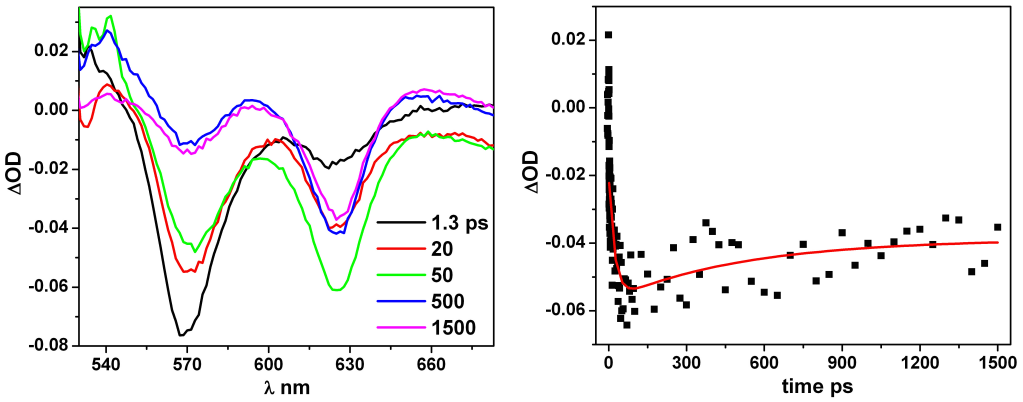

(a) (b)

Figure 7.5: (a) TAS spectra at selected delay times of the bi-chromophore dissolved in THF excite at 520 nm. (b) Scattered data reports the kinetic trace took at 625 nm and in red is reported its best fit.

Figure 7.5 (a) collects the Transient Absorption Spectra at selected picosecond delay times (as expressed in legend) upon an excitation at 520 nm. The six spectra are characterized by the two main bleaching bands centered at 570 and at 625 nm due to donor and acceptor cromophores, respectively. An excited state absorption (ESA) is also evident at 535 nm. Focusing on the donor absorption's region, some comments are possible: the bleaching at 625 nm reaches its highest intensity at 50 ps, probably due to the EET process, however this band is present already, for its $\sim$ 30%, at the first delay time reported (1.3 ps). This feature could be taken as an indication of an ultrafast energy transfer process taking place at early times; however, the TAS experiment cannot support this interpretation, as its limited time resolution does not allow accessing delay times significantly shorter than 1 ps.

Figure 7.5 (b) shows the kinetic trace taken at 625 nm (scattered symbols) and its best fit (red line). For the fit I used a bi-exponential function, in which the first time constant accounts for the rise of the signal, the second one for the decay. The best-fit value for the former is $\tau = 22 \pm 5$ ps.

As already noticed, some negative signal (bleaching) is present at 625

nm already at 1.3 ps (see Fig. 7.5 (a) black line), what could be attributed to some sub-picosecond energy transfer process, similar to that observed in the styryl-pyrudinium/BODIPY bi-chromophoric molecule of ref.[56]. The 2D PE experiment, employing light pulses as short as 20 fs, is expected to clarify this issue.

7.4 2D Photon Echo

We performed the 2D PE experiment on the BODIPY/BODIPY bi-chromophoric molecule of Figure 7.1 (c) by scanning the t_2 population time from 40 fs to 230 fs with 10 fs steps. The t_1 delay time between pulses E_1 and E_2 was scan from -10 to 130 fs, with 250 as steps. The energy transfer from the donor to the acceptor is expected to result in a cross peak whose relative intensity should rise with increasing t_2 population time.

Figure 7.6 (a) shows the 2D photon echo maps recorded at selected population delay time. The most intense band is the one on the diagonal, centered at 570 nm, consistent with the visible absorption spectra (Fig. 7.2 blue line) and all the 2D maps were normalized in respect to its intensity. All the 2D maps reported show a cross peak centered at $\lambda_1 = 570$ nm, $\lambda_3 = 625$ nm. Figure 7.6 (b) shows the kinetic trace of its intensity vs the population time t_2. This trace oscillates around a constant value very close to 0.2, suggesting the absence of any energy transfer, appreciable on this short time scale. More clearly: this measurements led out that if a dynamical process is present in this time scale, it is inside our signal-to-noise ratio and, actually, we are not able to observe it.

The presence of a bleaching band in the TAS spectrum at 1.3 ps (Fig. 7.5 (a) black line) is probably to be ascribed to a direct excitation of the acceptor around 570 nm, in the blue tail of its weaker absorption band (see red spectrum in Figure 7.2) in the bi-chromophore even though the pump pulse is centered at 520 nm. This conclusion can be supported observing the 2D maps in Figure 7.6 (a); in fact, the presence of the cross peak at $\lambda_1 = 570$ nm, $\lambda_3 = 625$ nm with constant intensity of 0.2 can be assigned to this direct excitation process, and the absence of a subsequent dynamic in the short time scale confirms this hypothesis.

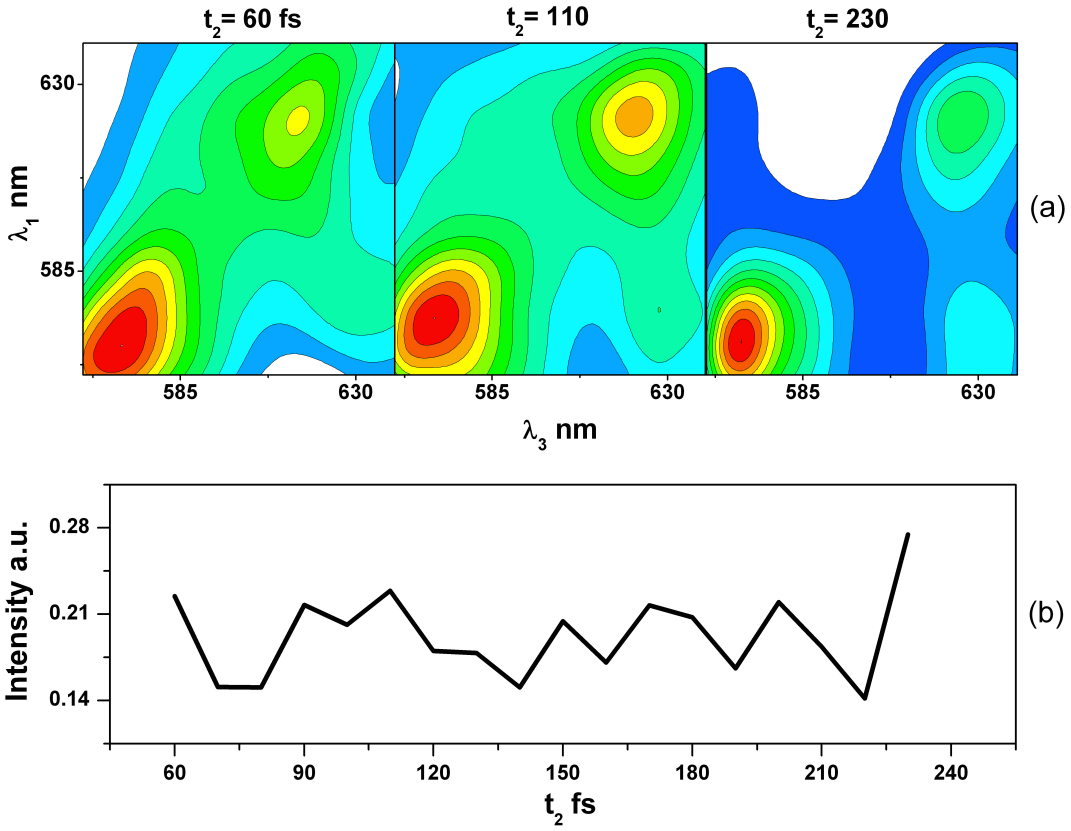

Figure 7.6: (a) Normalized 2D photon echo maps of the bi-chromophore dissolved in THF at selected population delay time. (b) Kinetic trace of the off diagonal peak centered at $\lambda_1 = 570$ and $\lambda_3 = 625$ vs the t_2 population time.

7.5 Conclusion

Comparing the results reported in Ref.[56] and the ones pinpointed with our measurements, some comments can be outlined. The molecule under our investigation is characterized by a rigid linker which limits to rather small angles the possible relative orientations of the two chromophores. Donor and acceptor moieties are bonded in equatorial position to cycle-hexane in chair conformation (Fig. 7.1 (c)), and the two hydroxide groups in axial position hinder large conformational changes of the two chromophores with respect to the cyclic linker. The transient absorption measurements (see Figure 7.5) provide convincing evidence that an appreciable donor-acceptor energy transfer takes place in few tens of picosecond (time constant 22 ps). Within the

Förster picture, this value is indicative of a rather slow and incomplete energy transfer, a finding that is in sharp contrast to that reported in Ref.[56] for a styryl-pyrudinium/BODIPY complex, a bi-chromophore having the same acceptor as the BODIPY/BODIPY molecule reported here, with a different donor unit. The main difference between the two compounds resides in the flexible linker adopted for the styryl-pyrudinium/BODIPY molecule of Ref.[56]. In that case, it is possible for the two chromophores to vary their relative orientation over a very large angular range. Being the conformational changes very slow in respect to the time scale we are considering, the transient absorption experiment probes an inhomogeneous distribution of different geometries. The calculation reported in Ref.[56] show that the most stable structure is the one where the two roughly planar chromophores are facing each other with parallel planes at very short distance ($\sim$ 10 Å). The short distance and the favorable angular geometry make the energy transfer very fast and efficient and account for the experimental observation that about 70% of the excitation energy is transferred to the acceptor with a sub-picosecond time constant.

On the contrary, the rigid structure of the linker in the BODIPY/BODIPY molecule, which forces the two chromophoric units to keep a rather unfavorable relative orientation at a larger distance, precludes any very fast energy exchange mechanism and leads to the rather slow (22 ps time constant) and incomplete transfer that we measured in our experiments.

Our measurements pinpointed some interesting aspects on the molecules discussed in this chapter. In particular we characterized the donor unit and we found it as a very good candidate to be employed in molecules designed to observe and study this kind of processes, in particular coupled with the well known acceptor chromophore adopted in this case and in the Ref.[56]. A step further will be to sensitize a new bi-chromophore composed by the same donor and acceptor couple but bounded to a different rigid linker. As mentioned above the employment of such a kind of rigid bridge is useful for the selectivity of the molecule's geometry during the EET process. In order to make this transfer faster and more efficient it would be smart to adopt a linker which block the two chromophores in a closer position in order to maximize the dipole-dipole coupling.

Chapter 8

Conclusions

The spectroscopic investigation of very fast intra- and inter-molecular processes, like energy and electron transfer, requires specific experimental methods, capable of preserving both frequency and time resolution at the highest possible level. This thesis work, carried on within the framework of a research project aimed to the understanding of the energy transfer mechanisms in poly-chromophoric molecular systems, has been in large part dedicated to designing, building and testing the complex spectroscopic apparatus to be used in four wave mixing experiments, with special attention to the two-dimensional photon echo. The requirement of having very short light pulses whose central frequency can be tuned in a broad visible spectral range, gave rise to the need of designing and building a Non-collinear Optical Parametric Amplifier (NOPA).

The first step was the design of the optical layout of the NOPA and of the photon echo spectrometer itself, done with the CAD software support. The help of this digital support, allowed me to design a compact and stable set-up, pre-determining, with millimeter accuracy, the disposition of each optical element, including some custom components that were realized in the LENS' Mechanical Workshop. This preparatory work made the realization of the entire set-up on the laboratory table easy.

Once the opto-mechanical set-up was completed, I focused on the acquisition of the signal. In particular, I interfaced a commercial monochromator with a home-made NMOS linear array detector realized and programmed by

the LENS' Electronic Workshop under the guidance of Prof. Marco Prevedelli who designed the logic circuits. The timing of the electronic components is synchronized with the laser trigger; the whole set-up is controlled by a PC via the USB port, thanks to a software that I wrote in Labview language.

I wrote also the computer codes for the data treatment and analysis. In particular, using MatLab language I wrote two codes for extracting the transient grating (TG) and 2D photon echo (2D PE) spectra from the experimental row data. The most relevant part of this work was dedicated to devising and testing proper methods to correct for the unavoidable phase mismatches affecting the acquired data. Following the approach proposed in recent literature, I had to include in the code that yields the photon echo spectra a number of adjustable parameters, to be optimized in order to obtain the correct two dimensional spectra.

Experiments of this kind, which make use of interferometric methods, are possible only if the phase distribution of the e.m. field is flat throughout the entire pulse spectrum. It was then necessary to characterize the pulses generated by the NOPA: I employed time resolved optical Kerr effect (OKE) to quantify the phase dispersion of the pulses at the exit of the parametric amplifier and at the sample location, thus being able of choosing the most efficient compression strategy. Different methods were considered and tested, both experimentally and in computer simulations; we finally found that multi-reflection on dispersion compensating mirror (Venteon® DCMs from Laser Quantum®) is the preferable solution, which allowed us to lower the pulse duration to approximately 10 fs.

The necessary tests of the experimental set-up and of the computer codes that yield the final 2D spectra were performed by replicating the measurements on test molecular dyes present in the literature. The experiments performed on Rhodamine 800 and on Cresyl Violet confirm the excellent stability of the system in non-stop experiments lasting many hours. The comparison of the extracted 2D spectra with those already published demonstrate that our computer codes guarantee a very accurate treatment of the data.

As a first application of the experimental apparatus to the study of interchromophoric energy transfer, we investigated the sub-picosecond ultrafast dynamics in a bi-chromophoric molecular dye, sensitised by Prof. Stefano

Cicchi. The molecule consists of two different BODIPY chromophores, one acting as donor and the other as acceptor, linked by a rigid moiety. Pump-probe Transient Absorption Spectroscopy (TAS) measurements performed on this molecule, revealed that a partial Electronic Energy Transfer (EET) takes place with 22 ps time constant. The observation that the earliest transient spectrum recorded at 1.3 ps shows the presence of the characteristic acceptor's bleaching band, could be interpreted as an indication that a much faster, sub-picosecond transfer process goes into action. The time evolution of the 2D PE spectra shows that a cross peak is present, but no delay time variation of its intensity was detected, thus leading us to ascribe the cross peak to direct excitation of the acceptor chromophore.

In conclusion, I can say that the experimental and computational apparatus that I set-up in my thesis work is already well operating, so that we can be confident about the reliability of the measured 2D spectra. Of course, some further steps can be foreseen to improve the system. The first desirable improvement concerns the acquisition system: replacing the present NMOS array detector with a commercial cooled CCD camera would allow us to lower the pulse energy and, at the same time, significantly increase the sensitivity and the signal-to-noise ratio. Another interesting possible improvement concerns the NOPA, and here two parallel ways could be taken. The first one involves a second amplification stage that would allow lowering the energy driven on the BBO crystals, without any loss in the output energy. This intervention would increase the stability of the parametric generation and, consequently, of the whole experiment. The second improvement could be adding a second NOPA, in order to make two colours experiments possible. With two pulsed light sources it would be possible tuning the wavelengths of the pump and probe pulses independently, thus broadening substantially the number of poly-chromophoric systems that can be studied.

Bibliography

[1] Maroncelli, M., Macinnis, J., and Fleming, G. R., Science **243** (1989) 1674.

[2] Jimenez, R., Fleming, G. R., Kumar, P. V., and Maroncelli, M., Nature **369** (1994) 471.

[3] Hamm, P., Lim, M., DeGrado, W. F., and Hochstrasser, R. M., Proceeding of the National Academy of Sciences **96** (1999) 2036.

[4] Fecko, C. J., Eaves, J. D., Loparo, J. J., Tokmakoff, A., and Geissler, P. L., Science **301** (2003) 1698.

[5] Mukamel, S., *Principles of Nonlinear Optical Spectroscopy*, Oxford Univ. Press, New York, 1995.

[6] Hamm, P. and Zanni, M. T., *Concepts and Methods of 2D Infrared Spectroscopy*, Cambridge Univ. Press, Oxford, 2011.

[7] Aue, W. P., Bartholdi, E., and Ernst, R. R., Journal of Chemical Physics **64** (1976) 2229.

[8] Ernst, R. R., Bodenhausen, G., and Wokaun, A., *Principles of Nuclear Magnetic Resonance in One and Two Dimensions*, Oxford Univ. Press, Oxford, 1987.

[9] Lepetit, L. and Joffre, M., Optics Letters **21** (1996) 564.

[10] Belabas, N. and Joffre, M., Optics Letters **27** (2002) 2043.

[11] Hybl, J. D., Albrecht, A. W., Gallager Faeder, S. M., and Jonas, D. M., Chemical Physics Letters **297** (1998) 307.

[12] Hybl, J. D., Albrecht Ferro, A., and Jonas, D. M., The Journal of Chemical Physics **115** (2001) 6606.

[13] Ashland, M. C., Zanni, M. T., and Hochstrasser, R. M., Proceeding of the National Academy of Sciences **97** (2000) 8219.

[14] Golonzka, O., Khalil, M., Demirdoven, N., and Tokmakoff, A., Physical Review Letter **86** (2001) 2154.

[15] Khalil, M., Demirdoven, N., and Tokmakoff, A., Journal of Chemical Physics **047401** (2003) 90.

[16] Mukamel, S., Annual Review of Physical Chemistry **51** (2000) 691.

[17] Scheurer, C. and Mukamel, S., Journal of Chemical Physics **115** (2001) 4989.

[18] Cho, M., Physical Chemistry Communication **5** 40.

[19] Cho, M., *Two-Dimensional Optical Spectroscopy*, CRC Press, Boca Raton, 2009.

[20] Ge, N. H., Zanni, M. T., and Hochstrasser, R. M., Journal of Physical Chemistry A **106** (2002) 962.

[21] Fang, C. et al., Chemical Physics Letters **382** (2003) 582.

[22] Gallager, S. M. et al., Journal of the Optical Society of America **15** (1998) 2338.

[23] Gallager Faeder, S. M. and Jonas, D. M., Journal of Physical Chemistry A **103** (1999) 10489.

[24] Hybl, J. D., Yu, A., Farrow, D. A., and Jonas, D. M., Journal of Physical Chemistry A **106** (2002) 7651.

[25] Collini, E. and Scholes, G. D., The journal of physical chemistry. A **113** (2009) 4223.

[26] Jonas, D. M., Annual Review of Physical Chemistry **54** (2003) 425.

[27] Cerullo, G., Nisoli, M., and De Silvestri, S., Applied Physics Letters **71** (1997) 3616.

[28] Cerullo, G. and De Silvestri, S., Review of Scientific Instruments **74** (2003) 1.

[29] Maznev, A. A., Nelson, K. A., and Rogers, T. A., Optics Letters **23** (1998) 1319.

[30] Goodno, G. D., Dadusc, G., and Miller, R. J. D., Journal of the Optical Society of America B **15** (1998) 1791.

[31] Goodno, G. D., Astinov, V., and Miller, R. J. D., Journal of Physical Chemistry B **103** (1999) 603.

[32] Khalil, M. Demirdven, N., Golonzka, O., Fecko, C. J., and Tokmakoff, A., Journal of Physical Chemistry A **104** (2000) 5711.

[33] Xu, Q. H., Ma, Y. Z., Stickpin, I. V., and R., F. G., Journal of Chemical Physics **116** (2002) 9333.

[34] Briner, T., Stickpin, I. V., and Fleming, G. R., Optics Letters **29** (2004) 884.

[35] Brixner, T. et al., Nature **434** (2005) 625.

[36] Prokhorenko, V. I., Halpin, A., and Miller, R. J. D., Optics express **17** (2009) 9764.

[37] Tian, P., Keuster, D., Suzaki, Y., and Warren, W. S., Science **300** (2003) 1553.

[38] Grumstrup, E. M., Shim, S., Montgomery, M. A., Damrauer, N. H., and Zanni, M. T., Optics Express **15** (2007) 16681.

[39] Brixner, T., Mancal, T., Stiopkin, I. V., and Fleming, G. R., The Journal of chemical physics **121** (2004) 4221.

[40] Harel, E., Fidler, A. F., and Engel, G. S., Proceedings of the National Academy of Sciences **107** (2010) 16444.

[41] Harel, E., Long, P. D., and Engel, G. S., Optics letters **36** (2011) 1665.

[42] Fidler, A. F., Harel, E., and Engel, G. S., Journal of Physical Chemistry Letters **1** (2010) 2876.

[43] Brixner, T., Stiopkin, I. V., and Fleming, G. R., Optics Letters **29** (2004) 884.

[44] Lepetit, L., Chériaux, G., and Joffre, M., Journal of the Optical Society of America B **12** (1995) 2467.

[45] Park, S., Kwak, K., and Fayer, M. D., Laser Physics Letters **4** (2007) 704.

[46] Anna, J. M., Song, Y., Dinshaw, R., and Scholes, G. D., Pure and Applied Chemistry **85** (2013) 1307.

[47] Diels, J. and Rudolf, W., *Ultrashort Laser Pulse Phenimena, II ed.*, Academic Press, Massachusetts, 2006.

[48] Oran Brigam, E., *The Fast Fourier Transform: An Introduction to Its Theory and Application*, Prentice Hall, New Jersey, 1973.

[49] Ramírez-Corral, C. Y., Rosete-Aguilar, M., and Garduño-Mejía, J., Journal of Modern Optics **56** (2009) 1659.

[50] Turner, D. B., Wilk, K. E., Curmi, P. M. G., and Scholes, G. D., The Journal of Physical Chemistry Letters **2** (2011) 1904.

[51] Pollard, W. T., Lee, S.-Y., and Mathies, R. a., The Journal of Chemical Physics **92** (1990) 4012.

[52] Collini, E. et al., Nature **463** (2010) 644.

[53] Butkus, V., Zigmantas, D., Valkunas, L., and Abramavicius, D., Chemical Physics Letters **545** (2012) 40.

[54] Deisenhofer, J. and Norris, J. R., *The Photosynthetic Reaction Center*, Academic Press, New York, 1993.

[55] Blankeship, R. E., *Molecular Mechanism of Photosynthesis*, Blackwell Sciences, Oxford, 2002.

[56] Donato, M. D. et al., The Journal of Physical Chemistry C **118** (2014) 23476.

[57] Sabatini, R. P. et al., Journal of Physical Chemistry Letters **2** (2011) 223.

[58] Bai, D. et al., Physical Chemistry Chemical Physics **15** (2013) 9854.

[59] El-Khouly, M. E., Fukuzumi, S., and F., D., ChemPhsChem **15** (2014) 30.

[60] Shi, W. J., El-Khouly, M. E., Ohkubo, K., Fukuzumi, S., and Ng, D. K., Chemistry a European Journal **19** (2013) 11332.

[61] D,ÄôSouza, F. et al., Journal of the American Chemical Society **126** (2004) 7898.

[62] Guo, S. et al., Chemical Science **5** (2014) 489.

[63] Loudet, A. and Burgess, K., Chemical Reviews **107** (2007) 4891.